ALMA MATER STUDIORUM · UNIVERSITY OF BOLOGNA

School of Science
Department of Physics and Astronomy
Master Degree in Physics

Neutrino interactions in the SAND LAr volume at the DUNE Near Detector site

Supervisor: Submitted by:

Dr. Gabriele Sirri   Alessandro Ruggeri

Co-supervisors:

Dr. Valerio Pia
Dr. Nicolò Tosi

Academic Year 2020/2021

Abstract

The neutrino mass ordering and the leptonic CP violation phase are key parameters of the three-neutrino flavour mixing still to be determined. Measuring these parameters is the main goal of DUNE, a next generation Long Baseline neutrino experiment under construction in the United States.

DUNE will feature a Near and a Far Detector site. An important component of the Near detector complex is the SAND apparatus, which will include GRAIN, a novel liquid Argon detector that aims at imaging neutrino interactions using scintillation light. For this purpose, an innovative optical readout system based on Coded Aperture Masks is under study.

This thesis work is aimed at a first quantitative assessment of a 3D neutrino event reconstruction algorithm for GRAIN. The processing procedure is optimized and the reconstruction performance is evaluated. Promising results are obtained.

Contents

Introduction

The experimental study of neutrino oscillations has made it possible to determine many of the parameters linked to neutrino masses by the complementary use of multiple experimental channels and sources. Some parameters are yet to be determined, most importantly the ordering of neutrino masses and the potential CP violating phase of the neutrino mixing matrix, the latter of which would have a profound impact on the whole lepton sector of particle physics. The search for the remaining unknowns in neutrino physics is the aim of the next generation of neutrino experiments. The Deep Underground Neutrino Experiment (DUNE) will be one of the flagship projects, leveraging innovative detector technologies and the most powerful neutrino beam available at the time of completion.

DUNE will feature two experimental sites, the Near and Far Detector complexes, the former being located at Fermilab, a few hundred meters from the neutrino beam source, and the latter being housed at SURF, 1300 km away. For the oscillation parameters to be determined through the data of the multi-kiloton Liquid Argon Time Projection Chambers (LArTPC) of the Far Detector (FD), the neutrino beam must be characterized before the onset of oscillations at the Near Detector (ND) complex: the three proposed near detectors will be able to provide complementary information on the neutrino beam and to refine the interaction models that will be necessary to analyse the FD data. The ND will also be capable of conducting searches for New Physics, providing high granularity ad resolution.

The SAND detector will be the only one in the ND complex to be fixed in an on-axis position, from which it will monitor the neutrino beam flux. For the inner volume of the SAND magnet and calorimeter, reused from the KLOE experiment, a system of trackers and a LAr active target is planned. The proposed LAr active target of the ND SAND detector, also known as GRAIN, aims at providing fast and granular vertex and track identification capabilities, which will be helpful for ν-LAr interaction modelling and to complement the tracking system. For GRAIN, an optical detection system is being considered, aiming to provide a complete spatial and timing reconstruction of the events with a timescale of a few nanoseconds. One of the two solutions that is being developed for the optical readout system is based on the Coded Aperture Mask technique, in which event reconstruction will be possible through the combination of images from

multiple Coded Aperture cameras with different viewpoints. This will be performed by a reconstruction algorithm based on a combinatorial approach: its output is a 3D neutrino event reconstruction in terms of the probability for each unit voxel of the GRAIN inner volume to be the source of a detected photon.

The aim of this thesis work is to perform the first quantitative assessment of the performance of this new reconstruction technique, identifying its characteristics and issues and determining the consistency of its results against the simulated Monte Carlo data. A strategy for extracting the basic event observables is additionally outlined. Specifically, the distributions of the reconstructed amplitudes will first be analysed, identifying their features and the origin of reconstruction artefacts. A preliminary evaluation of the consistency of the reconstructions to the true distributions will be performed by means of the Structural Similarity index. Estimators for the basic event features, vertex position, track length and total energy deposition are then developed and tested on the simulated data in order to determine their validity and the optimal procedure for their extraction.

The standard and metrics for the reconstruction quality obtained by this work will serve as a guide for the future development of the algorithm, enabling to test quantitatively the performance of new versions against the simulated data.

The dissertation is organized as follows:

- Chapter 1 will present an overview of the current status of neutrino physics, outlining the theoretical description of massive neutrinos and introducing the phenomenology of neutrino oscillations and the experimental results on the mixing parameters.

- Chapter 2 will describe the physics objectives, structure and detectors of the future DUNE experiment.

- Chapter 3 will outline the principles and features of Coded Aperture imaging and subsequently present the rationale and specifics of the GRAIN optical detection system and of the reconstruction algorithm.

- Chapter 4 will present the preliminary analysis of the reconstructed amplitude distributions, with the determination of their features and the comparison to the Monte Carlo data through an image-similarity metric.

- Chapter 5 will describe the analyses performed to determine the quality of the reconstruction estimates of basic features of the events, and to find an optimal processing procedure.

Chapter 1

Neutrino Physics

1.1 The physics of neutrinos

Ever since their proposal by Pauli in 1930, neutrinos have been at the forefront of particle physics, as the study of their interactions has been crucial for the description of phenomena ranging from β-decays and the quark structure of nucleons to stellar thermonuclear reactions and the gravitational collapse in supernovas.

Neutrinos are, at present, the only known fundamental fermions with zero electric charge and, as such, they only interact through weak charged and neutral current processes, with cross sections at all available energies that are much smaller than the electromagnetic cross sections of both quarks and other leptons. Detecting such rare neutrino processes required the development of special experimental techniques, which have since provided unique handles on many aspects of fundamental physics.

Neutrinos were, in the initial formulation of the Standard Model, thought to be massless, but the observations of Neutrino Flavour Oscillations by experiments operating in many different regimes have since proven that the mass of these particles is indeed non-zero. While the measurement of the absolute values of neutrino masses is still an open problem, the available upper limits are so much smaller than the masses of the other fundamental fermions that their *natural* production mechanism is thought to be of a non-Standard Model origin.

Neutrinos can thus be an handle with which to probe beyond the Standard Model physics: flavour oscillations represent the first hint for such a theory, and the searches for neutrinoless double β-decay might provide additional evidence by proving the Majorana nature of neutrinos and the non Standard Model origin of their masses.

This section aims at providing a brief theoretical overview of the main aspects of neutrino physics, discussing the relevant observables and introducing the questions that still remain open for next generation experiments to investigate.

1.1.1 Neutrino flavour and mass

Three types, or *flavours states*, of neutrinos and antineutrinos are currently known; they are distinguished into electron-type, muon-type and tau-type (ν_e, ν_μ and ν_τ respectively) by the charged lepton that they couple to in weak charged current (CC) interactions. The number of left handed, and thus interacting, flavour neutrinos is constrained by the cancellation of the quantum anomalies of the Standard Model to be the same as that of charged leptons and indeed results from LEP have ruled out extra neutrino flavours with masses below $M_W/2$ [1, 2].

Flavour neutrino states take part in weak CC and neutral current (NC) processes described, to an impressive accuracy, by the Standard Model weak interaction lagrangian terms [1, 2]:

$$\mathcal{L}_I^{CC} = -\frac{g}{2\sqrt{2}} j_\alpha^{CC} W^\alpha + h.c., \qquad j_\alpha^{CC} = 2 \sum_{\ell=e,\mu,\tau} \bar{\nu}_{\ell L} \gamma_\alpha \ell_L$$

$$\tag{1.1.1}$$

$$\mathcal{L}_l^{NC} = -\frac{g}{2\cos\theta_W} j_\alpha^{NC} Z^\alpha, \qquad j_\alpha^{NC} = \sum_{\ell=e,\mu,\tau} \bar{\nu}_{\ell L} \gamma_\alpha \nu_{\ell L}.$$

The discovery of neutrino oscillations, which by now has been followed up by detailed studies over a wide region of the parameter space [3], has additionally established one of the core aspects of neutrino physics: that neutrinos have a non-zero mass. Indeed flavour mixing and thus oscillations require neutrino mass terms that feature the flavour fields or a combination of them.

The simplest extension to the Standard Model that can accommodate neutrino mixing is the introduction of the right-handed (RH) components of the flavour neutrino fields, $\nu_{\alpha R}$. In this so-called *minimally extended Standard Model* the asymmetry between the lepton and quark sector due to the absence of RH neutrino fields is eliminated, and Dirac mass terms for neutrinos are generated through the Brout-Englert-Higgs mechanism as with the other fundamental fermions. In particular, the SM Higgs-lepton Yukawa lagrangian is extended with a term containing the conjugate Higgs doublet $\tilde{\Phi}$:

$$\mathcal{L}_{H,L} = -\sum_{\alpha,\beta=e,\mu,\tau} Y_{\alpha\beta}'^{\ell} \overline{L}_{\alpha L} \Phi \ell'_{\beta R} - \sum_{\alpha,\beta=e,\mu,\tau} Y_{\alpha\beta}'^{\nu} \overline{L}_{\alpha L} \tilde{\Phi} \nu'_{\beta R} + h.c., \tag{1.1.2}$$

where $L_{\alpha L}$ are the left-handed lepton isospin doublets and

$$\tilde{\Phi} \equiv i\sigma_2 \Phi^* = \frac{1}{\sqrt{2}} \begin{pmatrix} v+h \\ 0 \end{pmatrix}. \tag{1.1.3}$$

The complete Higgs-lepton lagrangian can then be written as:

$$\mathcal{L}_{H,L} = -\left(\frac{v+h}{\sqrt{2}}\right) \left[\overline{\boldsymbol{\ell}}'_L Y'^{\ell} \boldsymbol{\ell}'_R + \overline{\boldsymbol{\nu}}'_L Y'^{\nu} \boldsymbol{\nu}'_R \right] + h.c. \tag{1.1.4}$$

with $\boldsymbol{\ell}'_{L,R}$ and $\boldsymbol{\nu}'_{L,R}$ being the chiral lepton arrays:

$$\boldsymbol{\ell}'_i \equiv \begin{pmatrix} e'_i \\ \mu'_i \\ \tau'_i \end{pmatrix}, \quad \boldsymbol{\nu}'_i \equiv \begin{pmatrix} \nu'_{ei} \\ \nu'_{\mu i} \\ \nu'_{\tau i} \end{pmatrix}, \quad i = L, R. \tag{1.1.5}$$

The matrices of Yukawa couplings Y'^ℓ and Y'^ν can then be diagonalized in a similar way:

$$V_L^{\ell\dagger} Y'^\ell V_R^\ell = Y^\ell, \qquad \text{with} \quad Y_{\alpha\beta}^\ell = y_\alpha^\ell \delta_{\alpha\beta} \qquad (\alpha, \beta = e, \mu, \tau)$$

and

$$\tag{1.1.6}$$

$$V_L^{\nu\dagger} Y'^\nu V_R^\nu = Y^\nu, \qquad \text{with} \quad Y_{k\ell}^\nu = y_k^\nu \delta_{k\ell} \qquad (k, j = 1, 2, 3)$$

with real and positive y_α^ℓ and y_k^ν and $V_L^\ell, V_R^\ell, V_L^\nu, V_R^\nu$ being appropriate 3×3 unitary matrices. In order to be definite mass states, the lepton fields must have a diagonalized Yukawa lagrangian, thus the *massive lepton fields* can be defined as:

$$\boldsymbol{\ell}_L = V_L^{\ell\dagger} \boldsymbol{\ell}'_L \equiv \begin{pmatrix} e_L \\ \mu_L \\ \tau_L \end{pmatrix}, \qquad \boldsymbol{\ell}_R = V_R^{\ell\dagger} \boldsymbol{\ell}'_R \equiv \begin{pmatrix} e_R \\ \mu_R \\ \tau_R \end{pmatrix}$$

$$\tag{1.1.7}$$

$$\boldsymbol{n}_L = V_L^{\nu\dagger} \boldsymbol{\nu}'_L \equiv \begin{pmatrix} \nu_{1L} \\ \nu_{2L} \\ \nu_{3L} \end{pmatrix}, \qquad \boldsymbol{n}_R = V_R^{\nu\dagger} \boldsymbol{\nu}'_R \equiv \begin{pmatrix} \nu_{1R} \\ \nu_{1R} \\ \nu_{3R} \end{pmatrix}$$

leading to the diagonalized Higgs-lepton Yukawa Lagrangian:

$$\begin{aligned} \mathcal{L}_{H,L} &= -\left(\frac{v+h}{\sqrt{2}}\right) \left[\overline{\boldsymbol{\ell}}_L Y^\ell \boldsymbol{\ell}_R + \overline{\boldsymbol{n}}_L Y^\nu \boldsymbol{n}_R\right] + h.c. \\ &= -\left(\frac{v+h}{\sqrt{2}}\right) \left[\sum_{\alpha=e,\mu,\tau} y_\alpha^\ell \overline{\ell}_{\alpha L} l_{\alpha R} + \sum_{k=1}^3 y_k^\nu \overline{\nu}_{kL} \nu_{kR}\right] + h.c. \end{aligned} \tag{1.1.8}$$

which contains the Dirac mass terms m_α and m_k respectively for the charged lepton fields $\ell_\alpha = \ell_{\alpha L} + \ell_{\alpha R}$ and for the neutrino fields $\nu_k = \nu_{kL} + \nu_{kR}$:

$$m_\alpha = \frac{y_\alpha^\ell v}{\sqrt{2}} \quad (\alpha = e, \mu, \tau) \quad \text{and} \quad m_k = \frac{y_k^\nu v}{\sqrt{2}} \quad (k = 1, 2, 3). \tag{1.1.9}$$

The Standard Model leptonic weak charged current lagrangian is written in terms of the chiral lepton arrays $\boldsymbol{\ell}'$ and $\boldsymbol{\nu}'$ as:

$$\mathcal{L}_\ell^{CC} = -\frac{g}{2\sqrt{2}} j_\alpha^{CC} W^\alpha + h.c., \qquad j_\alpha^{CC} \equiv 2\overline{\boldsymbol{\nu}}'_L \gamma_\alpha \boldsymbol{\ell}'_L \tag{1.1.10}$$

and using eqn. (1.1.7), the lepton current j_α^{CC} becomes:

$$j_\alpha^{CC} = 2\overline{\boldsymbol{\nu}}'_L \gamma_\alpha \boldsymbol{\ell}'_L = 2\overline{\boldsymbol{n}}_L V_L^{\nu\dagger} \gamma_\alpha V_L^\ell \boldsymbol{\ell}_L = 2\overline{\boldsymbol{n}}_L \gamma_\alpha V_L^{\nu\dagger} V_L^\ell \boldsymbol{\ell}_L. \tag{1.1.11}$$

The charged lepton current thus depends on the product

$$U \equiv V_L^{\nu\dagger} V_L^\ell \tag{1.1.12}$$

which, analogously to the CKM matrix for quarks, describes the mixing in the lepton sector. Specifically, the leptonic weak charged current is written, in terms of U, as

$$j_\alpha^{CC} = 2\overline{\boldsymbol{n}_L} \gamma_\alpha U^\dagger \boldsymbol{\ell}_L. \tag{1.1.13}$$

As charged lepton *flavour states* coincide with the massive fields $\boldsymbol{\ell}$, it is customary to define the left-handed *flavour neutrino* fields as:

$$\boldsymbol{\nu}_L \equiv U\boldsymbol{n}_L = V_L^{l\dagger} \boldsymbol{\nu}'_L, \quad \text{with} \quad \boldsymbol{\nu}_L \equiv \begin{pmatrix} \nu_{eL} \\ \nu_{\mu L} \\ \nu_{\tau L} \end{pmatrix} \tag{1.1.14}$$

allowing to write the leptonic weak charged current as in eqn. (1.1.1):

$$j_\alpha^{CC} = 2\overline{\boldsymbol{\nu}}_L \gamma_\alpha \boldsymbol{\ell}_L = 2 \sum_{\ell=e,\mu,\tau} \overline{\nu}_{\ell L} \gamma_\alpha \ell_L. \tag{1.1.15}$$

The introduction of left-handed *flavour neutrino* fields allows to define the flavour lepton numbers as in the Standard Model: the weak charged current in eqn. (1.1.15) is invariant under the global $U(1)$ transformations

$$\ell_{\alpha L} \to e^{i\varphi_\alpha} \ell_{\alpha L}, \quad \nu_{\alpha L} \to e^{i\varphi_\alpha} \nu_{\alpha L} \quad (\alpha = e, \mu, \tau) \tag{1.1.16}$$

with each flavour having different phases. The charged lepton Yukawa lagrangian terms are invariant if the right-handed chiral fields transform with the same phases:

$$\ell_{\alpha R} \to e^{i\varphi_\alpha} \ell_{\alpha R} \quad (\alpha = e, \mu, \tau). \tag{1.1.17}$$

For neutrinos, conversely, it is not possible to find any transformation of the right-handed flavour fields $\nu_{\alpha R}$ that leaves simultaneously invariant the corresponding Yukawa terms and the kinetic part of the neutrino lagrangian. Thus flavour lepton numbers are not conserved in the neutrino sector: the next section shall describe the mixing of neutrino flavours in weak interactions and derive how it leads to neutrino oscillations [1].

1.1.2 Neutrino mixing and oscillations

The central object in the study of neutrino oscillations is the matrix U, defined in eqn. (1.1.12): named Pontecorvo-Maki-Nakagawa-Sakata (PMNS) matrix, its parameters are determinant to the phenomenology of neutrino oscillations and to the issues of CP invariance in the lepton sector and the Majorana nature of neutrinos. Measuring the PMNS matrix element has thus been one of the main objectives of oscillation experiments.

From its definition, in eqn. (1.1.12), it follows that the PMNS is a unitary 3×3 matrix and as such is characterized by $3^2 = 9$ real parameters, which can be represented by $n_{angles} = 3(3-1)/2 = 3$ mixing angles and $n_{phases} = 3(3+1)/2 = 6$ phases. Not all six of the phases are physical though, as the mixing matrix enters into the weak charged currents in eqn. (1.1.1) together with the Dirac fields of the charged leptons and the Dirac or Majorana fields of neutrinos. In the case of neutrinos being Dirac fields, the current terms are invariant under the global phase transformations

$$\ell_\alpha \to \ell_\alpha e^{i\varphi_\alpha}, \quad \nu_k \to \nu_k e^{i\varphi_k} \quad \text{and} \quad U_{\alpha k} \to U_{\alpha k} e^{i(\varphi_\alpha - \varphi_k)} \tag{1.1.18}$$

thus, as an overall phase $Ue^{i\varphi}$ in the PMNS matrix has no physical consequence, five of the six phases can be absorbed into the definition of the lepton fields, leaving a single physical one. The case of Majorana neutrino fields, whose mass lagrangian term is not invariant under the lepton number global $U(1)$ transformation, will be discussed more in detail in § 1.1.4, while in the following discussion of mixing and oscillations, Dirac neutrinos will be assumed.

In the field of neutrino oscillations, the PMNS matrix is conventionally written as:

$$U \equiv \begin{pmatrix} U_{e1} & U_{e2} & U_{e3} \\ U_{\mu 1} & U_{\mu 2} & U_{\mu 3} \\ U_{\tau 1} & U_{\tau 2} & U_{\tau 3} \end{pmatrix} \equiv \begin{pmatrix} 1 & 0 & 0 \\ 0 & c_{23} & s_{23} \\ 0 & -s_{23} & c_{23} \end{pmatrix} \begin{pmatrix} c_{13} & 0 & s_{13}e^{-i\delta} \\ 0 & 1 & 0 \\ -s_{13}e^{i\delta} & 0 & c_{23} \end{pmatrix} \begin{pmatrix} c_{12} & s_{12} & 0 \\ -s_{12} & c_{12} & 0 \\ 0 & 0 & 1 \end{pmatrix}$$
$$\tag{1.1.19}$$

where $c_{ij} \equiv \cos\theta_{ij}$ and $s_{ij} \equiv \sin\theta_{ij}$. This notation has proved particularly convenient because, as will be discussed in the following, θ_{13} has been measured to be relatively small, so that the central matrix is approximately diagonal [4]. Performing the matrix multiplication one gets the individual PMNS elements:

$$\begin{pmatrix} U_{e1} & U_{e2} & U_{e3} \\ U_{\mu 1} & U_{\mu 2} & U_{\mu 3} \\ U_{\tau 1} & U_{\tau 2} & U_{\tau 3} \end{pmatrix} = \begin{pmatrix} c_{12}c_{13} & s_{12}c_{13} & s_{13}e^{-i\delta} \\ -s_{12}c_{13} - c_{12}s_{23}s_{13}e^{i\delta} & c_{12}c_{23} - s_{12}s_{23}s_{13}e^{i\delta} & s_{23}c_{13} \\ s_{12}s_{23} - c_{12}c_{23}s_{13}e^{i\delta} & -c_{12}s_{23} - s_{12}c_{23}s_{13}e^{i\delta} & c_{23}c_{13} \end{pmatrix}.$$
$$\tag{1.1.20}$$

In the standard formulation of neutrino oscillations, neutrinos with flavour α and momentum $\vec{p}$ are created in a weak charged-current (CC) process from a charged lepton ℓ_α^- or together with a charged antilepton ℓ_α^+. If the energies and momenta of the particles

involved in the process are not measured with the accuracy needed to distinguish the neutrino mass states, as is the case for all experiments so far, the flavour state can be expressed as a coherent superposition of the mass eigenstates,

$$|\nu_\alpha\rangle = \sum_{k=1}^{3} U^*_{\alpha k} |\nu_k\rangle \quad (\alpha = e, \mu, \tau) \tag{1.1.21}$$

as follows from eqn. (1.1.14). The massive neutrinos $|\nu_k\rangle$ are eigenstates of the Hamiltonian with energy eigenvalues E_k

$$\mathcal{H} |\nu_k\rangle = E_k |\nu_k\rangle, \quad E_k = \sqrt{\vec{p}^2 + m_k^2} \tag{1.1.22}$$

thus, by the Schrödinger equation they evolve in time as plane waves:

$$|\nu_k(t)\rangle = e^{-iE_k t} |\nu_k\rangle. \tag{1.1.23}$$

The time evolution of a flavour state $|\nu_\alpha(t)\rangle$ describing a neutrino created with a definite flavour α at time $t = 0$ will thus be given by:

$$|\nu_\alpha(t)\rangle = \sum_{k=1}^{3} U^*_{\alpha k} e^{-iE_k t} |\nu_k\rangle \tag{1.1.24}$$

so that $|\nu_\alpha(t = 0)\rangle = |\nu_\alpha\rangle$. The unitarity relation $U^\dagger U = \mathbb{1}$ allows to express the massive states in terms of flavour states:

$$|\nu_k\rangle = \sum_{\alpha} U_{\alpha k} |\nu_\alpha\rangle \tag{1.1.25}$$

substituting this into eqn. (1.1.24) one obtains the time evolution of the $|\nu_\alpha(t)\rangle$ in terms of the flavour eigenstates:

$$|\nu_\alpha(t)\rangle = \sum_{\beta = e, \mu, \tau} \left(\sum_k U^*_{\alpha k} e^{-iE_k t} U_{\beta k} \right) |\nu_\beta\rangle. \tag{1.1.26}$$

Thus, a pure flavour state $|\nu_\alpha\rangle$ at $t = 0$ becomes a superposition of different flavour states at $t > 0$, with the amplitude of a transition $\nu_\alpha \to \nu_\beta$ at time t being

$$A_{\nu_\alpha \to \nu_\beta}(t) \equiv \langle \nu_\beta | \nu_\alpha(t) \rangle = \sum_k U^*_{\alpha k} U_{\beta k} e^{-iE_k t}. \tag{1.1.27}$$

The transition probability is then given by:

$$P_{\nu_\alpha \to \nu_\beta}(t) = |A_{\nu_\alpha \to \nu_\beta}|^2 = \sum_{k,j} U^*_{\alpha k} U_{\beta k} U_{\alpha j} U^*_{\beta j} e^{-i(E_k - E_j)t}. \tag{1.1.28}$$

For ultrarelativistic neutrinos, the energy momentum relation in eqn. (1.1.22) can be approximated by:

$$E_k \simeq E + \frac{m_k^2}{2E}, \quad E = |\vec{p}| \tag{1.1.29}$$

so that

$$E_k - E_j \simeq \frac{\Delta m_{kl}^2}{2E} \tag{1.1.30}$$

where Δm_{kl}^2 is the squared-mass difference

$$\Delta m_{kl}^2 \equiv m_k^2 - m_j^2. \tag{1.1.31}$$

The transition probability $P_{\nu_\alpha \to \nu_\beta}(t)$ is therefore approximated by:

$$P_{\nu_\alpha \to \nu_\beta}(t) = \sum_{k,j} U_{\alpha k}^* U_{\beta k} U_{\alpha j} U_{\beta j}^* \exp\left(-i\frac{\Delta m_{kj}^2 t}{2E}\right). \tag{1.1.32}$$

In order to move from the mixing of neutrino flavours to the phenomenon of oscillations as observed by experiments, one must finally consider that the propagation time t is not measured: what is known is instead the distance L between the source and the detector. As neutrinos are ultrarelativistic, it is possible to approximate $L = t$, leading to:

$$P_{\nu_\alpha \to \nu_\beta}(L, E) = \sum_{k,j} U_{\alpha k}^* U_{\beta k} U_{\alpha j} U_{\beta j}^* \exp\left(-i\frac{\Delta m_{kj}^2 L}{2E}\right). \tag{1.1.33}$$

From this expression it follows that the phases of neutrino oscillations

$$\Phi_{kj} = -\frac{\Delta m_{kj}^2 L}{2E} \tag{1.1.34}$$

are determined by the source-detector distance L and the neutrino energy E, which are quantities dependent on the experiment, as well as on the squared-mass differences Δm_{kj}^2, which are instead physical constants to be determined. The amplitudes of the oscillations, on the other hand, only depend on the PMNS matrix elements, which are constants of nature [1].

The main results of neutrino oscillation experiments are therefore the determination of the squared-mass differences and the elements of the PMNS matrix: although the observation of neutrino oscillations implies massive neutrinos, it can't provide information on the absolute values of neutrino masses, except that either m_k^2 or m_j^2 must be larger than $|\Delta m_{kj}^2|$.

In Section 1.2 the strategies followed by experiments to determine the set of parameters of neutrino physics and the current results will be discussed in more detail.

1.1.3 CP violation

The discovery of CP violation in the systems of neutral K and B mesons has been one of the key results in the study of electroweak interactions: the amount that has been observed is compatible with that generated by the physical phase of the CKM mixing matrix [4].

The case of three-flavour Dirac neutrino mixing is equivalent to that of quarks, for CP violation to occur the following conditions must be satisfied:

- No two charged leptons or neutrinos must be degenerate in mass.

- No mixing angle must be equal to 0 or $\pi/2$.

- The PMNS matrix must be complex, i.e. the physical phase δ must be different from 0 or π. In the following the physical phase for Dirac-neutrino mixing will be referred to as δ_{CP}

These 14 conditions can be summarized by the following:

$$-2J(m_{\nu_2}^2 - m_{\nu_1}^2)(m_{\nu_3}^2 - m_{\nu_1}^2)(m_{\nu_3} - m_{\nu_2}^2)\cdot$$
$$\cdot (m_\mu^2 - m_e^2)(m_\tau^2 - m_e^2)(m_\tau^2 - m_\mu^2) \neq 0, \tag{1.1.35}$$

where the Jarlskog Invariant $J \equiv \mathrm{Im}\left[U_{e2}U_{e3}^*U_{\mu 2}^*U_{\mu 3}\right]$ quantifies in a rephasing-invariant way the CP violation in the lepton sector.

A CP transformation interchanges neutrinos with antineutrinos and reverses their helicities:

$$\nu_\alpha \xleftrightarrow{\text{CP}} \bar{\nu}_\alpha, \tag{1.1.36}$$

thus the oscillation channel $\nu_\alpha \to \nu_\beta$ is transformed into $\bar{\nu}_\alpha \to \bar{\nu}_\beta$ and experiments can be performed to measure the CP asymmetry

$$A_{\alpha\beta}^{CP} = P_{\nu_\alpha \to \nu_\beta} - P_{\bar{\nu}_\alpha \to \bar{\nu}_\beta} \tag{1.1.37}$$

and, as the conservation of the CPT implies that $A_{\alpha\beta}^{CP} = -A_{\beta\alpha}^{CP}$, it follows that the CP asymmetry can be only measured in transitions between different flavours.

The experimental channels that are being exploited to measure δ_{CP} will be detailed in Section 1.2.

1.1.4 Majorana neutrinos

While Dirac neutrinos have been assumed so far for ease of discussion, the possibility of them being Majorana particles has not yet been ruled out by experiments: indeed, it is key to the See-saw Mechanisms, the most promising *natural* explanations for the of light neutrino masses.

For Majorana neutrinos, the chiral components ν_L and ν_R of the field are not independent, and are instead related by the *Majorana condition*:

$$\nu_R = \nu_L^C \equiv \mathcal{C}\bar{\nu}_L^T, \tag{1.1.38}$$

where $C \equiv i\gamma^2\gamma^0$ is the charge conjugation operator. Substituting the previous definition in the decomposition of the neutrino field allows to rewrite the Majorana condition as

$$\nu = \nu_L + \nu_L^C = \nu^C. \tag{1.1.39}$$

Majorana particles are thus equal to their antiparticles, so that only neutral fermions like neutrinos can be described by a Majorana field.

As only the left-handed neutrino field interacts, the Dirac and Majorana descriptions are phenomenologically different for massive neutrinos: for massless particles, indeed, the same Weyl equations would hold for the chiral components in both cases. It follows then that the Dirac or Majorana nature of neutrinos can be distinguished only by measuring effects due to the neutrino mass.

The Majorana mass lagrangian for a single neutrino type can be generated using only the left-handed chiral field ν_L as its charge conjugate ν_L^C can be substituted in place of ν_R thanks to the Majorana condition. The Majorana mass term is thus given by:

$$\mathcal{L}_{mass}^M = -\frac{1}{2}m\bar{\nu}_L^C\nu_L + h.c., \tag{1.1.40}$$

with the full Majorana Lagrangian consisting of the kinetic terms for ν_L and ν_L^C in addition to the mass term.

The introduction of three generations of massive Majorana neutrinos requires the Majorana mass term to be diagonalized as with Dirac neutrinos, expressing the left-handed flavour fields $\boldsymbol{\nu}_L'$ as linear combinations of massive neutrino fields $\boldsymbol{\nu}_L$:

$$\boldsymbol{\nu}_L' = V_L^\nu\boldsymbol{\nu}_L \quad \text{with} \quad \boldsymbol{n}_L = \begin{pmatrix} \nu_{1L} \\ \nu_{2L} \\ \nu_{3L} \end{pmatrix} \tag{1.1.41}$$

so that the three-generation Majorana mass lagrangian can be written as:

$$\mathcal{L}_{mass}^M = -\frac{1}{2}\bar{\boldsymbol{n}}_L^C M \boldsymbol{n}_L + h.c. = \frac{1}{2}\sum_{k=1}^{3} m_k \bar{\nu}_{kL}^C \nu_{kL} + h.c. \tag{1.1.42}$$

with M being the diagonalized mass matrix. It can be seen now that this mass term is not invariant under the global $U(1)$ gauge transformations

$$\nu_{kL} \to e^{i\varphi}\nu_{kL} \quad (k = 1, 2, 3), \tag{1.1.43}$$

13

with the same phase φ for all massive neutrinos: this implies a violation of the total lepton number conservation, leading to beyond the Standard Model phenomena, such as the neutrinoless double-β decay, that represents the best handle to probe the potential Majorana nature of neutrinos.

The above discussion can be trivially extended to global $U(1)$ gauge transformations $\nu_{kL} \to e^{i\varphi_k}\nu_{kL}$, so that, recalling Section 1.1.2, the left-handed massive neutrinos cannot be rephased to eliminate two of the PMNS phases, leaving three physical CP violating phases. The mixing matrix of Majorana neutrinos can therefore be written as a product of a Dirac unitary mixing matrix U^D, similar to the usual PMNS, and a diagonal unitary matrix D^M featuring the two extra phases:

$$U = U^D D^M. \tag{1.1.44}$$

While for U^D the same parametrization and properties of the previously discussed PMNS hold, the D^M matrix can be written as

$$D^M \equiv \operatorname{diag}\left(e^{i\lambda_1}, e^{i\lambda_2}, e^{i\lambda_3}\right), \quad \text{with} \quad \lambda_1 = 0. \tag{1.1.45}$$

Through the previous two relations, the oscillation formula, in eqn. (1.1.2) can be extended to the case of Majorana neutrinos; in particular the products $U_{\alpha k}^* U_{\beta k}$ will reduce to

$$U_{\alpha k}^* U_{\beta k} = U_{\alpha k}^{D*} D_{\alpha k}^{M*} U_{\beta k}^D D_{\beta k}^M = U_{\alpha k}^{D*} U_{\beta k}^D \tag{1.1.46}$$

as, recalling eqn. (1.1.45), $D_{\alpha k} = \delta_{\alpha k} e^{i\lambda_k}$. Thus Majorana phases do not enter into the transition probabilities of neutrino oscillations, which are the same as with Dirac neutrinos, so that lepton number violating processes like the aforementioned neutrinoless double-β decay are the only handles to explore the Majorana nature of neutrinos [1, 2].

The determination of the Dirac or Majorana nature of neutrinos, together with the quantification of the amount of CP violation in the lepton sector through the measurement of δ_{CP}, is essential for our understanding of the process of *leptogenesis* and *baryogenesis* [5].

1.2 Neutrino physics experiments

The aim of this section is to outline the experimental channels and techniques that can be used to probe the core aspects of the neutrino sector, presenting the current results and the future prospects of this field.

1.2.1 Neutrino oscillation experiments

Neutrino oscillation experiments aim at retrieving, through the relations derived in Section 1.1.2, the PMNS parameters and the squared-mass differences. The measure of

fluxes of flavour neutrinos at the production and detection points allows to determine the probability of oscillation into a different neutrino flavour than the initial one. Two broad categories of experiments are considered:

- **Appearance experiments**, which measure transitions between different neutrino flavours, according to eqn. (1.1.2). As the final flavour can be either absent or present as contamination in the initial beam, the background for its measurement can be very small. Thus appearance experiments can be sensitive to rather small values of the mixing angle.

- **Disappearance experiments**, which measure the survival probability of a neutrino flavour

$$P_{\nu_\alpha \to \nu_\alpha}(L, E) = 1 - 4 \sum_{k>j} |U_{\alpha k}|^2 |U_{\alpha j}|^2 \sin^2 \left(\frac{\Delta m_{kj}^2 L}{2E} \right), \qquad (1.2.1)$$

by comparing its initial and final interaction rates. As the interaction rates have statistical fluctuations, apart from oscillations, small disappearances are difficult to reveal, so that disappearance experiments are not suited for measuring small mixing angles.

1.2.1.1 Two-neutrino mixing

For the description of neutrino oscillation data, the **two-neutrino mixing** approximation has proved particularly useful: this consists in neglecting the coupling of the flavour neutrinos to the third massive eigenstate that exists in nature. Such an assumption has two practical advantages:

- it leads to much simpler oscillation formulae that depend on fewer parameters than in the actual case of three-neutrino mixing,

- many experimental channels are not sensitive to the influence of three-neutrino mixing, so that data can be analysed with the effective two-neutrino mixing model.

In two-neutrino mixing, the two flavour neutrinos ν_α and ν_β can be pure flavour neutrinos $(\alpha, \beta = e, \mu, \tau)$ or linear combinations of such pure flavours; for instance, in ν_e-disappearance experiments, $\nu_\alpha = \nu_e$ and $\nu_\beta = c_\mu \nu_\mu + c_\tau \nu_\tau$, as only the fluxes of ν_e are measured. The flavour states are linear superposition of two massive neutrinos ν_1 and ν_2 according to the effective mixing matrix

$$U = \begin{pmatrix} \cos\theta & \sin\theta \\ -\sin\theta & \cos\theta \end{pmatrix}, \qquad (1.2.2)$$

where $0 \leq \theta \leq \pi/2$. Furthermore, in two-neutrino mixing there is only the squared-mass difference

$$\Delta m^2 \equiv \Delta m_{21}^2 = m_2^2 - m_1^2, \tag{1.2.3}$$

where ν_1 can be taken as the lightest eigenstate, so that Δm^2 is positive. Starting from eqn. (1.2.2), the probability of the oscillations $\nu_\alpha \to \nu_\beta$, $\alpha \neq \beta$ can be derived straightforwardly:

$$P_{\nu_\alpha \to \nu_\beta}(L, E) = \frac{1}{2} \sin^2 2\theta \left[1 - \cos\left(\frac{\Delta m^2 L}{2E} \right) \right] \quad (\alpha \neq \beta), \tag{1.2.4}$$

and from this the survival probability $P_{\nu_\alpha \to \nu_\alpha}(L, E)$ follows trivially:

$$P_{\nu_\alpha \to \nu_\alpha}(L, E) = 1 - P_{\nu_\alpha \to \nu_\beta}(L, E) = 1 - \sin^2 2\theta \sin^2\left(\frac{\Delta m^2 L}{4E} \right). \tag{1.2.5}$$

1.2.1.2 Averaged transition probability

It is not possible, in oscillation experiments, to measure the transition probabilities for precise values of the propagation distance L (or *baseline*) and of the neutrino energy E:, as both the source and detection processes are subject to spatial and energy uncertainties. Any actual measurement, therefore, must be averaged over the appropriate distributions of L and E. In the case of two-neutrino mixing, this average probability is given by:

$$\left\langle P_{\nu_\alpha \to \nu_\beta}(L, E) \right\rangle = \frac{1}{2} \sin^2 2\theta \left[1 - \left\langle \cos\left(\frac{\Delta m^2 L}{2E} \right) \right\rangle \right]$$

with
$$\tag{1.2.6}$$

$$\left\langle \cos\left(\frac{\Delta m^2 L}{2E} \right) \right\rangle = \int \cos\left(\frac{\Delta m^2}{2E} \right) \phi\left(\frac{L}{E} \right) \mathrm{d}\frac{L}{E}.$$

Under the assumption of a Gaussian distribution of the experimental L/E ratio with average $\langle L/E \rangle$ and standard deviation $\sigma_{L/E}$, the averaged oscillation probability follows the behaviour in Fig. 1.1 : for

$$\frac{\Delta m^2 L}{2E} \gg 1, \tag{1.2.7}$$

the transition probability averages out to

$$\left\langle P_{\nu_\alpha \to \nu_\beta} \right\rangle = \frac{1}{2} \sin^2 2\theta \quad (\alpha \neq \beta), \tag{1.2.8}$$

so that the experiment can only yield information on $\sin^2 2\theta$.
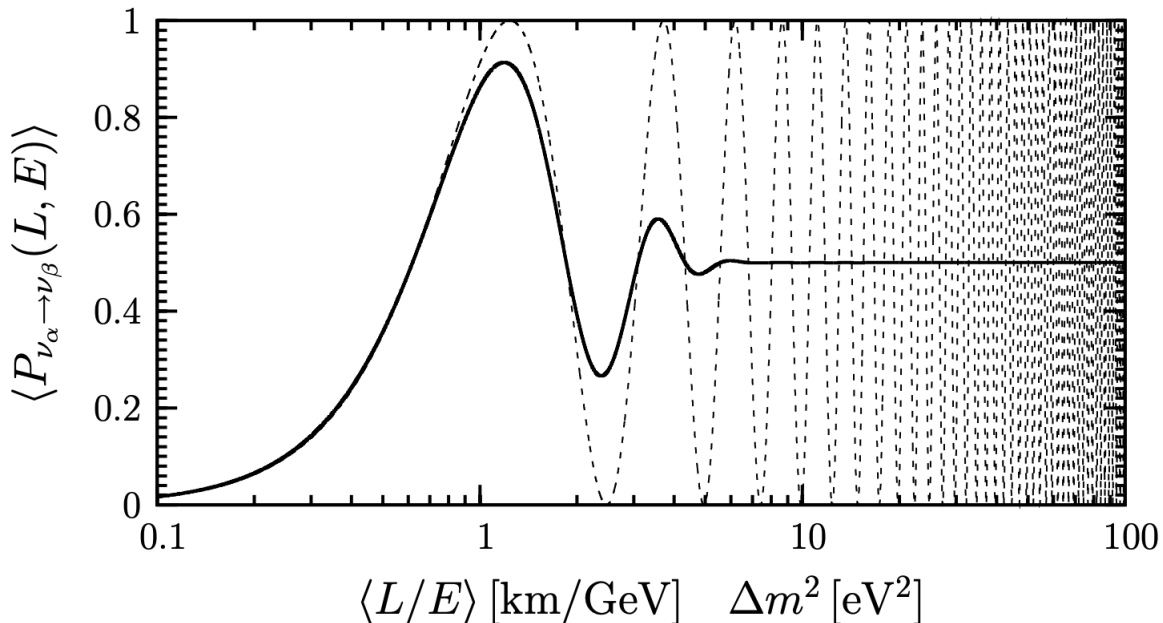
Fig. 1.1: Probability of the $\nu_\alpha \to \nu_\beta$ transition for $\sin^2 2\theta = 1$ as a function of $\langle L/E\rangle \, \Delta m^2$. Solid line: probability averaged over a Gaussian L/E distribution with $\sigma_{L/E} = 0.2 \, \langle L/E\rangle$. Dashed line: unaveraged transition probability where $L/E = \langle L/E\rangle$ [1].

1.2.1.3   Classes of oscillation experiments

As the oscillation phase only depends on the physical parameter Δm^2, experiments can be designed to be sensitive to different values of the squared-mass differences by having suitable values of the ratio L/E. This is because if

$$\frac{\Delta m^2 L}{2E} \ll 1, \tag{1.2.9}$$

the phase $\Phi \sim 0$ and transitions to different flavours have low probabilities as per eqn. (1.2.4). On the other hand, referring to eqns. (1.2.7-1.2.8), oscillations are averaged out for $\Delta m^2 L/2E \gg 1$ and do not depend on the squared-mass differences. Thus, the sensitivity to Δm^2, i.e. the value of Δm^2 for which

$$\frac{\Delta m^2 L}{2E} \sim 1, \tag{1.2.10}$$

represents one of the defining parameters of an oscillation experiment, as it determines the lower limit for the squared-mass differences that can be measured.

The different types of neutrino oscillation experiments are indeed classified according to the average value of their L/E ratio, which determines their sensitivity. In the fol-

lowing, the main classes of of oscillation experiments, depending on the sensitivity, will be presented, discussing briefly the possible design types.

Short Baseline experiments (SBL). Experiments reaching sensitivities of up to $\Delta m^2 \gtrsim 10^2 \, \text{eV}^2$, with source-detector distances below $\sim 1 \, \text{km}$. Depending on the neutrino source, which determines the energy, they are divided as follows:

- Reactor SBL: experiments that utilize the large fluxes of $\overline{\nu}_e$ produced in nuclear reactors. As the typical energy of reactor antineutrinos is of the order of a few MeV, baselines of $\sim 10 \, \text{m}$ give sensitivities to Δm^2 of

$$\frac{L}{E} \lesssim 10 \, \text{m/MeV} \quad \Rightarrow \quad \Delta m^2 \gtrsim 0.1 \, \text{eV}^2. \tag{1.2.11}$$

  As the antineutrino energies are too low to produce μ's or τ's, these experiments are limited to the $\bar{\nu}_e$ disappearance channel, which can be studied in liquid scintillator detectors through the inverse β-decay reaction.

- Accelerator SBL: experiments with neutrino beams produced by the decay of pions, kaons and muons created by a proton beam hitting a target. Two designs in this category, *Pion Decay In Flight* (DIF) and *Muon Decay At Rest* (DAR) experiments, depending on the reaction that the muon neutrino beams, reach sensitivities to Δm^2 of $\Delta m^2 \gtrsim 1 \, \text{eV}^2$, while *Beam Dump* experiments reach, thanks to neutrino energies of the order of $10^2 \, \text{GeV}$ and propagation distances $L \sim 1 \, \text{km}$ sensitivities of $\Delta m^2 \gtrsim 10^2 \, \text{eV}^2$. Depending on the energy and the composition of the neutrino flux, $\nu_\mu/\bar{\nu}_m u$ oscillations to electron and tau neutrinos and antineutrinos can be measured.

Long Baseline experiments (LBL). These experiments generally have the same sources, and thus energies, of SBL experiments, but with baselines larger by two or three orders of magnitude, reaching sensitivities of $\Delta m^2 \gtrsim 10^{-4} \, \text{eV}^2$. LBLs are divided into:

- Reactor LBL: experiments in which the detector distance from the reactor source is $L \sim 1 \, \text{km}$, allowing to cover the sensitivity range of $\Delta m^2 \gtrsim 10^{-3} \, \text{eV}^2$ with the $\bar{\nu}_e$-disappearance channel.

- Accelerator LBL: experiments in which the source-detector distance is about $10^2 - 10^3 \, \text{km}$, leading, for the $\sim 1 \, \text{GeV}$ energies of accelerator neutrinos, to

$$\frac{L}{E} \lesssim 10^3 \, \text{km/GeV} \quad \Rightarrow \quad \Delta m^2 \gtrsim 10^{-3} \, \text{eV}^2. \tag{1.2.12}$$

- Atmospheric Neutrino Experiments (ATM): experiments that detect the neutrinos coming from the decay of mesons produced in cosmic ray showers. The energies of

these neutrinos cover a wide range, $500\,\text{MeV} \lesssim E \lesssim 100\,\text{GeV}$, while the baseline varies from $L \sim 20\,\text{km}$ for neutrinos coming from the zenith, to $L \sim 1.3 \times 10^{-4}$ for those produced at the opposite side of the planet. Thus, in ATM experiments the sensitivities are typically of

$$\frac{L}{E} \lesssim 10^4\,\text{km/GeV} \quad \Rightarrow \quad \Delta m^2 \gtrsim 10^{-4}\,\text{eV}^2. \tag{1.2.13}$$

Very Long-Baseline experiments (VLB). Experiments with source-detector distances larger than for LBL experiments by one or two orders of magnitude. VLBs are divided into:

- Reactor VLB: experiments that measure the combined neutrino fluxes from many nuclear reactors at distances of the order of $100\,\text{km}$, allowing sensitivities of

$$\frac{L}{E} \lesssim 10^5\,\text{m/MeV} \quad \Rightarrow \quad \Delta m^2 \gtrsim 10^{-5}\,\text{eV}^2. \tag{1.2.14}$$

- Accelerator VLB: experiments in which accelerator neutrinos propagate for distances $L \sim 10^3\,\text{km}$, allowing to cover the sensitivity range of

$$\frac{L}{E} \lesssim 10^4\,\text{km/GeV} \quad \Rightarrow \quad \Delta m^2 \gtrsim 10^{-4}\,\text{eV}^2. \tag{1.2.15}$$

- Solar Neutrino Experiments (SOL): experiments that detect the neutrinos generated by the thermonuclear reaction cycle in the core of the Sun. As the energies of detectable solar neutrinos are in the range $0.2 - 15\,\text{MeV}$ and the Sun-Earth distance is about $1.5 \times 10^{11}\,\text{m}$, the theoretical sensitivity of SOL experiments is of

$$\frac{L}{E} \lesssim 10^{12}\,\text{m/MeV} \quad \Rightarrow \quad \Delta m^2 \gtrsim 10^{-12}\,\text{eV}^2, \tag{1.2.16}$$

much smaller than any other experiment discussed above.

1.2.1.4   Results of neutrino oscillation experiments

As the first phase in the history of neutrino oscillation experiments ended, with the results from Super-Kamiokande and SNO experiments, later confirmed by other collaborations, two main features of neutrinos had been proven: that neutrinos have small masses, so that flavour neutrinos are combinations of mass eigenstates, and that all observed data can be described assuming a three-neutrino mixing model [2].

Indeed, the data coming from the first solar and atmospheric neutrino experiments could be modelled, in a two-neutrino approximation, according to two separate sets of parameters: a solar mixing angle $\theta_\odot$ and mass difference $\Delta m_\odot^2$ and an atmospheric mixing angle

θ_{ATM} and mass difference Δm^2_{ATM}; this implied, clearly, the existence of three massive neutrino states.

In the following, the experimental results on the solar and atmospheric oscillation parameters will be presented, discussing subsequently how the measurement of the θ_{13} PMNS parameter in SBL experiments allows to fit them into the three-neutrino mixing framework.

Solar oscillation parameters. The Sun is a very powerful neutrino source, with the thermonuclear reactions in its core producing ν_e with energies of the order of $1\,\text{MeV}$. Despite the extremely large solar neutrino flux on Earth, of about $6 \times 10^{10}\,\text{cm}^{-2}\text{s}^{-1}$, the detection of solar neutrinos is difficult, requiring large underground detectors to compensate for the small neutrino interaction cross section and the background from cosmic rays interactions.

The first experiment to detect solar neutrinos, the Homestake Mine radiochemical experiment, was meant to test the Standard solar model of thermonuclear reactions, but found instead a deficit of observed ν_e with respect to the predictions of this model [6]. This so-called *Solar neutrino problem* was later confirmed by radiochemical experiments (GALLEX/GNO and SAGE [7, 8]) and Cherenkov detectors (Kamiokande and Super-Kamiokande [9, 10]), and finally explained by the SNO experiment as due to neutrino oscillations [11].

As anticipated, the solar neutrino oscillation data can be modelled, in a first order approximation, as the result of two-neutrino mixing with the parameters $\Delta m^2_\odot$ and $\theta_\odot$, with the best estimates given by a global fit that includes SNO-III and KamLAND data:

$$\Delta m^2_\odot = +7.59^{+0.19}_{-0.21} \times 10^{-5}\text{eV}^2, \quad \theta_\odot = 34.4^{+1.3}_{-1.2}, \tag{1.2.17}$$

having thus a quite large but not maximal mixing angle [12]. Fig. 1.2 shows the allowed regions for the solar oscillation parameters obtained from the global analysis and the KamLAND data.

The sign of the squared-mass difference could be determined thanks to the *Mikheev-Smirnov-Wolfenstein* (MSW) *effect* which introduces a dependence on Δm^2 due to the interaction of neutrinos inside the solar volume. As the nuclear reactions in the Sun produce ν_e, the composition of the neutrino state exiting the Sun is given, in a two-neutrino framework, by a superposition ν_X of ν_μ and ν_τ flavour and it depends on the relative size of $\Delta m^2_\odot \cos 2\theta_\odot$ versus the value of the interaction potential at the production point close to the solar core, $A_0 = 2EG_F n_{e,0}$, $n_{e,0}$ being the corresponding electron density. In particular, if the matter potential at production is well below the *resonant value* $A_R = \Delta m^2 \cos 2\theta$, matter effects are negligible.

In the case, instead, of $A_R = \Delta m^2 \cos 2\theta < A_0$, neutrinos can cross the resonant condition on their way out of the Sun, as n_e decreases farther from the center. As the behaviour of the survival probability measured by experiments is consistent with

such a crossing for $E > 10\,\mathrm{MeV}$, it follows from the definition of A_R that the product $\Delta m^2 \cos 2\theta$ must be positive, as the electron-ν_e interaction potential is positive; therefore, as $\cos 2\theta_\odot > 0$, as shown in the following, $\Delta m_\odot^2$ must too be positive [3, 13, 14].
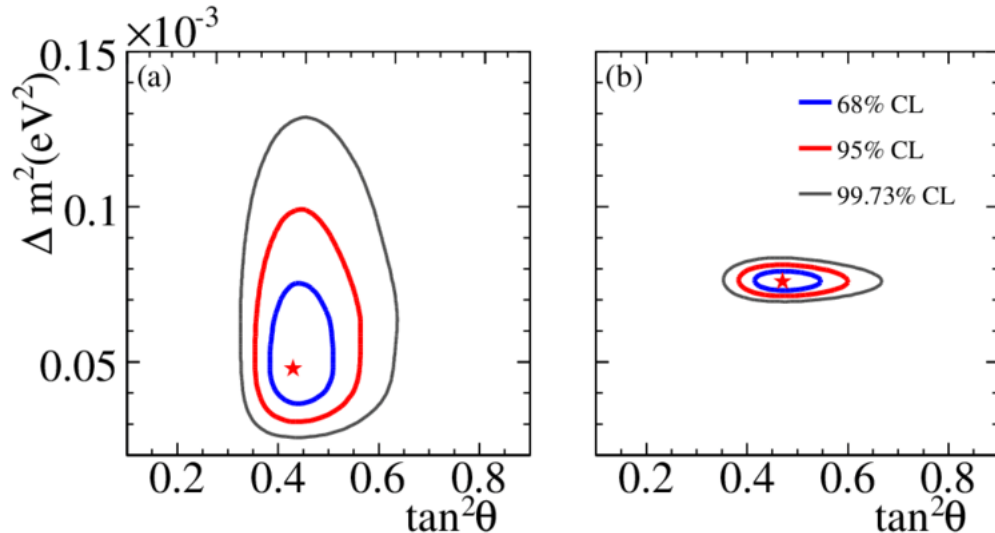
Fig. 1.2: Allowed regions for the solar oscillation parameters. (a) The global solar analysis including rate measurements from Homestake, Gallex, GNO, Sage and Borexino, SK-I zenith energy spectra, SNO-I summed kinetic energy spectra, NC, ES fluxes and CC kinetic energy spectra from SNO-II, CC, ES and NC fluxes from SNO-III. The best fit point is: $\Delta m_\odot^2 = 4.90 \times 10^{-5}\,\mathrm{eV}^2$, $\tan^2\theta_\odot = 0.437$. (b) KamLAND data are included; the best fit is: $\Delta m_\odot^2 = 7.59 \times 10^{-5}\,\mathrm{eV}^2$, $\tan^2\theta_\odot = 0.468$ [12].

Atmospheric oscillation parameters. The large underground Cherenkov experiments that came online in the second half of the 1980s, Kamiokande and IMB, performed the first observations of atmospheric neutrinos: they measured, however, a deficit of ν_μ interactions with respect to the prediction based on the cosmic ray spectrum.

The breakthrough for the solution of this so-called *atmospheric neutrino anomaly* came from the data of Super-Kamiokande (SK), the follow-up experiment to Kamiokande, which revealed an up-down asymmetry in muon neutrino events, a clear effect of atmospheric neutrino oscillations [15]. The SK experiment has provided, so far, high-statistics data on the flux of atmospheric neutrino flux, allowing to model the oscillations as from muon to tau neutrinos and to infer the values of the oscillation parameters with significant accuracy. The SK results have also been corroborated by those of other ATM experiments, such as Soudan 2 [16] and MACRO [17], as well as LBL accelerator experiments like K2K [18].

As with the solar oscillations, atmospheric neutrino oscillations could be modelled in a two-neutrino approximation: the data collected during the first phase of the SK experiments yielded the following 90% CL ranges for the atmospheric oscillation parameters [19]:

$$\sin^2 2\theta > 0.92, \quad 1.5 \times 10^{-3} < |\Delta m^2_{ATM}| < 3.4 \times 10^{-3} \, \text{eV}^2. \tag{1.2.18}$$

Fig 1.3 shows the 90% CL allowed region of the atmospheric $\nu_\nu \leftrightarrow \nu_\tau$ oscillation parameters, obtained from the SK data in [19], for six subsamples of the events with distinct topologies. The combined analysis defines the constraints in eqn. (1.2.18).
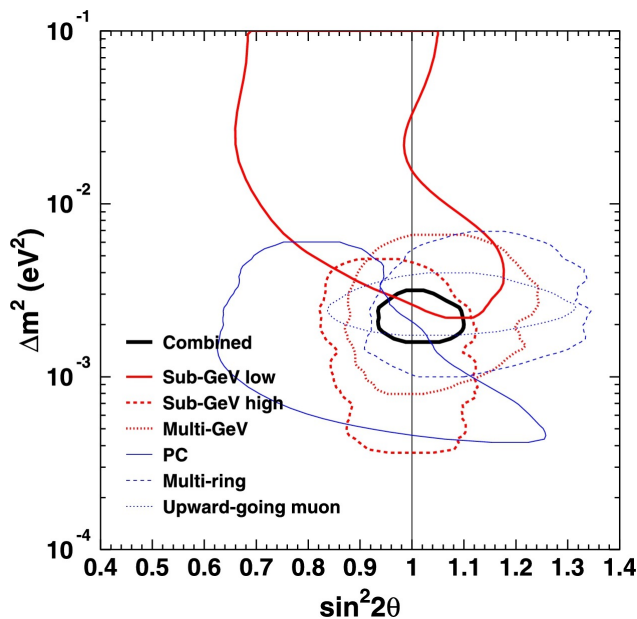
Fig. 1.3: 90% CL allowed oscillation parameter regions for $\nu_\nu \leftrightarrow \nu_\tau$ oscillations from six sub-samples. The bold region is the interval in which all samples simultaneously fit [19].

Three-neutrino analysis. The minimal possibility of just the two independent squared-mass differences $\Delta m^2_\odot$ and Δm^2_{ATM} is realized in the three neutrino mixing framework, which has been introduced in Section 1.1.2.

The solar and atmospheric squared-mass differences can be arbitrarily labelled so as to have

$$\Delta m^2_\odot \equiv \Delta m^2_{21}, \quad \Delta m^2_{ATM} \equiv |\Delta m^2_{31}|, \tag{1.2.19}$$

so that, from eqns. (1.2.17-1.2.18):

$$\Delta m^2_{21} \ll \Delta m^2_{31} \simeq \Delta m^2_{32}. \tag{1.2.20}$$

As the PMNS matrix features three mixing angles, replacing the separate solar and atmospheric two-neutrino analyses with a combined three-neutrino one, could have drastically changed the information on the mixing. This was not the case as $|U_{e3}|$ is small, as will be discussed in the following.

Indeed, as solar neutrino experiments are limited to the ν_e disappearance channel, the oscillation probabilities only depend on the first row U_{ej} of the PMNS. The probabilities for atmospheric neutrino experiments depend instead on the θ_{13} and θ_{23} angles, which are determined by the third column of the PMNS through

$$\sin\theta_{23} = \frac{|U_{\mu3}|}{\sqrt{1-|U_{e3}|}}, \quad \sin\theta_{13} = |U_{e3}|. \tag{1.2.21}$$

Therefore $|U_{e3}|$ is the only element that correlates solar and atmospheric neutrino oscillations [1]. In addition to that, $\sin\theta_{13}$ multiplies the CP violating phase, thus determining whether CP violation in the lepton sector is experimentally observable. Another problem, the solution of which requires θ_{13} to be nonzero is that of the neutrino mass ordering, as will be discussed in Section 1.2.1.5 [2].

The experiments that can provide the most precise determination of the θ_{13} angle are Medium Baseline reactor experiments, having $L \sim 1\,\mathrm{km}$, for which the ν_e survival probability can be approximated as

$$P_{\nu_e \to \nu_e} \simeq 1 - \sin^2 2\theta_{13}\sin^2\left(\frac{\Delta m_{ee}^2 L}{4E}\right)$$

where

$$\Delta m_{ee}^2 = \cos^2\theta_{12}\Delta m_{31}^2 + \sin^2\theta_{12}\Delta m_{32}^2 \tag{1.2.22}$$

The θ_{13} angle was successfully measured by the Daya Bay [20], RENO [21] and D-Chooz [22] experiments for the best-fit values shown in Tab 1.1 [2, 3]. The small value of the

θ_{13} measurements	
Daya Bay	$\sin^2 2\theta_{13} = 0.084 \pm 0.0027\,(\text{stat}) \pm 0.0019\,(\text{syst})$
RENO	$\sin^2 2\theta_{13} = 0.082 \pm 0.009\,(\text{stat}) \pm 0.006\,(\text{syst})$
D-Chooz	$\sin^2 2\theta_{13} = 0.111 \pm 0.018\,(\text{stat+syst})$

Table 1.1: $\sin^2\theta_{13}$ parameters obtained from the Daya Bay, RENO and D-Chooz experiments: Daya Bay imposed the most stringent constraints on the mixing angle [2].

θ_{13} angle thus justifies the independence, to the leading order, of solar and atmospheric neutrino oscillations, with the remaining PMNS mixing angles being approximately

$$\theta_{12} \simeq \theta_\odot \quad \text{and} \quad \theta_{23} \simeq \theta_{ATM}. \tag{1.2.23}$$

Having established the validity of the three-neutrino mixing framework, the data of VLB and LBL can be used, together with the measurements of θ_{13} to give the following global best-fit values for θ_{12} and θ_{23} [3]:

$$\begin{aligned}
\sin^2\theta_{12} &= 0.310^{+0.013}_{-0.012}, \quad \text{i.e.} \quad \theta_{12}/^\circ = 33.82^{0.78}_{-0.76} \\
\sin^2\theta_{23} &= 0.558^{+0.020}_{-0.033}, \quad \text{i.e.} \quad \theta_{23}/^\circ = 48.3^{+1.2}_{-1.9}
\end{aligned} \tag{1.2.24}$$

The determination of the parameters of the neutrino sector requires a global analysis of the data from the different experiments, with slightly variations depending on the statistical analyses and data samples used by the different groups. Tab. 1.2 presents the latest global analysis results, with the exclusion of the Super-Kamiokande data: the estimates depend on the *Mass ordering* of the massive neutrinos, with *Normal ordering* (NO) being

$$\Delta m^2_{32} < 0, \Delta m^2_{21} > 0 \Longrightarrow m_1 < m_2 < m_3 \tag{1.2.25}$$

and *Inverted Ordering* (IO) being

$$\Delta m^2_{32} \simeq \Delta m^2_{31} > 0, \Delta m^2_{21} > 0 \Longrightarrow m_3 < m_1 < m_2, \tag{1.2.26}$$

where, thus far, only $m_2 > m_1$ has been determined. Fig. 1.4 illustrates the currently determined patterns of NO and IO squared-mass differences and flavour mixing. The global analysis finds the best fits for the NO hypothesis, with the IO being disfavoured by $\Delta\chi^2 = 6.2$ [3].
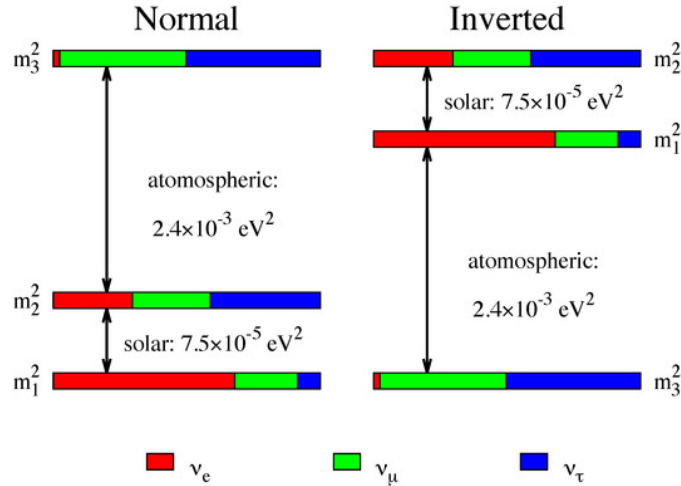
Fig. 1.4: Neutrino mass eigenstate flavour composition and mass pattern in the two cases of Normal Ordering (left) and Inverted Ordering (right) [24].

Normal ordering (NO)		
Parameters	best fit param. $\pm 1\sigma$	3σ range
$\theta_{12}/°$	$33.82^{+0.78}_{-0.76}$	$31.61 \to 36.27$
$\theta_{23}/°$	$48.3^{+1.2}_{-1.9}$	$40.8 \to 51.3$
$\theta_{13}/°$	$8.61^{+0.13}_{-0.13}$	$8.22 \to 8.99$
$\delta_{CP}/°$	222^{+38}_{-28}	$141 \to 370$
$\Delta m_{21}^2/(10^{-5}\,\mathrm{eV}^2)$	$7.39^{+0.21}_{-0.20}$	$6.79 \to 8.01$
$\Delta m_{32}^2/(10^{-3}\,\mathrm{eV}^2)$	$2.449^{+0.032}_{-0.030}$	$2.358 \to 2.544$
Inverted ordering (IO)		
Parameters	best fit param. $\pm 1\sigma$	3σ range
$\theta_{12}/°$	$33.82^{+0.78}_{-0.76}$	$31.61 \to 36.27$
$\theta_{23}/°$	$48.6^{+1.1}_{-1.5}$	$41.0 \to 51.5$
$\theta_{13}/°$	$8.65^{+0.13}_{-0.12}$	$8.26 \to 9.02$
$\delta_{CP}/°$	285^{+24}_{-26}	$205 \to 354$
$\Delta m_{21}^2/(10^{-5}\,\mathrm{eV}^2)$	$7.39^{+0.21}_{-0.20}$	$6.79 \to 8.01$
$\Delta m_{32}^2/(10^{-3}\,\mathrm{eV}^2)$	$-2.509^{+0.032}_{-0.032}$	$-2.603 \to -2.416$

Table 1.2: Three-neutrino oscillation parameters obtained from the global fit analysis in [23] excluding the SK data, in the assumption of NO and IO respectively [3].

1.2.1.5   Known Unknowns

Despite the high sensitivity reached in the determination of most of the neutrino oscillation parameters, three of them still require further investigation. Recalling Tab. 1.2 these so-called *known unknowns* are the neutrino mass ordering, the octant of θ_{23} and the CP violating phase δ_{CP} of the lepton sector. In the following, the current results on the three *known unknowns* are presented, as well as the experimental strategies that future experiments will use to finally determine these parameters.

The octant of θ_{23}.   The θ_{23} mixing angle can be studied at long baselines via the $\nu_\mu \to \nu_e$ and $\bar{\nu}_\mu \to \bar{\nu}_e$ oscillation channels, which are open to both atmospheric and accelerator neutrino experiments. Indeed, the ν_μ disappearance and ν_e appearance probabilities can

be approximated, being $\Delta m_{21}^2 / \Delta m_{31}^2 \ll 1/30 \ll 1$, as:

$$P(\nu_\mu \to \nu_\mu) \simeq 1 - \sin^2 2\theta_{23} \sin^2 \left(\frac{\Delta m_{31}^2 L}{4E} \right)$$

$$P(\nu_\mu \to \nu_e) \simeq \sin^2 \theta_{23} \sin^2 2\theta_{13} \sin^2 \left(\frac{\Delta m_{31}^2 L}{4E} \right)$$

(1.2.27)

where matter and δ_{CP}-related terms have been neglected. Disappearance experiments are capable of determining both Δm_{31}^2 and $\sin^2 2\theta_{23}$ with high accuracies. It is then easy to notice that, for $\theta_{23} \neq \pi/4$, there is a twofold solution of θ_{23} for a certain value of $\sin^2 2\theta_{23}$:

$$\sin^2 \theta_{23} = \frac{1}{2} \left[1 \pm \sqrt{1 - \sin^2 2\theta_{23}} \right],$$

(1.2.28)

leading to the so-called *octant degeneracy*, as the two solutions for θ_{23} are either below 45° (*first octant*) or above it (*second octant*).

The degeneracy can be lifted by combining the results of the ν_μ disappearance and ν_e appearance channels, the latter depending on $\sin^2 \theta_{23} \sin^2 2\theta_{13}$, with the independent measurements of θ_{13} from reactor experiments, discussed in Section 1.2.1.4 [25].

Despite all analyses finding some preference for $\theta_{23} > 45°$, values of θ_{23} smaller, larger or equal to $\pi/4$ are still all consistent at the 3σ level. With the current data, the status of the maximality/non-maximality of the θ_{23} mixing angle is thus quite delicate; this might change, however, with the implementation of T2K data [26] in the global fit [3, 27].

Mass ordering determination. In all analyses so far the best fit is for the Normal mass ordering, with the IO being disfavoured with a $\Delta\chi^2$ ranging from $\sim 2\sigma$, driven by the interplay of LBL accelerator and SBL reactor data, to 3σ when including the atmospheric SK data. Current experiments, though, display too much of a limited individual sensitivity for the discrimination to be finally resolved [3, 27].

In order to resolve the mass ordering, the next generation of experiments will thus focus on three different oscillation configurations [28]:

- Medium baseline ($L \sim 50$ km) reactor $\bar{\nu}_e \to \bar{\nu}_e$ oscillations, will be studied by the JUNO [28] and RENO-50 [29] experiments.

- Long baseline accelerator muon (anti-)neutrino $\overset{(-)}{\nu}_\mu \to \overset{(-)}{\nu}_e$ oscillations at experiments like the already running NOνA [30] and the future DUNE [31].

- Atmospheric (anti-)neutrino oscillations with the same channel as above, studied by experiments such as PINGU, ORCA, DUNE and Hyper-K [31–35].

The medium baseline experimental channel relies on the oscillation interference between Δm_{31}^2 and Δm_{32}^2, allowed by the nonzero value of θ_{13}. The survival probability of reactor antineutrinos can be written as:

$$
\begin{aligned}
P_{\bar{\nu}_e \to \bar{\nu}_e} \simeq\ & 1 - \cos^4 \theta_{13} \sin^2 2\theta_{12} \sin^2 \left(\frac{\Delta m_{21}^2 L}{4E} \right) \\
& - \sin^2 2\theta_{13} \sin^2 \left(\frac{\Delta m_{31}^2 L}{4E} \right) \\
& - \sin^2 \theta_{12} \sin^2 2\theta_{13} \sin^2 \left(\frac{\Delta m_{21}^2 L}{4E} \right) \cos \left(\frac{2|\Delta m_{31}^2|L}{4E} \right) \\
& \pm \frac{\sin^2 \theta_{12}}{2} \sin^2 2\theta_{13} \sin \left(\frac{2\Delta m_{21}^2 L}{4E} \right) \sin \left(\frac{2|\Delta m_{31}^2|L}{4E} \right)
\end{aligned}
\tag{1.2.29}
$$

where the $\pm$ at the fourth term distinguishes the normal and inverted ordering. This probability does not depend on the δ_{CP} phase and the MSW effect is negligible for the baselines in question. Fig. 1.5 illustrates the reactor neutrino energy spectra for both orderings compared to the unoscillated spectrum as a function of the L/E ratio.

The two experiments that are planning to leverage this channel are JUNO, in China and RENO-50 in South Korea: their source-detector distance of $\sim 50\,\mathrm{km}$ maximises the mass ordering interference term and using large ($\sim 20\,\mathrm{kt}$) liquid scintillator detectors allows to reach the required high energy resolution [36].
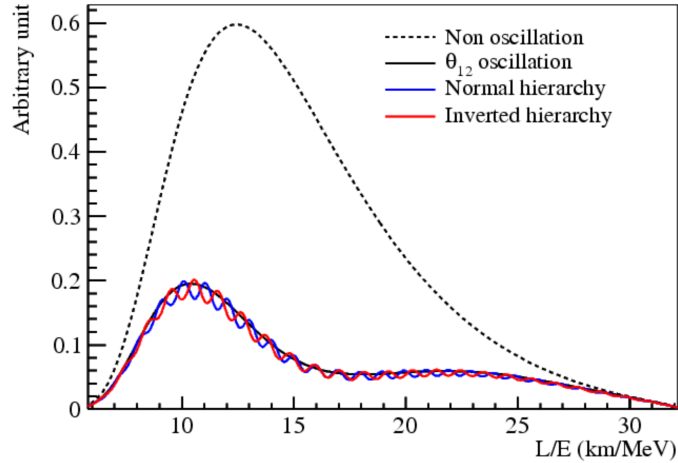
Fig. 1.5: Relative shape difference of the reactor $\bar{\nu}_e$ flux for the two mass orderings. The spectra are given as the product of neutrino flux times interaction cross section times survival probability [24].

The second and third experiment types will leverage the *matter effect* of neutrino propagation in the Earth crust at Long Baselines in the $\overset{(-)}{\nu}_\mu \to \overset{(-)}{\nu}_e$ channels. Assuming a

constant matter density, the oscillation probability can be expanded to the second order in the small parameters θ_{13} and $\alpha \equiv \Delta m_{21}^2 / \Delta m_{31}^2$ to:

$$
\begin{aligned}
P_{\nu_\mu \to \nu_e, (\bar{\nu}_\mu \to \bar{\nu}_e)} \simeq \, & 4 \sin^2 \theta_{13} \sin^2 \theta_{23} \frac{\sin^2 \Delta}{(1-A)^2} \\
& + \alpha^2 \sin^2 2\theta_{12} \cos^2 \theta_{23} \frac{\sin^2 A\Delta}{A^2} \\
& + 8\alpha J_{CP}^{max} \cos(\Delta \pm \delta_{CP}) \frac{\sin \Delta A}{A} \frac{\sin \Delta(1-A)}{1-A},
\end{aligned}
\tag{1.2.30}
$$

with

$$
J_{CP}^{max} = \cos \theta_{12} \sin \theta_{12} \cos \theta_{23} \sin \theta_{23} \cos^2 \theta_{13} \sin \theta_{13}
\tag{1.2.31}
$$

and

$$
\Delta \equiv \frac{\Delta m_{31}^2 L}{4E}, \quad A \equiv \frac{2EV}{\Delta m_{31}^2},
\tag{1.2.32}
$$

where V is the effective matter potential in the Earth crust and the $+$ $(-)$ in the third term is for the neutrino (antineutrino) channel. In this expression α, Δ and A are sensitive to the sign of Δm_{32}^2 and therefore to the mass ordering. The probability is also dependent on the CP violating phase of the lepton sector: indeed, as discussed in the following, results on $\overset{(-)}{\nu_e}$-appearance at LBL experiments provide the dominant information on δ_{CP} [3]. Fig. 1.6 illustrates the appearance probabilities for ν_e and $\bar{\nu}_e$ in both mass ordering possibilities and for several values of δ_{CP}.

The determination of the mass ordering is thus a crucial factor for measuring the δ_{CP} phase, as it appears in the same expressions for LBL oscillations as the latter: this could lead to degenerate solutions for the ordering and CP phase merge. An independent measurement, e.g. from medium baseline experiments, is thus important [28].

CP **violation.** As discussed in Section 1.1.3, the discovery of neutrino oscillations opened up the possibility of CP symmetry being violated also in the lepton sector. The subsequent measurement of a nonzero value for all mixing angles implies that an experimental determination of δ_{CP} might be possible.

CP invariance can be tested by comparing neutrino and antineutrino channels $P_{\nu_\alpha \to \nu_\beta}$ and $P_{\bar{\nu}_\alpha \to \bar{\nu}_\beta}$ and searching for the asymmetry [38]:

$$
\Delta_{\alpha\beta}^{CP} = P_{(\nu_\alpha \to \nu_\beta, L)} - P_{(\bar{\nu}_\alpha \to \bar{\nu}_\beta, L)}.
\tag{1.2.33}
$$

The current LBL experiments utilize $\overset{(-)}{\nu_\mu}$ beams and can therefore study this asymmetry through the $\overset{(-)}{\nu_e}$-appearance and $\overset{(-)}{\nu_\mu}$-disappearance channels. The dependence on
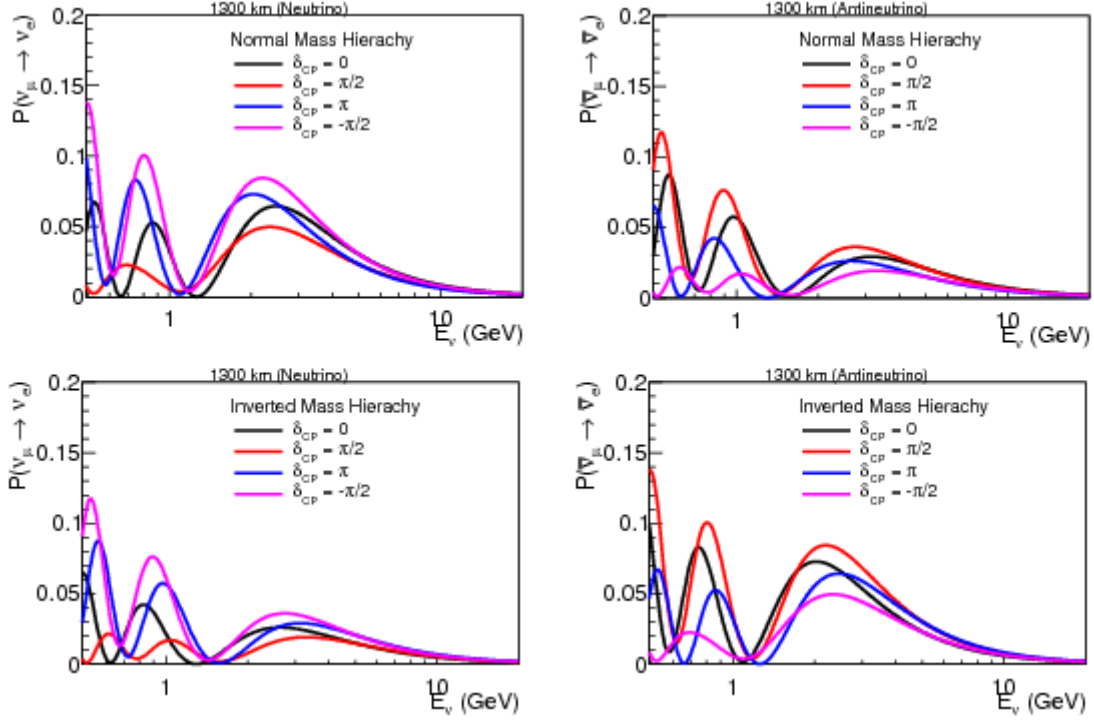
Fig. 1.6: Electron neutrino and antineutrino appearance probabilities as a function of the neutrino energy E_ν at the baseline of the future DUNE experiment $L = 1300\,\text{km}$ and for the indicated values of δ_{CP}. Top (bottom) panels correspond to NO (IO) while left (right) panels to ν_e ($\bar{\nu}_e$). In the NO (IO), the ν_e ($\bar{\nu}_e$) appearance is enhanced, while that of $\bar{\nu}_e$ (ν_e) is suppressed [37].

δ_{CP} of the oscillation probabilities is then given by eqn. (1.2.30), which, neglecting the matter effect, becomes:

$$
\begin{aligned}
P_{\nu_\mu \to \nu_e, (\bar{\nu}_\mu \to \bar{\nu}_e)} \simeq{}& \sin^2\theta_{23} \sin^2 2\theta_{13} \sin^2\Delta \\
&\pm \frac{\sin 2\theta_{12} \sin 2\theta_{23}}{2\sin\theta_{13}} \sin\frac{\Delta m_{21}^2}{4E} \sin^2 2\theta_{13} \sin^2\Delta \sin\delta_{CP} \\
&+ (CP \text{ conserving term, solar term, matter term})
\end{aligned}
\tag{1.2.34}
$$

where Δ is defined in eqn. (1.2.32) and the $+$ $(-)$ sign in the second term is for the neutrino (antineutrino) channel [39].

From eqn. (1.2.34) the following CP violation asymmetry can be defined:

$$
A_{CP} \equiv \frac{P(\nu_\mu \to \nu_e) - P(\bar{\nu}_\mu \to \bar{\nu}_e)}{P(\nu_\mu \to \nu_e) + P(\bar{\nu}_\mu \to \bar{\nu}_e)}
\tag{1.2.35}
$$

29

which, to the leading order in Δm_{21}^2, is given by:

$$A_{CP} \simeq \frac{\cos\theta_{21}\sin 2\theta 12 \sin\delta_{CP}}{\sin\theta_{23}\sin\theta_{13}}\left(\frac{\Delta m_{12}^2 L}{4E}\right) \qquad (1.2.36)$$
$$+\text{ matter terms}$$

thus growing linearly with the distance L [40].

The best fit for the complex phase of the PMNS is at $\delta_{CP} \sim 120°$, but CP conservation is still allowed at a confidence level (CL) of $1-2\sigma$. The significance of CP violation has recently been reduced in the global analysis with respect to the one reported by T2K [41], as NOνA data does not show a significant indication of CP violation[3].

In the three-neutrino framework, CP violation can be quantified, as discussed in Section 1.1.3, in terms of the leptonic Jarlskog invariant

$$J \equiv \text{Im}\left[U_{e2}U_{e3}^* U_{\mu 2}^* U_{\mu 3}\right] = J_{CP}^{max}\sin\delta_{CP} \qquad (1.2.37)$$

where the definition of $J_{CP}^{\max}$ in eqn. (1.2.31) has been used. The global analysis in [23],finds for J_{CP}^{max} a value of

$$J_{CP}^{\max} = 0.03359 \pm 0.0006\,(\pm 0.0019), \qquad (1.2.38)$$

at 1σ (3σ) for both mass orderings, so that the preference of present data for nonzero δ_{CP} implies a nonzero best fit value for J of $J^{\text{best}} = -0.0019$.

The status of the determination of CP violation in the lepton sector is illustrated by the *leptonic unitarity triangle* in Fig. 1.7: the triangle corresponding to the unitarity conditions for the first and third columns of the PMNS matrix, as in the quark sector. In this plot the absence of CP violation would result in a flat triangle, so that the confidence level of CP violation observation would be given by the confidence level at which the region crosses the horizontal axis.

Both leading LBL experiments in the search for leptonic CP violation, T2K and NOνA,will be operating until 2024-2026. T2K will undergo a beam and near detector upgrade, with the projected amount of data to be gathered by 2026 allowing a sensitivity larger than 3σ for the exclusion of $\sin\delta_{CP} = 0$. NoνA should instead be able to reach a 2σ significance to disfavour CP conservation. Both experiment, though, only have the *indication potential* for the search of CP violation, being unable to measure δ_{CP} with a 5σ significance.

The next generation of LBL experiment is thus needed to perform the measurement, with two major project being in development [39]:

- Hyper-Kamiokande: the continuation of the T2K experiment with an upgraded $1.3\,\text{MW}$ neutrino beam and a $\sim 500\,\text{kt}$ far detector with the same technology as SK. The goal of the data-taking, which should start in 2026, is to reach an uncertainty on δ_{CP} as low as $7-21$ degrees over 10 years of running [35].
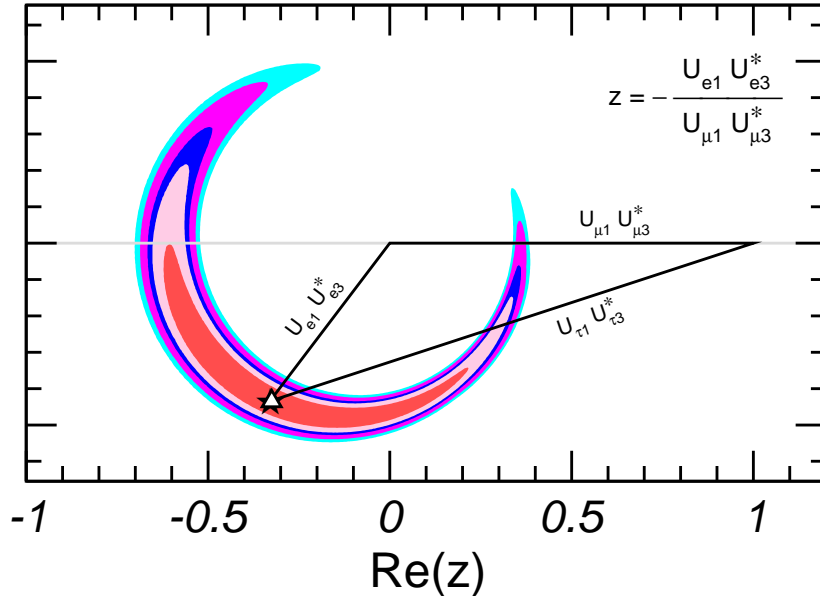
Fig. 1.7: Leptonic unitarity triangle for the first and third columns of the PMNS matrix. The triangle is scaled and rotated in order to have two vertices coinciding with (0,0) and (1,0). The 1σ, 90%, 2σ, 99% and 3σ CL allowed regions of the third vertex are given, assuming NO [3].

- DUNE: which will use a $1300\,\mathrm{km}$ baseline for the neutrino beam produced at Fermilab, with a $40\,\mathrm{kt}$ LAr far detector located at SURF. The expected resolution on δ_{CP} over 10 years of exposure is set to reach $6-10$ degrees [31]. DUNE will be the subject of the remainder of this thesis work.

1.2.2 Laboratory probes of neutrino masses

As described in the previous sections, the oscillations of neutrino flavours in vacuum and in matter only depend on the differences between the squared-masses and on the PMNS matrix elements. They are, conversely, insensitive to the absolute mass scales of neutrinos and to their Dirac or Majorana nature.

While flavour oscillations imply a lower bound on the mass of the heavier neutrino in Δm_{ij}^2, as trivially it must be $|m_i| \geqslant \sqrt{\Delta m_{ij}^2}$ for $\Delta m_{ij}^2 > 0$, there is no upper bound on m_i. Information on the absolute scale and production mechanism of neutrino masses has to be provided via other types of experiments. The following will provide a brief summary of the most sensitive probes of the mass scale and potential Majorana nature of neutrinos that can be explored in laboratory experiments.

1.2.2.1 Kinematics of weak decays

The only way to obtain model-independent information on neutrino masses is through the kinematics of reactions involving neutrinos or antineutrinos, which yield a bound on an *effective mass* for the flavour neutrino states.

The β decay of ^{3}H has proved, so far, the optimal channel for this search: being a superallowed decay, the electron spectrum is determined exclusively by the phase space:

$$
\begin{aligned}
\frac{dN_e}{dE} &= CpE(Q-T)\sqrt{(Q-T)^2 - (m_{\nu_e}^{\text{eff}})^2}F(E) \\
&\equiv R(E)\sqrt{(E_0 - E)^2 - (m_{\nu_e}^{\text{eff}})^2},
\end{aligned}
\tag{1.2.39}
$$

where E_0 is the mass difference between the initial and final nucleus, $E = T + m_e$ is the total electron energy, $Q \equiv E_0 - m_e$ is the maximum kinetic energy of the electron and $F(E)$ is the *Fermi function* containing the final state Coulomb interactions, so that $F(E)$ contains all the m_ν-dependent factors.

Defining the *Kurie Function* $K(T) \equiv \sqrt{\frac{dN}{dE}\frac{1}{pEF(E)}}$, it follows from eqn. (1.2.39) that $m_{\nu_e}^{\text{eff}} = 0$ would lead to a linear dependence of $K(T)$ on T, while a non-vanishing antineutrino mass introduces a distortion at the end point, with the maximum electron kinetic energy being $T_{max} = Q - m_{\nu_e}^{\text{eff}}$ instead of Q. As the ^{3}H decay has a very small Q-value, $Q = 18.6\,\text{keV}$, it is more sensitive to the $m_{\nu_e}^{\text{eff}}$ distortion.

The KATRIN experiment has provided the most recent results on the neutrino mass search in the ^{3}H decay, not yet finding an indication for $m_{\nu_e} \neq 0$ and setting the upper limit

$$
m_{\nu_e}^{\text{eff}} < 1.1\,\text{eV},
\tag{1.2.40}
$$

at 90% CL [42]. KATRIN is still running, with an estimated sensitivity limit of $m_{\nu_e}^{\text{eff}} \sim 0.2\,\text{eV}$. An alternative channel to the decay of ^{3}H is ^{163}Ho, which undergoes electron capture to ^{163}Dy with a smaller $Q = 2.8\,\text{keV}$ and allows to determine the effective mass for ν_e. The ECHo, HOLMES and NuMECS experiments are currently probing this channel, with techniques that are complementary to tritium decay experiments [43–45].

The effective masses of ν_μ and ν_τ have been studied through kinematical techniques as well, albeit imposing much weaker upper bounds:

$$
\begin{aligned}
m_{\nu_\mu}^{\text{eff}} &< 190\,\text{keV}\,(90\%\,\text{CL}) && \text{from} \quad \pi^- \to \mu^- + \bar{\nu}_\mu, \\
m_{\nu_e}^{\text{eff}} &< 18.2\,\text{MeV}\,(95\%\,\text{CL}) && \text{from} \quad \tau^- \to n\pi + \nu_\tau.
\end{aligned}
\tag{1.2.41}
$$

Given the present knowledge of the neutrino mass differences and PMNS parameters from oscillation experiments, the information on m_{ν_e} can be translated on a corresponding range for the lightest neutrino mass which depends on the mass ordering. In Fig. 1.8-left the allowed regions of the analysis in [23] are recast in terms of the allowed range of m_{ν_e} as a function of the lightest neutrino mass $m_{\text{ligth}} \equiv m_0$: the results of

oscillation experiments thus imply a lower bound at 95% CL on $m_{\nu_e} > 0.048$ (0.0085) eV for IO (NO) [3].
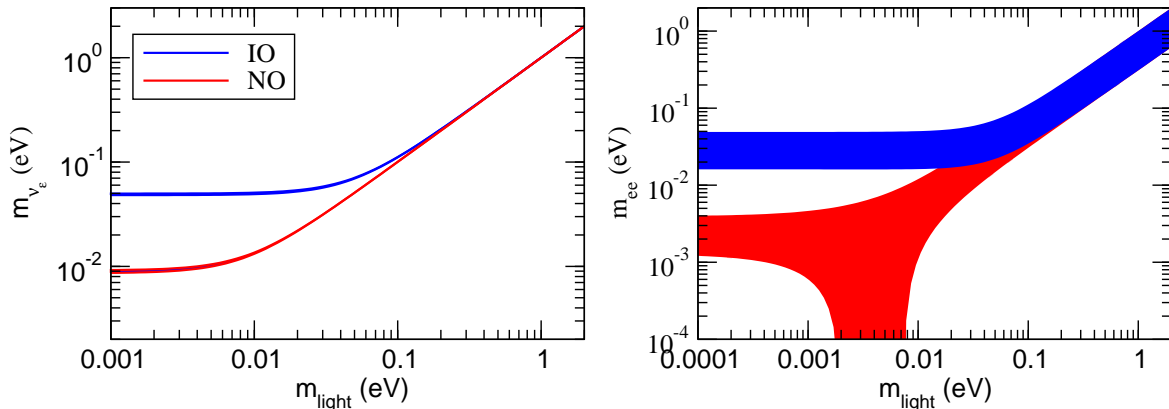
Fig. 1.8: Allowed 95% CL range for the $m_{\bar{\nu}_e}$ effective mass observable determined in ^{3}H (left) and in $0\nu\beta\beta$ decay (right) in the framework of three-neutrino mixing as a function of the lightest neutrino mass m_{light}. The ranges are obtained from the projections of the global analysis in [23] with each ordering defined with respect to its local minimum [3].

1.2.2.2 Majorana neutrinos

The most sensitive probe to the potential Majorana nature of neutrinos is the neutrinoless double beta decay ($0\nu\beta\beta$):

$$(A, Z) \to (A, Z + 2) + e^- + e^-, \tag{1.2.42}$$

which can only arise if neutrinos antineutrinos are described by the same field and the lepton number can be violated, as is the case for Majorana neutrinos, discussed in Section 1.1.4.

The observable in $0\nu\beta\beta$ experiments is the half-life of the decay, which, under the assumption that the Majorana mass term is the only source of lepton number violation, is given by:

$$(T_{1/2}^{0\nu})^{-1} = G^{0\nu} |M^{0\nu}|^2 \left(\frac{m_{ee}}{m_e} \right)^2, \tag{1.2.43}$$

where $G^{0\nu}$ is the phase space integral that includes the final atomic state, $|M^{0\nu}|$ is the nuclear matrix element of the transition and m_{ee} is the effective Majorana mass of ν_e, which depends on the extra Majorana complex phases in addition to the masses and PMNS parameters.

In Fig. 1.8-right the allowed regions for m_{ee} as a function of m_{light} according to the global analysis in [23] are plotted: the allowed range is substantially broader than that

33

of $m_{\bar{\nu}_e}$ for a given value of m_{light} as a consequence of the unknown Majorana phases. While for IO the global analysis implies a lower bound of $m_{ee} > 0.016\,\text{eV}$ at 95% CL, in the NO case the constraints reach down to $m_{ee} = 0$, in which case the observation of $0\nu\beta\beta$ would be impossible.

The strongest bound currently imposed on $0\nu\beta\beta$ lifetimes comes from the KamLAND-Zen experiment [46] which, searching for the decay of ^{136}Xe, has set an upper bound of $m_{ee} < 61 - 165\,\text{meV}$ [3]. In addition to determining the Dirac or Majorana nature of neutrinos, constraining m_{ee} mass would yield a bound on the absolute neutrino mass scale, according to the previous relations.

Chapter 2

The DUNE experiment

The Deep Underground Neutrino Experiment (DUNE) will be installed in the Long Baseline Neutrino Facility (LBNF) under construction in the United States. It will consist of a Near Detector at a distance of 547 m from the neutrino source at Fermilab in Illinos and a Far Detector located at the Sanford Underground Research Facility (SURF) in South Dakota, for a baseline of 1300 km.

The far detector, located at a depth of about 1.5 km, will consist of four modular liquid argon time-projection chambers (LArTPC) with a mass of 17 kt each. The LArTPC technology will allow the reconstruction of neutrino interactions with image-like precision [31].

2.1 DUNE physics objectives

The primary science goals of DUNE are:

- To perform a comprehensive program of neutrino oscillation measurements using the ν_μ and $\bar{\nu}_\mu$ beams from Fermilab's Long-Baseline Neutrino Facility (LBNF). The program includes the measurement of the CP violating phase of the lepton sector, δ_{CP}, the determination of the neutrino mass ordering, the measurement of the θ_{23} mixing angle and its octant, as well as sensitive tests of the three-neutrino mixing framework. Of paramount importance in this program is the search for CP violation in neutrino oscillations, as it might potentially offer insight into the origin mechanisms of the matter-antimatter asymmetry.

- The search for proton decay. The observation of such a process would represent a ground breaking discovery in physics, as it would satisfy a key requirement of Grand Unified Theories (GUT).

- The detection and measurement of the ν_e flux from a core-collapse supernova within our galaxy, should one such event occur during DUNE's lifetime. The detection of

supernova neutrinos in an up-to-date experiment would provide unique information on the early stages of the core-collapse event and could signal the birth of a black hole.

The innovative characteristics of the LBNF beam and DUNE detectors will also allow to perform a rich ancillary science program beyond the primary goals of the experiment, including:

- Measurements of accelerator-neutrino flavour transitions with sensitivity to beyond the standard model (BSM) physics such as non-standard interactions (NSIs) Lorentz and CPT invariance violation, sterile neutrinos, large extra dimensions and heavy neutral leptons. Tau neutrino appearance tests could also be conducted.

- Measurement of neutrino oscillation phenomena through atmospheric neutrinos.

- Searches for dark matter exploiting a variety of signatures in both the near and far detectors, as well as non-accelerator BSM physics searches such as that for neutron-antineutron oscillations.

- A varied neutrino interaction physics program with the near detector, including a wide range of measurements of neutrino cross sections and studies of nuclear effects.

Further advancements in LArTPC technology over the course of the far detector development and construction may enhance DUNE's sensitivity to very low-energy phenomena such as solar neutrinos or the supernova diffused neutrino flux [31].

2.1.1 Sensitivities of oscillation searches

In the following the oscillation parameters that will be object of study at DUNE, the techniques employed for the measurements and the expected timeline of discoveries will be presented.

The oscillation channels that DUNE will be able to observe are $\overset{(-)}{\nu}_\mu \to \overset{(-)}{\nu}_e$, whose probability $P_{\overset{(-)}{\nu}_\mu \to \overset{(-)}{\nu}_e}$, through matter in a constant density approximation, is given by eqn. (1.2.30): both δ_{CP} phase and the effective matter potential introduce an asymmetry between the $\nu_\mu \to \nu_e$ and $\bar\nu_\mu \to \bar\nu_e$ channels.

In the few-GeV range the $\nu/\bar\nu$ asymmetry due to the matter effect increases with the baseline, so that an experiment with a longer baseline will be more sensitive to the mass ordering. The 1300 km baseline is thus one of DUNE's key strengths as it allows a high sensitivity to the matter effect: the asymmetry in the neutrino/antineutrino oscillation probabilities, the sign of which depends on the mass ordering, amounts to approximately $\pm 40\%$ in the peak flux region, larger than the maximal CP violation

asymmetry associated to δ_{CP}. Thus, DUNE will be capable of removing the degeneracy between the matter and CP violation asymmetries and determine the mass ordering and δ_{CP} unambiguously and with a high confidence. Fig. 2.1 shows the $\overset{(-)}{\nu}_e$ appearance probability at a baseline of 1300 km as a function of the neutrino/antineutrino energy and for several values of δ_{CP}, this last quantity affecting both the amplitude and phase of the oscillation. The difference in probability for different values of δ_{CP} is larger at the higher oscillation nodes, for $E < 1.5$ GeV. A broadband experiment such as DUNE, capable of mapping out the spectrum of observed oscillations down to at least 500 MeV, is therefore optimal for the study of δ_{CP}.
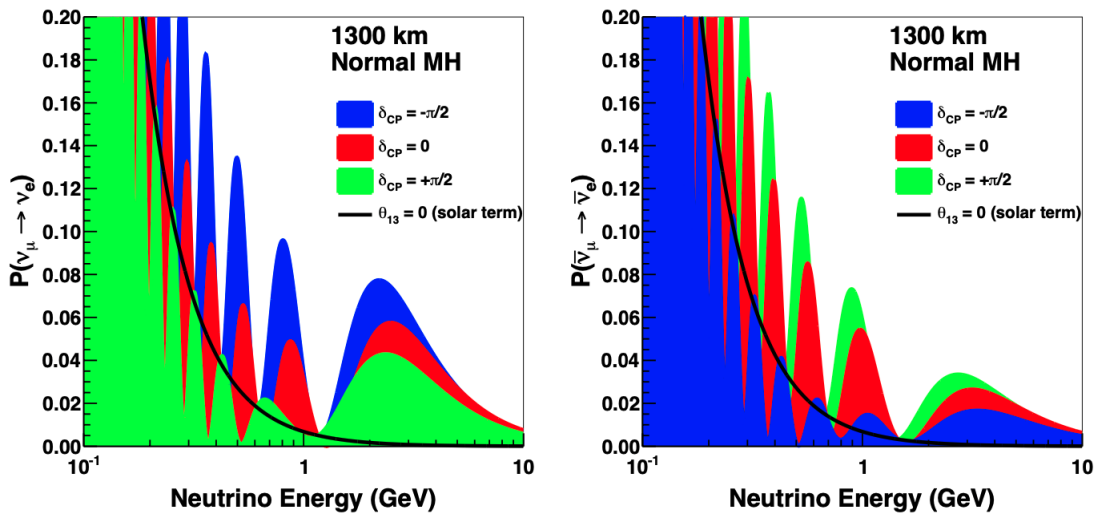
Fig. 2.1: Appearance probability at the DUNE baseline of 1300 km, as a function of neutrino energy, for $\delta_{CP} = -\pi/2$ (blue), 0 (red) and $\pi/2$ (green), for neutrinos (left) and antineutrinos (right). The $\theta_{13} = 0$ case is plotted as the black line. Normal ordering is assumed [31].

The observation of the oscillation structure will enable DUNE to perform precision measurements of all the individual mixing parameters with improved sensitivity. While reactor experiments have yielded the most accurate measurements of θ_{13} to date, DUNE will eventually be able to reach a comparable precision in its independent measurement of the mixing angle through the ν_e and $\bar{\nu}_e$ appearance channels. Such data will provide an independent constraint on the PMNS mixing matrix [31].

The simulated data samples for the far and near detectors have been taken as inputs to fits for the CP violation sensitivity, mass ordering sensitivity and parameter measurement resolutions. The resulting projections for seven, ten and fifteen years of exposure are presented in this section, assuming the following staging plan for the experiment [31]:

- Start of beam run: two far detector (FD) module volumes for a total target mass of 34 kt, 1.2 MW neutrino beam.

- After one year: one FD module added, for a total target mass of 51 kt.

- After three years: one FD module added, for a total fiducial mass of 40 kt.

- After six years: upgrade to a 2.4 kt neutrino beam.

Equal running time for neutrino and antineutrino beams is assumed.

CP **violation sensitivity** Fig. 2.2a shows the significance of CP violation ($\delta_{CP} \neq 0, \pi$) observation as a function of the true δ_{CP} value for exposures corresponding to seven and ten years of data. The double peak structure is produced by the CP violation significance necessarily dropping to zero at the CP conserving values of $\delta_{CP} = -\pi, 0, \pi$. The variation in the true value of $\sin^2 2\theta_{23}$ is responsible for a significant portion of the variation in the fit projections, shown as the bands indicating 68% of the fits.

The significance that can be reached for CP violation for 75% and 50% of the δ_{CP} values and for $\delta_{CP} = -\pi/2$ is shown in Fig. (2.2b) as a function of the exposure in years: CP violation can be observed with 5σ significance after 7 years for $\delta_{CP} = -\pi/2$ and after about 10 years for 50% of the δ_{CP} values. Around thirteen years of runtime allow to reach a 3σ significance for 75% of the δ_{CP} values [31].

Mass ordering sensitivity The significance for the determination of the mass ordering as a function of the true value of δ_{CP} is shown in Fig. (2.3a), with the same exposures and staging plan assumptions described above. The characteristic shape of the diagram is due to the near degeneracy between matter and CP violating effects that occurs close to $\delta_{CP} = \pi/2$ for normal ordering.

The significance, as a function of exposure in years, that can be determined for 100% of δ_{CP} values and when $\delta_{CP} = -\pi/2$, is shown in Fig. 2.3b. DUNE will be able to establish the neutrino mass ordering at a 5σ level for 100% of δ_{CP} values after between two and three years, so the plot only extends to seven years of exposure, corresponding to 500 kt·MW·years [31].

Oscillation parameters measurements In addition to the discovery potential for mass ordering and leptonic CP violation, DUNE is set to improve the precision on the key parameters governing neutrino oscillations, including δ_{CP}, $\sin^2 2\theta_{13}$, $\sin^2 \theta_{23}$ and its octant as well as Δm_{31}^2. The resolution, in degrees, of DUNE's measurement of δ_{CP} is shown in Fig. 2.4a as a function of the true value of δ_{CP}: it is significantly better for near CP conserving values of the CP phase compared to maximally CP violating ones. Resolutions between 5° and 15° are possible for fifteen years of exposure depending on the true value of δ_{CP}. Figs. 2.5a to 2.5d show the resolution of DUNE's measurements of δ_{CP}, $\sin^2 2\theta_{13}$, $\sin^2 2\theta_{23}$ and Δm_{32}^2 respectively, as a function of exposure in kt·MW·years. The DUNE measurement of $\sin^2 2\theta_{13}$ will approach the precision of reactor experiments
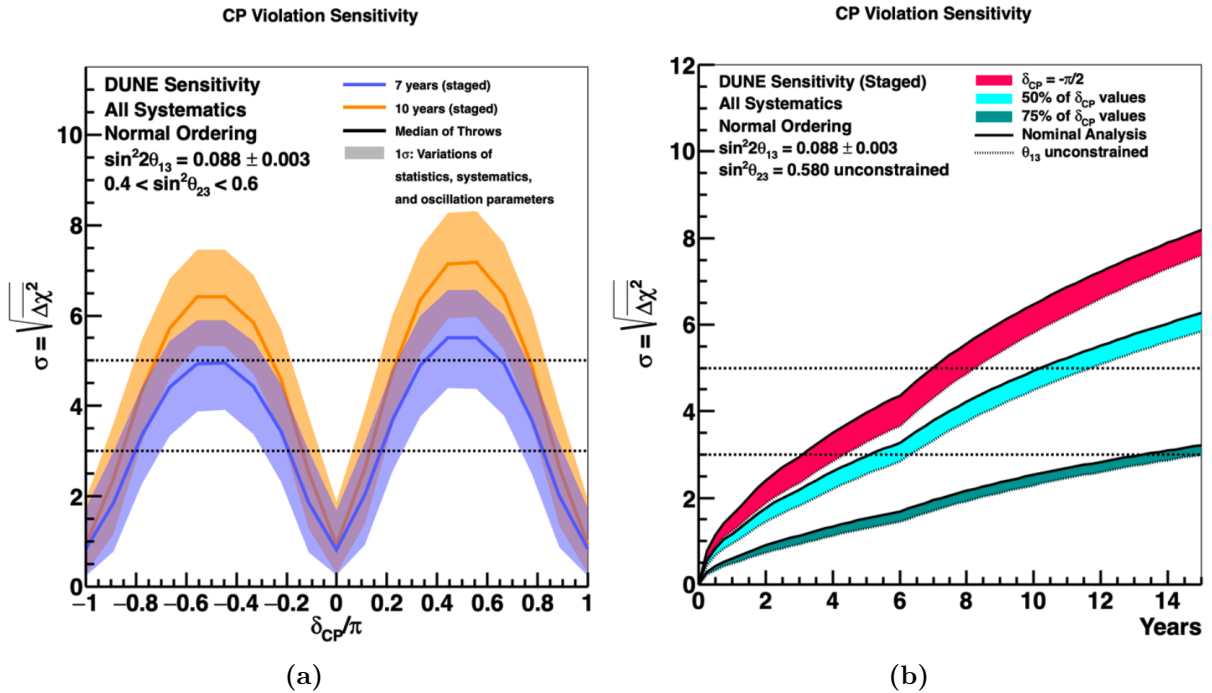
Fig. 2.2: (a) Significance of the DUNE determination of CP violation as a function of the true δ_{CP} value for seven (blue) and ten (orange) years of exposure. The width of the bands covers 68% of fits in which random throws are used to simulate statistical variations and select the true values of oscillation and systematics parameters. The median sensitivities are represented by the solid lines. Normal ordering is assumed. (b) Significance of DUNE's determination of CP violation for $\delta_{CP} = -\pi/2$ and for 50% and 75% of possible δ_{CP} values, as a function of time in calendar years. Normal ordering is assumed. Changes in trajectory correspond to the upgrades in the staging plan. The widths of the bands are due to the application of an external constraint on $\sin^2 2\theta_{23}$ [31].

for high exposures, allowing an independent comparison between the two values, which would be useful as a test of the unitarity of the PMNS.

A combination of the ν_μ disappearance and ν_e appearance channels allows, as shown in Section 1.2.1.5, to probe the octant of θ_{23}. Fig. 2.4b shows the sensitivity to the determination of the octant as a function of the true value of $\sin^2 \theta_{23}$: such sensitivity is significant for values of $\sin^2 \theta_{23}$ less than about 0.47 and larger than about 0.55 [31].

2.1.2 Low-energy and supernova neutrinos

The DUNE experiment will be sensitive to neutrinos with energies between ~ 5 MeV to a few tens of MeV. This energy regime is of particular interest for the observation of the neutrino burst produced in galactic core-collapse supernovae and other astrophysical

sources, like the Sun and the Diffuse Supernova Neutrino background.

Study of supernova neutrino bursts   The particular sensitivity to the ν_e component of the supernova neutrino burst at DUNE should be due to the dominant reaction $\nu_e + {}^{40}\text{Ar} \rightarrow e^- + {}^{40}\text{K}^*$, with e^- and the de-excitation products of ${}^{40}\text{K}^*$ being the observables. Other possibly significant transitions are under investigation.

In the event of a supernova in our galaxy, the predicted number of signal events at the DUNE FD is of ~ 3000, with preliminary simulation studies showing that cosmogenic and radiological backgrounds will have minor effects on the reconstruction of a triggered neutrino burst [31].

(a)   (b)
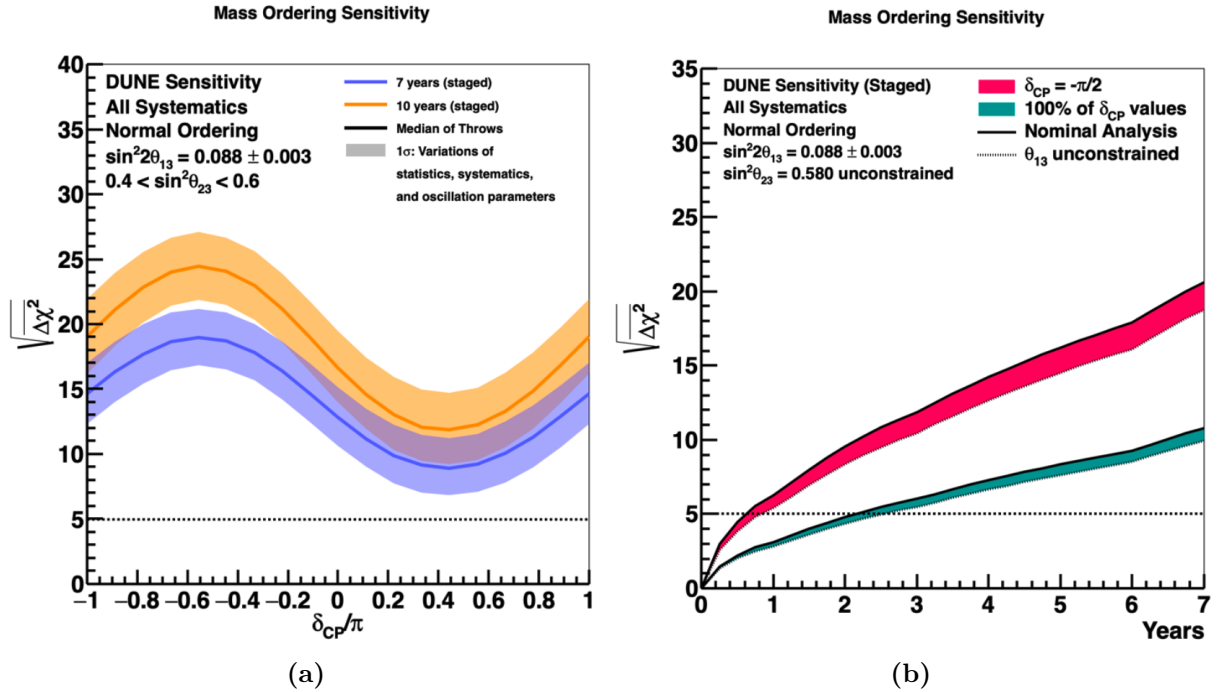
Fig. 2.3: (a) Significance of the DUNE determination of the neutrino mass ordering as a function of the true δ_{CP} value for seven (blue) and ten (orange) years of exposure. The width of the bands covers 68% of fits in which random throws are used to simulate statistical variations and select the true values of oscillation and systematics parameters. The median sensitivities are represented by the solid lines. Normal ordering is assumed. (b) Significance of DUNE's determination of the neutrino mass ordering for $\delta_{CP} = -\pi/2$ and for 100% of possible δ_{CP} values, as a function of time in calendar years. Normal ordering is assumed. Changes in trajectory correspond to the upgrades in the staging plan. The widths of the bands are due to the application of an external constraint on $\sin^2 2\theta_{23}$ [31].
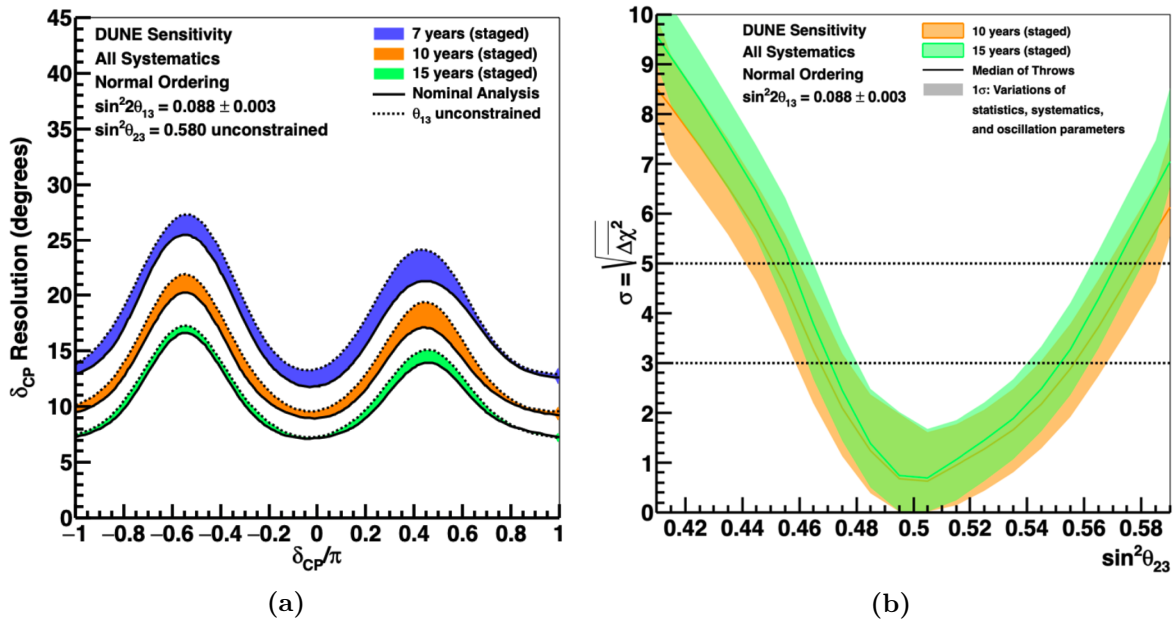
Fig. 2.4: (a) Resolution in degrees for DUNE's measurement of δ_{CP} as a function of the true value for seven (blue), ten (orange) and fifteen (green) years of exposure. Normal ordering is assumed. The width of the bands shows the impact of external constraints on $\sin^2 2\theta_{13}$.
(b) Sensitivity to the determination of the θ_{23} octant, as a function of the true $\sin^2 \theta_{23}$ value, for ten (orange) and fifteen (green) years of exposure. Normal ordering is assumed. The width of the bands covers 68% of fits with statistical variations and true parameter values selected by random throws. The solid lines show the median sensitivities [31].

Study of solar neutrinos The detection of solar and other astrophysical low-energy neutrinos is challenging in a LArTPC because of the relatively high energy threshold for detection of charged current interactions in argon (> 5 MeV). However, DUNE's LArTPC offer a large cross section and unique channel-tagging signatures from deexcitation photons. The solar neutrino event rate for a final Far Detector fiducial mass of 40 kt is of ~ 100 per day. A high-statistics solar neutrino sample could plausibly be selected with sophisticated event selection and possibly additional shielding [31].

Study of the Diffuse Supernova Neutrino Background. The Diffuse Supernova Neutrino Background (DSNB) is the yet unobserved background of relic neutrinos produced by supernovae all over the universe, with energies in the few-to-30 MeV range. Its observation would provide valuable information on the supernova neutrino emission and the overall core-collapse process rate. DUNE's far detector would complement, with its sensitivity to the ν_e component of the DSNB, the observations of Cherenkov and scintillator detectors, which are sensitive to the antineutrino component.

The DSNB detection will be limited down to 18.8 MeV of the neutrino from the solar
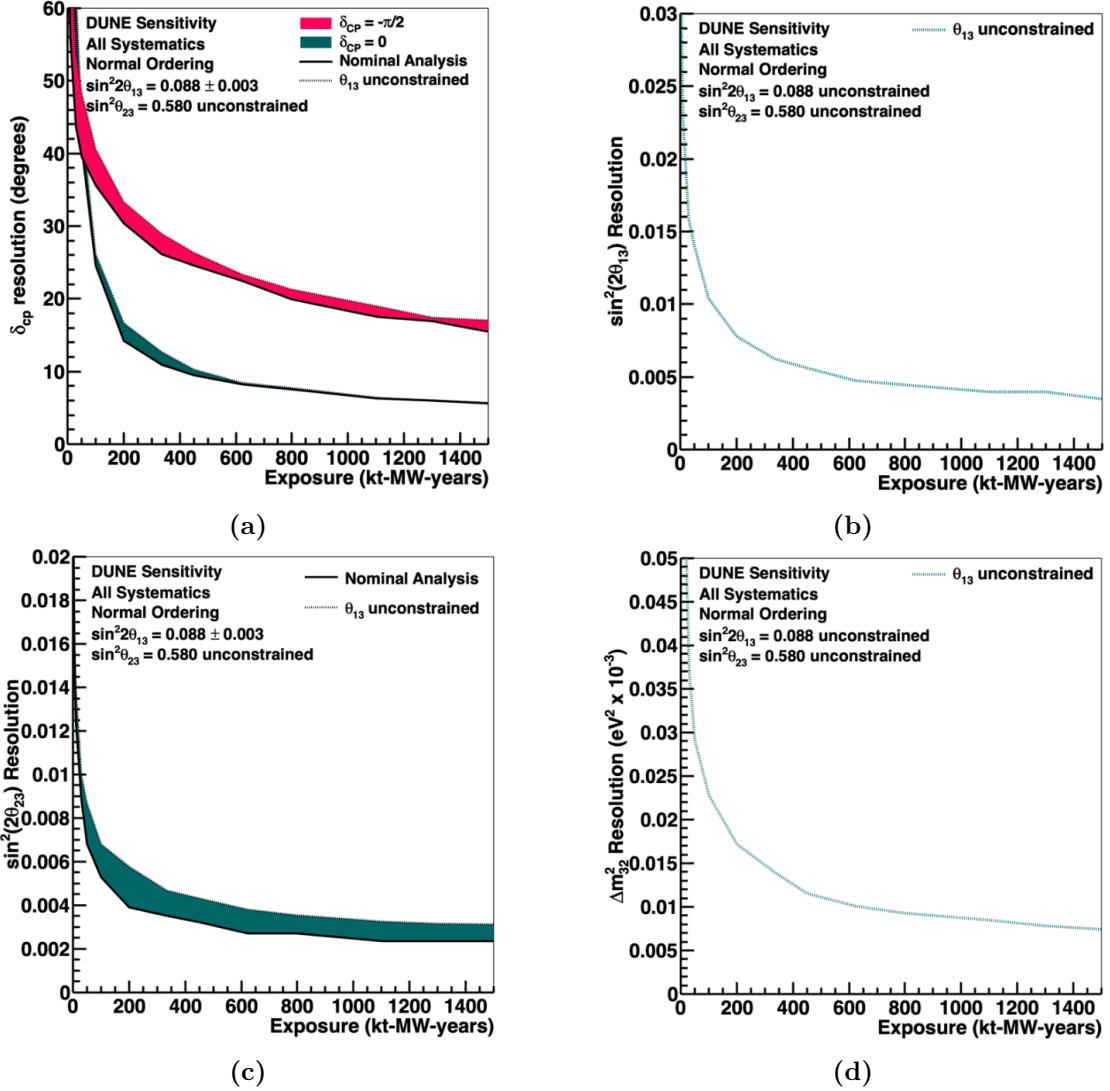
Fig. 2.5: (a) Resolution of DUNE's measurement of δ_{CP} as a function of the exposure in kt·MW·years. The resolution depends significantly on the true value of the phase, so curves for $\delta_{CP} = -\pi/2$ (red) and $\delta_{CP} = 0$ (green) are shown. The width of the bands is due to the external constraint on $\sin^2 2\theta_{13}$. (b) Resolution of DUNE's measurement of $\sin^2 2\theta_{13}$ as a function of the exposure in kt·MW·years. As external constraints are irrelevant, only the unconstrained curve is shown. (c) Resolution of DUNE's measurement of $\sin^2 2\theta_{23}$ as a function of the exposure in kt·MW·years. The width of the bands is due to the external constraint on $\sin^2 2\theta_{13}$. (d) Resolution of DUNE's measurement of Δm_{32}^2 as a function of the exposure in kt·MW·years. As external constraints are irrelevant, only the unconstrained curve is shown [31].

hep reaction and up to 40 MeV by the atmospheric ν_e flux, with event rates expected to be of $1-2$ per MeV per 20 years in 10 kt in the $19-31$ MeV window: such a low signal rate would make even rare radiological and cosmogenic backgrounds challenging [31].

2.1.3 BSM physics

The combination of the high intensity LBNF neutrino beam with DUNE's near detector and massive LArTPC far detector modules at a baseline of 1300 km will enable a variety of probes of beyond the standard model (BSM) physics.

Search for active-sterile neutrino mixing. Experimental results in tension with the three-neutrino framework which may be interpreted as mixing between the known active neutrinos and one or more right-handed-only sterile states have led to a diverse program of searches. DUNE is sensitive over a wide range of potential sterile neutrino mass splittings by searching for unexpected disappearances of charged and neutral current interactions over the long baseline between near and far detector or over the short baseline to the near detector. DUNE is set to improve significantly on the sensitivities of previous probes.

Searches for non-unitarities in the PMNS matrix. A characteristic of most of the proposed mechanisms for neutrino mass generation is the presence of heavy neutrino states in addition to the three light states of the standard model. This would imply a deviation from unitarity of the PMNS matrix which, if of order 10^{-2}, would decrease the event rate at DUNE, and thus its reach to the standard parameters.

Searches for nonstandard interactions (NSI). Data collected by DUNE could be significantly affected by NSI occurring during neutrino propagation through the Earth, provided that the new physics parameters are large enough. DUNE will be sensitive to such probes as it can leverage a very long baseline and a wide-band beam.

Searches for Lorentz or CPT symmetries violation. The present constraints on the CPT and Lorentz symmetries, whose potential violation would have major consequences on the standard model, can be improved by DUNE by several orders of magnitude, providing an important test of these assumptions of standard fundamental physics.

Searches for neutrino trident production. DUNE will be able to test the possibility that neutrinos may be charged under additional BSM symmetries and interact with the new gauges bosons with unprecedented precision. The near detector will measure extremely rare *neutrino trident interactions*, which are neutrino-induced dilepton

production in the Coulomb field of a heavy nucleus, searching for deviations from the standard model rate of 100 per year.

Search for light dark matter (LDM). The parameter space of hypothetical light dark matter particles, with masses below the electroweak scale, and of the mediator that allows interactions with ordinary matter, can be covered by high-flux neutrino beam experiments like DUNE in a complementary way to direct detection or collider experiments. The LDM particles can be detected in the near detector through neutral-current-like interactions with electrons or nucleons and the neutrino induced backgrounds can be suppressed with timing and event kinematics.

Search for boosted dark matter (BDM). The large DUNE far detector will be able to search for BDM, a dark matter model in which a relativistic light DM particle is produced by the annihilation of a heavier one in astrophysical sources. The incoming energy of the light DM components could be above the DUNE energy threshold over a wide range of parameter space.

2.2 DUNE design

The remainder of this chapter will outline the features, design choices and science goals of the components of the DUNE experiment: the Long Baseline Neutrino Facility (LBNF) beam, the far detector (FD) and near detector (ND), a qualitative schematic of which is shown in Fig. 2.6.
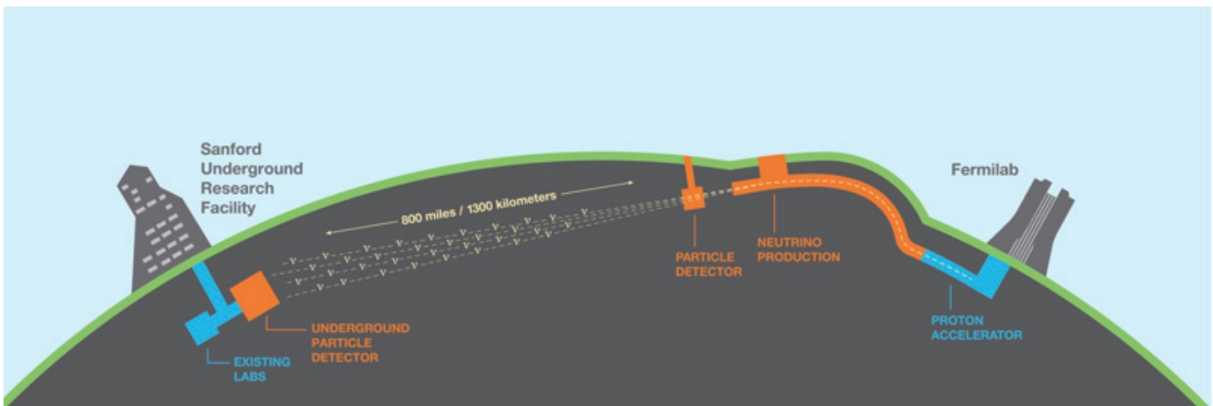
Fig. 2.6: Schematic of the LBNF/DUNE facilities at Fermilab and SURF. The existing facilities are shown in blue, while the planned ones are in orange. The neutrino beam baseline of 1300 km is indicated [31].

2.2.1 The LBNF neutrino beam

The LBNF beamline at Fermilab will provide a neutrino beam of with appropriate intensity and energy range to meet the requirements of the long baseline neutrino physics conducted at DUNE. The wide-band neutrino beam will be aimed the SURF detectors 1.5 km underground at a distance of 1300 km from the production point.

The primary proton beam will be provided by the PIP-II upgrade of the Main Injector accelerator at Fermilab, which will deliver between 1.0 and 1.2 MW of proton beam in the 60 to 120 GeV energy range at the start of DUNE operations. PIP-II will also provide a platform for extending the beam power to DUNE to > 2 MW and a further update of the accelerator complex will allow up to 2.4 MW of beam power by 2030.

The proton beam will be extracted at the new MI-10 installation and, passing through the transport section, it will be bent in order to establish the final trajectory towards the far detector. The proton beam will hit a solid target and produce, among others, charged mesons that are focused by magnetic horns into a 194 m decay pipe, travelling along which they decay producing the neutrino beam. The neutrino beam characteristics are defined by the meson focusing system, which is optimized to provide a wide-band beam in an energy of 0.5 to 5 GeV. Such an energy range will allow the coverage of the first and second neutrino oscillation maxima which, for $L \simeq 1300$ km, are approximately at 2.4 and 0.8 GeV. The polarity of the focusing horns allows to select either positive or negative mesons, which yield neutrino and antineutrino beams respectively.

The goal for the proton beam is to accumulate 1.1×10^{21} protons on target per year, with the resulting neutrino and antineutrino fluxes at the FD, in the absence of oscillation, shown in Fig. 2.7. Focusing positive and negative particles respectively allows to produce a beam composed mainly of ν_μ or $\bar{\nu}_\mu$, with a small contamination of ν_e and $\bar{\nu}_e$ [47].

2.2.2 The DUNE Far Detector modules

The DUNE far detector, located 1.5 km underground at SURF, will consist, by the end of the staging plan, of four LArTPC detector modules, each contained in a cryostat holding 17.5 kt of LAr. The LArTPC technology will provide good tracking and calorimetry performances, and the use of four identically sized modules will allow flexibility for staging construction and for potential evolution of the LArTPC technology [31].

The LArTPC technology that has been selected for the FD is the Single-phase (SP) LArTPC: in this design charges drift in LAr and are read out on wire planes. As no signal amplification occurs in the liquid, the SP design requires very low-noise electronics for a good signal-to-noise ratio to be achieved. Two designs of SP-TPC are being considered: a *horizontal drift* TPC, where the charges drift horizontally towards an anode plane, and a *vertical drift* TPC, where the drift direction is vertical towards the anode planes on the top and bottom. The DUNE collaboration has constructed the ProtoDUNE-SP
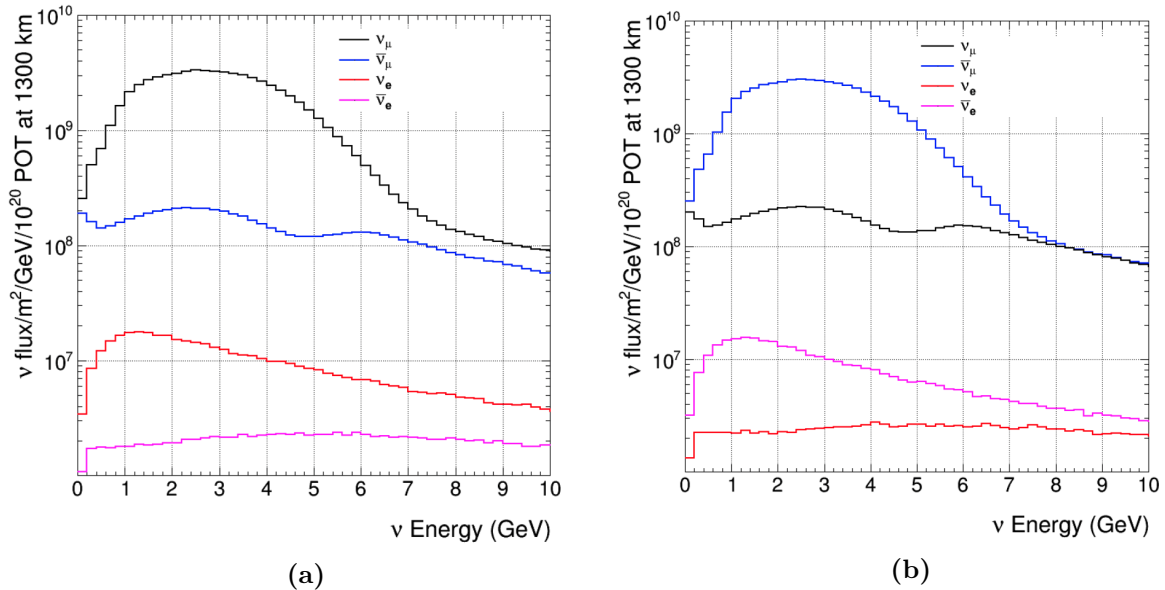
Fig. 2.7: (a) Neutrino fluxes at the far detector as a function of energy in the absence of oscillations, with horns focusing positive particles. The minor components are shown in addition to the dominant ν_μ flux. (b) Antineutrino fluxes at the far detector as a function of energy in the absence of oscillations, with horns focusing negative particles. The minor components are shown in addition to the dominant $\bar{\nu}_\mu$ flux [47].

prototype detector at CERN to test the technology of the *horizontal drift* TPC. This has approximately 1/20 the size of a full-scale FD module and uses the same components as the final detector. The large scale prototype has allowed to validate key aspects of the TPC design, engineering procedures and collect valuable calibration data from a hadron test beam. The ProtoDUNE-SP has started collecting data in fall 2018 and a new run is planned to start by the end of 2022 [31].

Results obtained with the ProtoDUNE-SP detector have already provided valuable information on the design, calibration and simulation of the FD modules. At the time of writing of this dissertation, the plan is to utilize the SP horizontal and vertical drift design for the first and second module respectively. The technology that will be implemented in the third and fourth modules is still to be decided. The main features of DUNE's two LArTPC detector designs are outlined in the following.

2.2.2.1 Horizontal drift LArTPC

In the horizontal drift LAr TPC design, particles passing through the detector ionize the argon atoms and the ionization electrons drift in the intense electric field to the Anode Assembly Plane (APA) with a timescale of milliseconds. The APA consists of layers of active wires forming a grid, with the relative voltage between the layers chosen so that

the drifting electrons will only produce bipolar induction signals on all but the last layer, where they are instead absorbed, inducing a monopolar signal.

Liquid Argon is an excellent scintillator which emits Vacuum Ultra-Violet light (VUV) with a 1.27 nm wavelength. The prompt scintillation light, which crosses the detector with a ns timescale, is collected by photon detectors after being shifted into the visible range: this provides a starting time t_0 for the ionization. The event topology along the drift direction is thus reconstructed from the timing of the ionization electrons reaching the anode. The coordinates along directions perpendicular to that of drift is given by the pattern of currents on the grid of anode wires. Fig. 2.8 shows the general operating principle of a LArTPC [48].
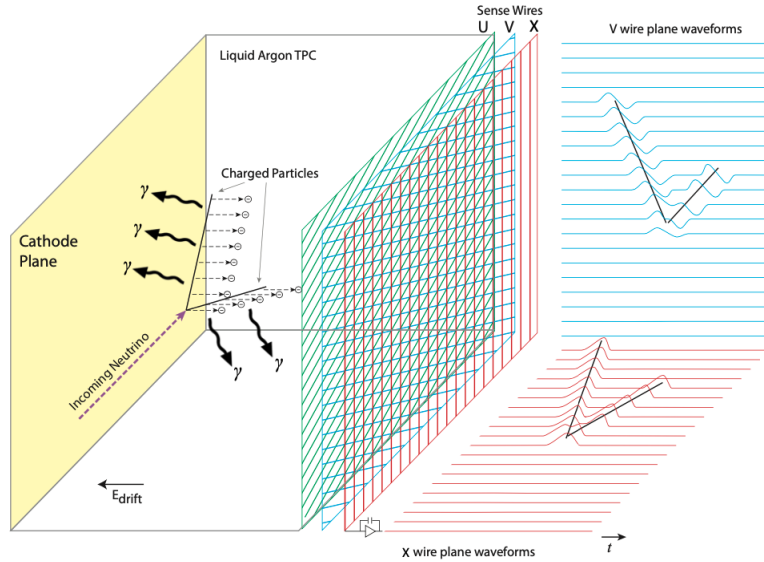
Fig. 2.8: General operating principle of a single-phase LArTPC [48].

The DUNE single-phase LArTPC will have each a total mass of 17.5 kt. Each TPC module will be housed inside a cryostat of 65.8 m ×17.8 m ×18.9 m outer dimensions, creating four 3.5 m drift volumes between five alternating anode and cathode walls, each with dimensions 58 m ×12 m. Fig. 2.9 shows the internal structure of a SP module.

Each cathode wall is formed by and array of 150 Cathode Plane Assemblies, 1.2 m ×4 m panels held at −180 kV. With the anode walls being kept close to ground, a uniform 500 V/m electric drift field is produced across the drift volume. The remaining open sides of the TPC are surrounded by a Field Cage which ensures a field uniformity better than 1% throughout the active volume.

Anode walls are each composed of 50 Anode Plane Assemblies (APA) units of 6 m ×2.3 m dimensions. Each anode wall is two (APA) high and 25 (APA) wide. The APAs, the scheme of which is shown in Fig. 2.10, are two-sided, with three active wire layers
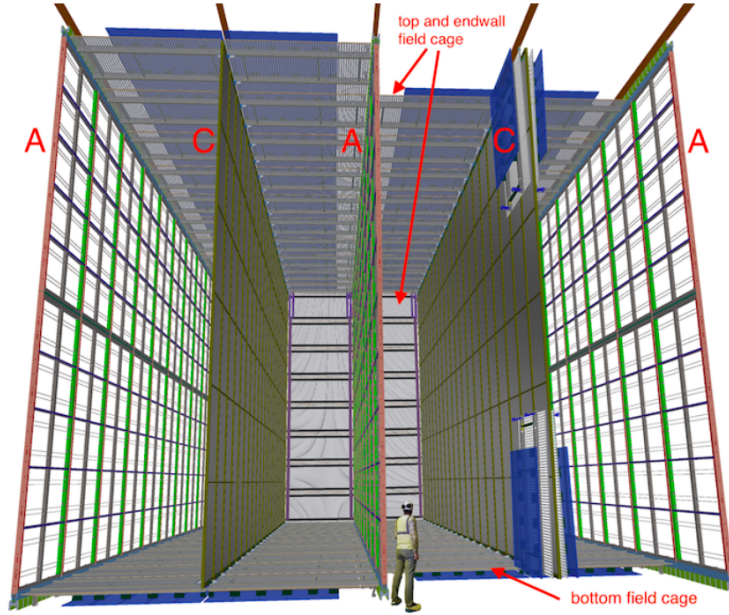
Fig. 2.9: A 10 kt DUNE far detector SP module, showing the alternating anode (A) and cathode (C) planes, as well as the surrounding Field Cage surrounding the field regions. The field cage on the right is shown in its undeployed state [48].

and an additional shielding layer wrapped around them. The spacing of the wires is of ~ 5 mm.

The readout cold electronics (CE) are attached to the top end of the top APA and to the bottom end of the bottom APA. The low LAr temperature benefits these front-end electronics trough the reduction of the thermal noise. The signals from the collection and induction wires are shaped, amplified and digitized by the front-end electronics thanks to a series of three different ASIC types.

Charged particles passing through the liquid argon will produce, in addition to ionization, scintillation light, with approximately 24×10^3 photons per MeV. The scintillation photons are collected by devices called X-Arapucas, bars running the 2.3 m width of the APA in between the two sets of wire layers. Ten X-Arapucas are mounted on each of the APAs. Each X-Arapuca bar consists of four Arapuca cells with dichroic filters transparent to VUV light, alternated with wavelength-shifter (WLS) plates, which convert the UV photons into the visible spectrum at 430 nm. The visible photons emitted inside the WLS plates with an inclination with respect to the surface grater than the critical angle reach the SiPMs at the edges of the plates. The visible photons that, conversely, escape the WLS are reflected by the dichroic filters back into the wavelength-shifter plates, as the former have an optical cutoff for wavelengths > 400 nm. The working principle of the X-Arapuca cells is illustrated in Fig. 2.11, while scheme of the X-Arapuca modules

and their placement inside APAs is shown in Fig. 2.12.

The primary requirement for the LAr used in the TPCs is its purity, as electronegative contaminants can absorb ionization electrons and nitrogen contaminants quench scintillation photons. The target purity from electronegative contaminants in argon is below 100 ppt O_2 equivalent, enough to ensure an ionization-electron lifetime > 3 ms at the nominal drift voltage. This ensures the SNRs which are necessary to perform pattern recognition and track separation. Detector components are also required to release < 30 ppt of electronegative impurities in the LAr. ProtoDUNE data has confirmed the possibility of exceeding the target purity, reaching lifetimes in excess of 6 ms. Nitrogen contaminants must be kept below 25 ppm to achieve the required minimum of 0.5 photoelectrons per MeV detected for events in all parts of the detector. LAr purity is maintained by constantly cycling the argon through the purification system [48].
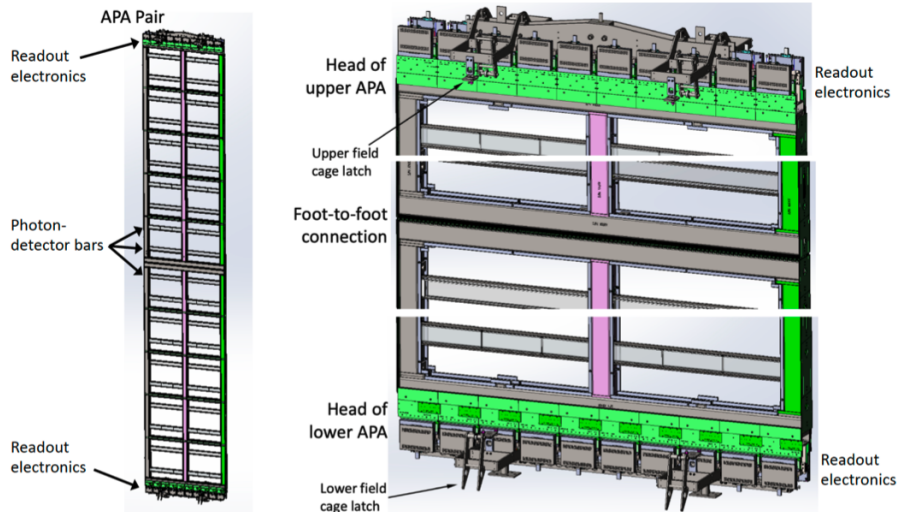
Fig. 2.10: Left: two APAs linked together to form one unit of an APA wall. Photon detection X-Arapuca modules are installed across the width of the APAs.
Right: a closer look at the top and bottom of the APA stack, showing the readout electronics and at the center, where the APAs are connected [48].
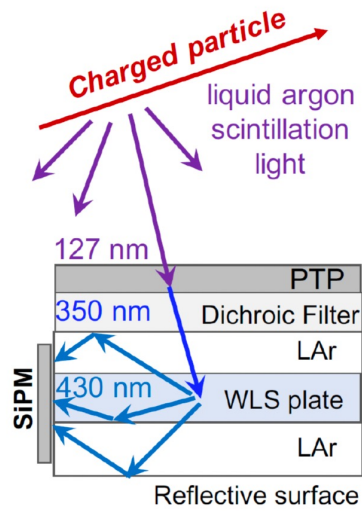
Fig. 2.11: Working principle of an X-Arapuca cell: the VUV LAr scintillation light is shifted into the visible spectrum upon entering the module. The escaping visible photons are reflected back towards the SiPM by the dichroic filters.
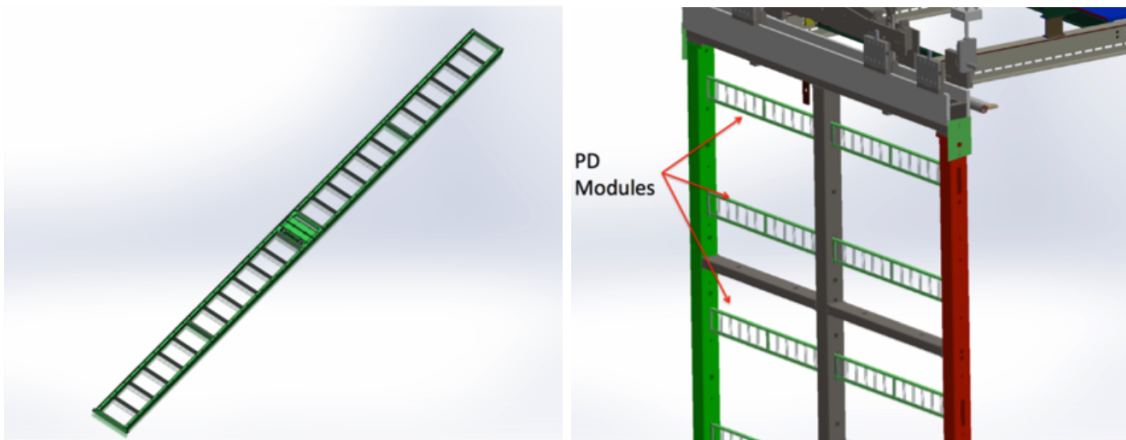
Fig. 2.12: Left: an X-Arapuca photon detection module, showing the 24 X-Arapuca cells. The 48 SiPMs that detect the light from the cells are long the long edges of the module. Right: X-Arapuca modules mounted inside an APA [48].

2.2.2.2 Vertical Drift LArTPC

For the second module of the DUNE Far Detector, a Vertical Drift LArTPC has been recently proposed, thanks to the experience gained by the run of ProtoDUNE at CERN. In this design, the cathode plane hangs at mid height in the module with a -300 kV

voltage, for a drift length of 6.5 m towards the anodes on the top and bottom. The field cage ensures the uniformity of the electric field at 500 V/cm.

For the TPC anodes, perforated Printed Circuit Boards have been chosen, as they can be hung horizontally without suffering significant deformations. Each section of the anode plane will consist of two PCB boards, with the electron drifting trough the amplified electric field in the induction PCB towards the collection board. The design specifications are being optimized at the time of writing. The anodes are mounted within Charge Readout Plane structures in the top and bottom of the module.

In the vertical drift design the Photon Detection System modules, using the same X-Arapuca detectors as the horizontal drift version, can be placed on the walls of the cryostat behind the field cage, designed to be semi-transparent, and on the cathode surface. The latter position has most importantly required the development of novel optoelectronic systems for signal and power transmission: a Power-over-Fiber solution for the power distribution and an analog optical transmitter that allows the digitization of the SiPM signals in warm.

The VD-TPC concept is currently undergoing an intense R&D campaign of test and validate its different systems. Tests on a small scale prototype cryostat at CERN have started in fall 2021 [49].

2.2.3 The DUNE Near Detector complex

The near detector (ND) is located approximately 547 m from the source of the LBNF neutrino beam and includes three primary detector components: ND-LAr and ND-GAr, which can move off-axis and SAND, with a fixed on axis position. The three detectors are shown in the ND hall in Fig. 2.13. The ND will serve key roles in the oscillation program [50]:

- It will allow a high-statistics characterization of the beam close to the source, providing its initial state which is compared to the FD observations to extract oscillation parameters. The use of LArTPC detectors that are functionally similar to the FD helps in reducing the systematics.

- It will include a spectral beam monitor that can detect changes in the beam in a timely fashion.

- The high statistics collected in the ND, together with its particle ID capabilities, will make the ND instrumental for tuning the neutrino interaction models used to move between the beam model and the experimental data, thus allowing a reduction of the systematic errors.

- The ND components will take data at different off-axis positions, providing data sets with different beam spectra. This allows to deconvolve the beam and cross-section models and constrain each separately. Additionally, the creation of ND

data sets similar to the oscillated FD ones will make it possible to minimize the errors arising from near-to-far flux interference.

In the following, the features and objectives of each of the three detectors are outlined.
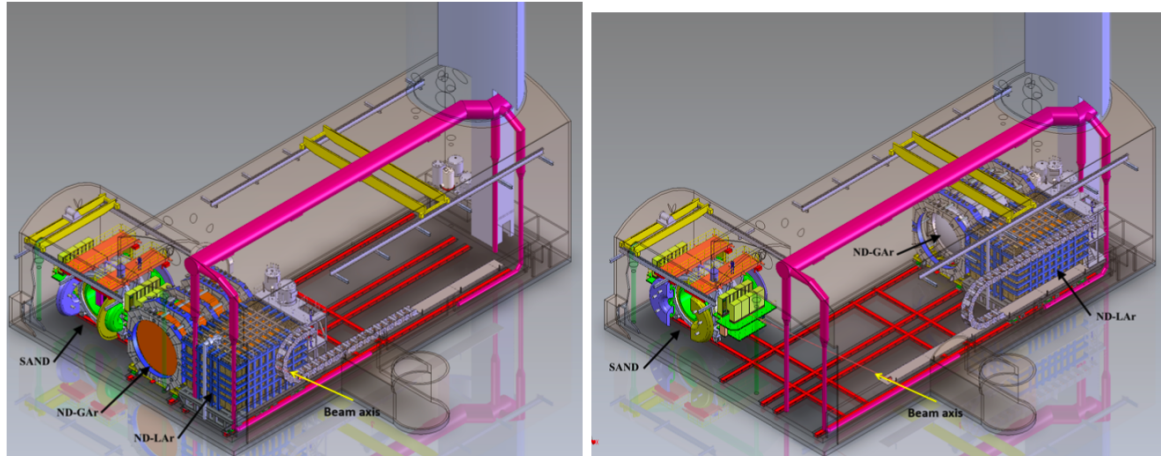
Fig. 2.13: Schematic of the DUNE ND hall with all components in the on-axis configuration (left) and with ND-LAr and ND-GAr in an off-axis configuration (right). The SAND detector is along the beam axis, indicated by the yellow arrow [50].

2.2.3.1   ND-LAr

The ND-LAr detector will be a LArTPC similar to those used at the far site. At the near site, the LArTPC will be exposed to a much more intense neutrino flux, leading to event pile-up. To overcome this limitation, ND-LAr will be based on the ArgonCube technology, consisting of a large TPC fabricated out of a matrix of smaller, optically isolated TPCs read out individually by a pixelized readout. Each of the TPCs will be equipped with optical readout providing the timing necessary to associate tracks and events across the matrix. The current design features a 5×7 matrix of modules. The subdivision of the volume will allow for smaller drift distances and times, which, together with the optical insulation will reduce the issues with overlapping interactions. The smaller volumes will also reduce the requirements on high voltage and argon purity.

The pixelization of the readout will enable the full 3D reconstruction of tracks and enhance the robustness in a high-multiplicity environment. New dielectric light detection systems, which can be placed inside the field cage, will improve the localization of light signals. The tracking and energy resolution will enable the measurement of the beam flux using several techniques, including the rare νe^- scattering process.

The ArgonCube TPCs configuration of ND-LAr will be large enough to provide the required hadronic shower containment and statistics (1×10^8 ν_μ events per year), with

a fiducial mass of 67 t in a 5 (along beam) ×7 (transverse to beam) ×3 (height) m³ volume. In Fig. 2.14, an illustration of ND-LAr shows the array of ArgonCube TPCs.
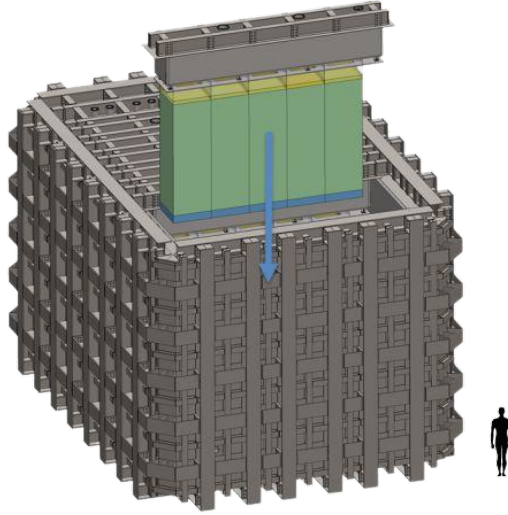
Fig. 2.14: Schematic of the ND-LAr detector, showing a row of the 5 × 7 array of optically isolated ArgonCube modules [51].

As shown in Fig. 2.13 ND-LAr will move to take data from off-axis spectra, a capability referred to as DUNE Precision Reaction-Independent Spectrum Measurement (DUNE-PRISM) [50].

2.2.3.2 ND-GAr

The ND-GAr detector will be a magnetized system consisting of a high-pressure gaseous argon TPC (HPgTPC) surrounded by an electromagnetic calorimeter (ECAL), both in a 0.5 T magnetic field, and a muon detection system. As ND-LAr begins to lose acceptance for muons above ~ 0.7 GeV/c due to lack of containment, ND-GAr is needed to measure the momenta and charges of muons downstream of first detector. A schematic of ND-GAr is shown in Fig. 2.15.

The high pressure TPC, run at 10 atm, will provide a lower-density medium with excellent tracking resolution to analyse the momenta of ND-LAr muons. This technology will additionally contribute a large independent sample of νAr interactions from the neutrinos interacting with argon in the TPC. These events can be studied with a very low momentum threshold for charged particle tracking, excellent tracking resolution, nearly uniform angular coverage and with systematic uncertainties that differ from those of the liquid detectors. ND-GAr will be able to collect around 1.6×10^6 ν_μ charged current events per year of on-axis running with a 1.0 t fiducial volume.
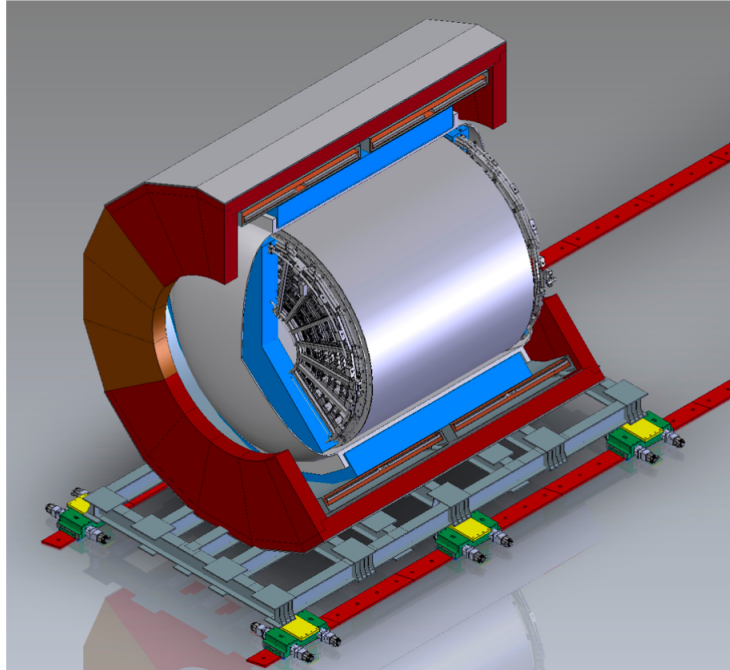
Fig. 2.15: Schematic of ND-GAr which shows the HPgTPC, its pressure vessel, the ECAL, the magnet and return iron yoke. The muon-tagging system detectors are omitted [50].

Since ND-GAr can access lower-momentum protons and has superior charged π capabilities than ND-LAr, it will be valuable for studying the charged particle activity near the interaction vertex. The misidentification of pions as knocked-out protons can cause significant misreconstructions of neutrino energies and event types, mostly in the LArTPCs: ND-GAr will thus play a key role in understanding how often such mistakes occur in ND-LAr and in the FD modules.

The relatively low level of secondary interactions in the gas will help at identifying particles produced in the primary interaction and at modelling secondary interactions in denser detectors. Like ND-LAr, ND-GAr will move to perform PRISM measurements of off-axis spectra [50].

2.2.3.3 SAND

The ND component permanently on the beam axis is the System for on-Axis Neutrino Detection (SAND). This multi-purpose detector will monitor the flux of neutrinos going to the FD from an on-axis position, which guarantees a higher sensitivity to variations in the neutrino beam. SAND will serve as a dedicated neutrino spectrum monitor, allowing to potentially adjust the beam model should any changes be detected. The design

of SAND is mostly based on the reuse of the magnet and electromagnetic calorimeter (ECAL) of the KLOE experiment, a view of which is shown in Fig. 2.16, with the inner volume of the ECAL being instrumented with a target/tracking system [50].
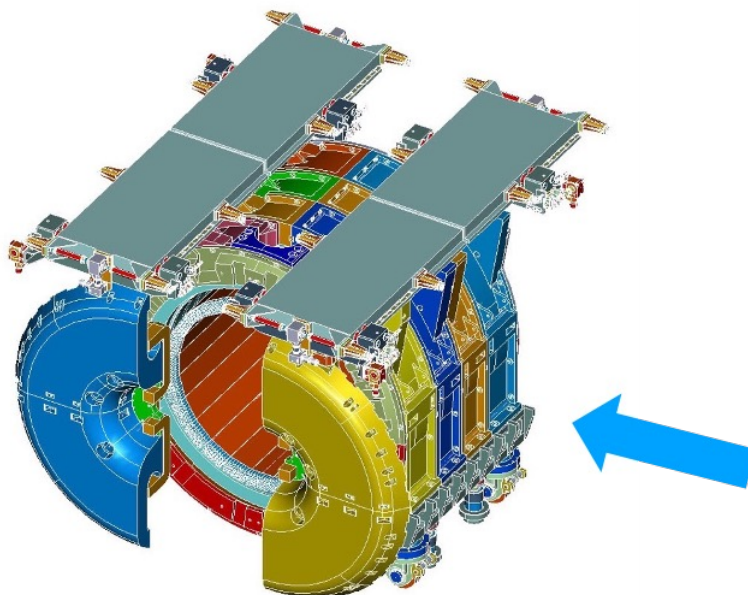
Fig. 2.16: 3D View of the KLOE magnet and ECAL. The neutrino beam direction at DUNE is indicated by the blue arrow.

SAND magnet and ECAL   The magnet, with its return yoke, and ECAL will be repurposed from the KLOE detector at the INFN LNF laboratories, previously used to study ϕ meson production. A scheme of KLOE systems is shown in Fig. 2.17. KLOE's solenoidal superconducting coil will provide a ~ 0.6 T magnetic field over a 4.3 m long, 4.8 m diameter volume.

The KLOE electromagnetic calorimeter is a lead/scintillating-fiber sampling calorimeter offering good light transmission over several meters, sub-ns timing accuracy and a very good hermeticity. The barrel calorimeter is cylindrical and located inside the KLOE magnet, close to the cryostat. It is divided into 24 modules, each 4.3 m long and 23 cm thick, with a trapezoidal cross section having 0.7-3.9 m bases. The two calorimeter end-cap modules consist each of 32 rectangular cross section modules. $0.7 - 3.9$ m long and 23 cm thick.

All ECAL modules are constructed as a stack of 200 grooved, 0.5 mm thick, lead foils alternating with 200 layers of cladded 1 mm scintillating fibers. KLOE took data until
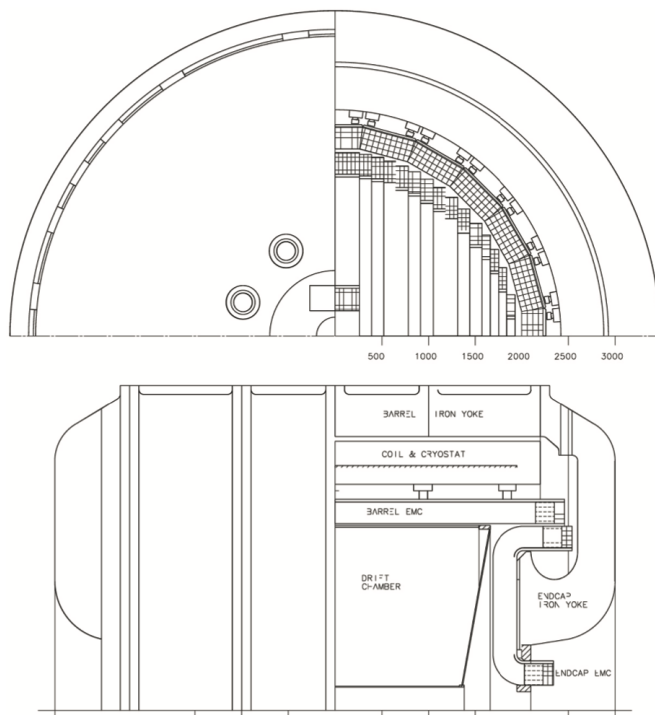
Fig. 2.17: Front (top) and side (bottom) views of the calorimeters, showing the trapezoidal barrel and vertical endcap modules and their location inside the magnet. Units are in mm [50].

march 2018: up to the end, the ECAL and time and energy resolution were found to be:

$$
\begin{aligned}
\text{Energy resolution:} \quad & \sigma/E = \frac{5\%}{\sqrt{E\,(\text{GeV})}}, \\
\text{Time resolution:} \quad & \sigma = \frac{54}{\sqrt{E\,(\text{GeV})}}\ \text{ps}.
\end{aligned}
\tag{2.2.1}
$$

The inner tracker. The option that has been chosen for the inner tracker has most of the volume inside the ECAL filled with Straw Tube Tracker (STT) modules, with the exception of a small upstream region instrumented with a LAr active target.

STTs are designed to offer a control of the configuration, chemical composition and mass of neutrino targets similar to that achieved in electron scattering experiments. The base tracker technology of STTs is provided by low-mass tungsten straws (5 mm diameter, 12 μm walls with 20 μm gold plating) operated with a 70%/30% Xe/CO$_2$ mixture at 1.9 atm, a similar design to the ones used in many precision physics experiments. The single hit space resolution is designed to be < 200 μm.

The STT design features hydrocarbon targets, which, having a different mass number

56

relative to argon, can provide information for developing nuclear effects models and improving the confidence in the interaction model and the size of several systematic uncertainties. Specifically, thin target layers ($\sim 1-2\,X_0$) of passive material with high chemical purity are placed between the straw layers, distributing, in such a way, the target mass throughout the volume. The current design will make use of ~ 4.7 t of polypropylene (CH_2) foils in 78 modules and of 504 kg of graphite.The average density is 0.18 g/cm^3, corresponding to a total thickness of the system of $1.33\,X_0$. The choice of passive target materials, together with their vertex, angular, momentum and timing resolutions are key factors for the correct association of neutrino interactions to each target element. The total number of straws in the STT is over 2×10^5, for the same number of channels. Fig. 2.18-right illustrates the inner volume of SAND, with an STT module shown on the right.

The GRAIN active target. The design of SAND envisages the GRAIN (GRanular Argon for Interactions of Neutrinos) active liquid argon target in the upstream part of the magnetized volume, with the main roles of constraining nuclear effects and providing a complementary Ar target permanently located on-axis for cross-calibration, as the Ar-based ND-LAr and ND-GAr detectors will be positioned off-axis for $\sim 50\%$ of the time [50, 52]. Fig. 2.18 shows two views of the GRAIN active target inside the SAND inner volume.

The LAr target mass will be of $\mathcal{O}(1\mathrm{t})$ with a small enough thickness along the beam direction ($\sim 1\,X_0$) for energy loss, showering and multiple scattering to be reduced, as the outgoing particles will have to be analysed by the downstream STT. The cryostat walls will be made of C-composite material reinforced by internal thin aluminium foil. The exact positioning, size and shape of the active target are still in the process of optimization. GRAIN is a novel LAr detector, designed to reconstruct neutrino interactions using only the scintillation light. It will be instrumented with an optical detection system to collect Vacuum UV scintillation light on fine segmented focal planes.

Two VUV imaging systems are being developed at the time of this work: one based on biconcave lenses and one using Coded Aperture Masks. As the two technologies feature several complementary capabilities, the final design of the detection system will likely feature a combination of both lenses and masks [50].

The main objective of this thesis is the development of track reconstruction algorithms for the Hadamard-Mask-based design of the LAr active target, the details and theoretical basis of which will be discussed in Section 3.
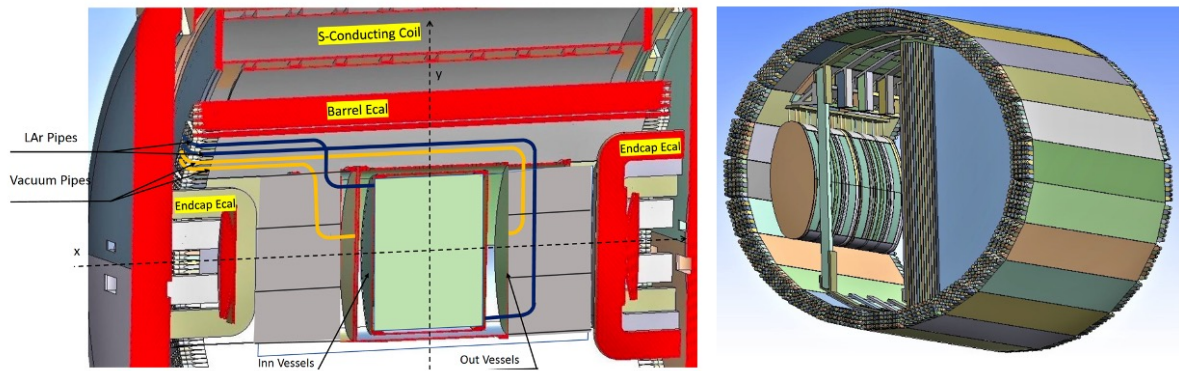
Fig. 2.18: (Left) Cutaway view of the inner volume of SAND, showing the position and vessel structure of GRAIN. (Right) View of the inner volume detectors of SAND: inside the KLOE calorimeter an STT module is shown on the right, with the GRAIN cryostat being on the left.

Chapter 3

Coded Aperture imaging in GRAIN

In Section 2.2.3.3, the rationale behind the development of a LAr active target volume for the SAND detector was outlined. A LAr target at the near detector complex would enable a study of the neutrino interaction topologies and cross sections which would be complementary to the measurements at the far detector, thus allowing to better constrain the systematics. The LAr target volume for the SAND detector could therefore supplement the ND-LAr TPCs, by permanently providing on-axis data [50, 52]. The two significant shortcomings of a traditional LArTPC in the SAND environment are the electron drift time of the order of ms, too slow to cope with the high event rate at the ND, and the required placement of the target inside the magnetized volume.

The scintillation properties of liquid argon allow, instead, to perform both calorimetric and spatial measurements by means of an optical detection system capable of collecting the VUV scintillation emission. For minimally ionizing particles liquid argon has a light yield of $\sim 4 \times 10^4$ photons per MeV of deposited energy [53], with an intensity peaking at 128 nm and a fast component decay time of 7 ns. Moreover, its Rayleigh scattering length at 128 nm is of ~ 99 cm [54], while the attenuation length is of the order of 66 cm [54].

LAr is fairly transparent to its own scintillation emission, which can be therefore used for imaging purposes, allowing to potentially cut the response time down to a few nanoseconds while maintaining high spatial resolution. Leveraging these properties requires an optical system capable of collecting enough light and a fast and segmented photodetector capable of providing an adequate resolution [55].

The development of such an imaging system presents serious challenges due to the unusual environment of the LAr target and to the needed high level of performance:

- Traditional lenses and mirrors have a highly inefficient transmission for Vacuum Ultra-Violet light, so that novel solutions are required.

- The readout electronics must be able to operate in cryogenic conditions and with single-photon detection capabilities.

- The distance of event tracks can be up to several meters, requiring a large field of view and depth of field to focus as many tracks as possible.

A possible approach to this problem is one already well known in X-ray and gamma-ray astronomy, but never used so far in particle physics experiments: the Coded Aperture Mask technique.

In such an optical detection system, the scintillation light signal would be filtered by Coded Aperture masks, placed on the sides of the cryostat, and read by matrices of Silicon Photomultipliers (SiPMs). These will provide the necessary performances, as they offer the advantage of robustness, a strong reduction of the dark noise at low temperatures and a high definition thanks to the large number of closely packed pixels. Coded Aperture masks will, concurrently, provide a sufficiently high photon detection efficiency without the need for special materials or complex designs. The signals, namely 2D images, detected by multiple mask-SiPM systems could then be combined in a *stereo view*, obtaining a 3D reconstruction of an event from its scintillation light [55, 56].

This chapter will first outline the principles behind and optical properties of Coded Aperture masks, presenting a number of their potential designs. The current mask-based design of the LAr active target, on which the rest of the work is based on will then be discussed. Lastly, the 3D reconstruction techniques, which are currently still in development, will be briefly touched upon.

3.1 Principles of Coded Aperture imaging

Coded Aperture Imaging techniques were being applied by the '70 in the field of X-ray imaging, and have since become a staple in X-ray and gamma-ray astronomy [57, 58]. In the original formulation, the single opening of a *pinhole camera* is replaced by many pinholes (collectively forming an *aperture*) arranged according to some pattern. Each point of a light-source will deposit a shadow of the aperture on the detector surface and the overall pattern of light and shadows can be processed, generating a reconstructed image of the original object [59].

As the pattern projected by the aperture is a combination of single pinhole images, it is appropriate to start by discussing the principles of pinhole cameras.

3.1.1 Pinhole cameras

The so-called pinhole camera could be rightly considered the simplest imaging device: it consists of just a slab of material opaque to radiation through which an infinitely small (ideally dimensionless) hole is poked. As every photon that passed through the hole must have travelled from the source, assumed at infinity, in a straight line, every point in the detection plane represents a point on the source. The detected photon

distribution recorded by detector is, moreover, an inverted picture of the source, with a 1-1 correspondence between the two, as the scheme in Fig. 3.1 shows.

Formally, the photon distribution $R(x_i, y_i)$ on the detector plane must be due only to the (x_0, y_0) point at the source, itself a point source with irradiance $O(x_0, y_0)$. Specifically, $R(x_i, y_i)$ and $O(x_0, y_0)$ must be proportional:

$$R(x_i, y_i) \propto O(x_0, y_0). \tag{3.1.1}$$
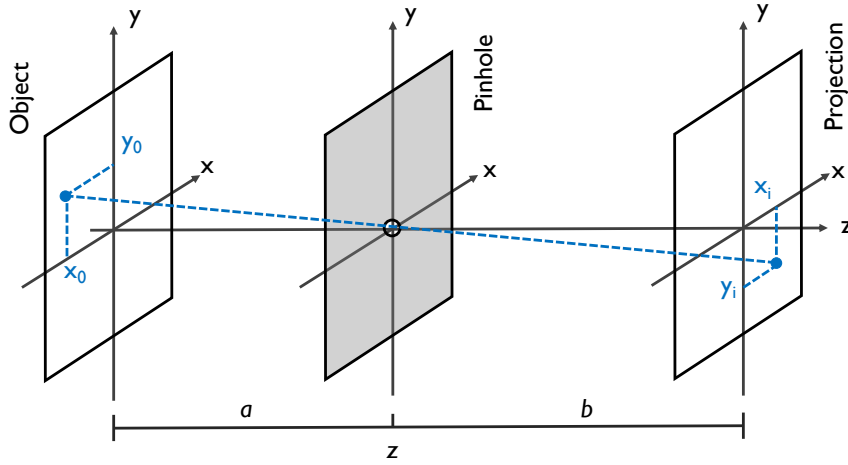
Fig. 3.1: Geometry of a pinhole camera.

Referring to the notation of Fig. 3.1, by defining the vectors

$$\vec{r_i} = (x_i, y_i) \quad \text{and} \quad \vec{r_0} = (x_0, y_0), \tag{3.1.2}$$

and being a and b respectively the distances from the pinhole to the object and detector planes, eqn. (3.1.1) becomes:

$$R(x_i, y_i) \propto O\left(-\frac{a}{b}\vec{r_i}\right), \tag{3.1.3}$$

thus showing that the projection through the pinhole is a copy of the object, inverted (because of the $-$ sign) and rescaled by a factor a/b, where a and b can be any positive number. If $a > b$, i.e. the pinhole is closer to the detector than to the object, the latter appears minified, while if $a < b$, the object appears magnified. Indeed, the ratio of the projected size of the object to the original, called *magnification coefficient* m_p of the pinhole can be verified to be $m_p = b/a$.

61

The magnification determines the Field of View (FoV) of the camera, i.e. the set of points in the plane of the object that can be measured; being d_d the size of the detector, it holds:

$$\text{FoV} = \frac{d_d}{m_p} \tag{3.1.4}$$

The discussion above assumed an ideal dimensionless pinhole: to understand the necessity of Coded Aperture masks for physics applications it is necessary to move to the realistic case instead, illustrated in Fig. 3.2. If the pinhole had a finite width w_m, each point would cast an image of size

$$w_d = \frac{a+b}{a} w_m = (1 + m_p) w_m. \tag{3.1.5}$$

Defining the resolution ℓ as the minimum distance between two points in the object plane such that their projections are separate in the detector image, one has:

$$\ell \geqslant \frac{a}{b} w_d = \left(1 + \frac{1}{m_p} \right) w_m, \tag{3.1.6}$$

where low ℓ values indicate a good resolution. This equation shows how resolution is limited by the size of the pinhole w_m. Moreover, while ℓ improves with increasing w_m, the FoV shrinks as per eqn. (3.1.4). The ratio of the two,

$$\frac{\text{FoV}}{\ell} = \frac{d_d}{(1 + m_p) w_m} \tag{3.1.7}$$

can be taken as a figure of merit for an imager, which, ideally, should have both the widest possible FoV and the highest possible resolution. Assuming $m_p = 0$ gives the highest and thus best ratio of d_d/w_m.

While the ideal pinhole has a perfect resolution, it cannot work in practice as a null aperture area would imply a null photon flux through the hole as well. Thus the dimension of the pinhole must be a compromise between the need for a high resolution and a high detection efficiency. The Coded Aperture mask technique has been developed to bypass this exact issue [60].

3.1.2 Coded Aperture masks

The rationale behind Coded Apertures is to achieve the resolution of small pinholes while maintaining a high throughput. The basic concept is to overcome the low passing photon flux by opening many small pinholes instead of a single large one. The pinholes can be arranged in specifically designed patterns, of which a *mask* is the physical realization. A mask coupled to the detector forms a Coded Aperture Camera.
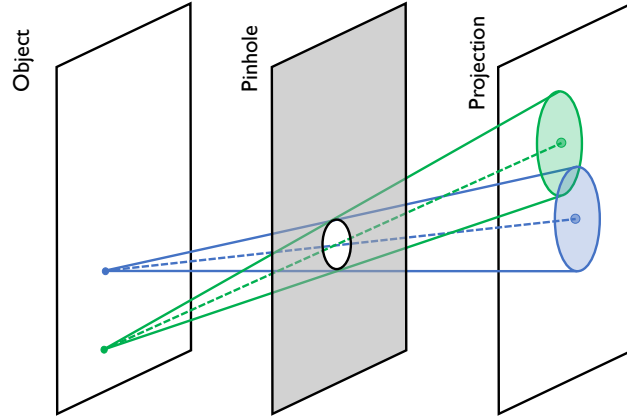
Fig. 3.2: Illustration of the resolution loss occurring when an ideal pinhole is enlarged to increase throughput. The dotted lines and corresponding circles indicate the projections in the ideal pinhole case.

The advantages of Coded Apertures over simple pinhole cameras can be quantified in terms of their respective signal-to-noise ratio (SNR). In fact, in the case of a point source, a single pinhole counting s photons would have a SNR$= \sqrt{s}$, according to Poisson statistics. If the same source were counted independently N times, as is the case of a Coded Aperture with N holes, the total average count and variance would be Ns, giving a SNR$= \sqrt{Ns}$. Thus the SNR advantage of Coded Apertures over single pinholes is $\sqrt{N}$.

3.1.2.1 Detector response in Coded aperture cameras

The response of the detector at the position $\vec{r}_i$ due to the point source $\vec{r}_0$ must be proportional to the irradiance $O(\vec{r}_0)$, modulated by the transmission of the mask A evaluated at the intersection point of the ray $\vec{r}_i - \vec{r}_0$. A is generally considered a two-value function, with 1s for holes and 0s for opaque elements. The response is thus:

$$R(\vec{r}_i) \propto O(\vec{r}_0)A\left(\vec{r}_0 + \frac{\vec{r}_i - \vec{r}_0}{z}a\right), \qquad (3.1.8)$$

where a and z have the same meaning as in Fig. 3.1. The total recorded photon distribution is obtained by repeating this argument over all point sources, i.e. integrating over the object plane:

$$R(\vec{r}_i) \propto \int_{\vec{r}_0} \int O(\vec{r}_0)A\left(\vec{r}_0 + \frac{\vec{r}_i - \vec{r}_0}{z}a\right) d^2\vec{r}_0. \qquad (3.1.9)$$

It is helpful to recast the previous equation using the following definitions:

$$O'(\vec{r}) \equiv O\left(-\frac{a}{b}\vec{r}\right) \quad \text{and} \quad A'(\vec{r}) \equiv A\left(\frac{a}{z}\vec{r}\right), \qquad (3.1.10)$$

where O' is the scaled and inverted version of O by the magnification coefficient m_p, so that O' is the pinhole image of the object. Similarly, A' is a scaled version of A: as $a/z < 1$, A' is larger than A. The magnification of A' is due to the projection of the mask pattern on the detector, with the ratio of the size of the projection (h_d) to that of the mask (h_m) being

$$\frac{h_d}{h_m} = \frac{z}{a} \tag{3.1.11}$$

Substituting eqn. (3.1.10) in eqn. (3.1.9) gives, recalling the definition of the *convolution* operation:

$$R(\vec{r}_i) \propto \int_{\vec{r}_0{}^i} \int O'(\vec{r}_0{}^i) A' \left(\vec{r}_i - \vec{r}_0{}^i\right) d^2\vec{r}_0{}^i = O' * A', \tag{3.1.12}$$

where $\vec{r}_0{}^i \equiv -(b/a) \cdot \vec{r}_0$ is the point associated to $\vec{r}_0$ in a pinhole imager. The previous equation shows that the projection is described by the convolution of the pinhole image O' with the projection of the mask pattern A'. A physical interpretation of this result is that the projection is the sum of all the magnified mask patterns, each shifted according to the position $\vec{r}_0$ of the point source casting the shadow and weighted according to its irradiance [60].

3.1.2.2 Decodification formalism

The reconstructed image can be obtained from the detector response $R(\vec{r}_i)$ through the *correlation method*, where the reconstructed object $\hat{O}$ is defined as:

$$\hat{O} \equiv R \otimes G = (O' * A') \otimes G = O' * (A' \otimes G), \tag{3.1.13}$$

where G is a decoding array, called *kernel*, and $\otimes$ and $*$ indicate the correlation and convolution operations respectively. Choosing a G such that

$$A' \otimes G = \delta, \tag{3.1.14}$$

leads to:

$$\hat{O} = O' * \delta = O', \tag{3.1.15}$$

which is the simple pinhole image, so that the system can reconstruct the exact initial image. The addition of a noise term N to the detector response $R \propto O' * A' + N$ does not change significantly the derivation, leading, for the same choice of G as in eqn. (3.1.15), to:

$$\hat{O} = O' * \delta = O' + N \otimes G. \tag{3.1.16}$$

In conclusion, the process of reconstruction entails the identification of a known pattern in a signal. This requires finding pairs (A, G) for which eqn. (3.1.14) holds. Fortunately, many families of aperture patterns A exist for which the G decoding matrices have known analytical expressions [60].

It is critical to note that the reconstruction procedure outlined so far allows to obtain a 2D image from a single camera, and as such is well suited for applications where information on the depth is irrelevant, e.g. X and gamma ray astronomy and medical or industrial imaging. In order to apply the Coded Aperture approach to a particle physics detector, as is being proposed for GRAIN, the information on all three coordinates of a source must be obtained for the event to be reconstructed.

The most obvious extension of the single camera technique to 3D imaging consists of combining the images captured by multiple cameras in different positions to obtain a *stereo view* of the event. As Section 3.2 shall outline, the difficulty in developing a combined reconstruction algorithm capable of working with the low efficiency of the available detectors is the limiting factor for this technique, which is not yet mature.

3.1.2.3 Geometric arrangements

The imaging characteristics of a Coded Aperture camera depend on the geometric arrangement between mask and detector. The projection of the mask on the detector distinguishes two regions in the Field of View: the Fully-Coded Field of View (FCFV), in which sources can project a complete mask pattern on the detector, and the Partially-Coded Field of View (PCFV), in which the projection on the detector is not complete. It is clear that perfect imaging according to the decoding procedure in Section 3.1.2.2 is only possible if complete mask patterns are detected.

Under the assumption of a point source located at infinity, so that the projection of the mask on the detector has the same size as the mask itself, the most straightforward arrangement, with mask and detector having the same size, has a FCFV consisting of a single point along the instrument axis, as Fig. 3.3a shows. All other point sources are part of the PCFV, as they only project part of the pattern on the detector, and cannot be reconstructed perfectly.

The most direct solution for increasing the FCFV, increasing the detector size as in Fig. 3.3b, is seldom the most practical, as fabrication issues or cost set a limit on the detector size. In GRAIN, larger detectors would also take up a larger fraction of the volume and increase the heat load of the LAr chamber. In such cases it is more convenient to enlarge the mask by replicating its pattern in a periodic tiling, or *mosaic*, arrangement, shown in Fig. 3.3c. With this arrangement all sources within the FCFV still project an entire mask pattern on the detector, as the pattern is periodic, but the pattern shifts are different depending on the source position, as Fig. 3.3d shows. Fig. 3.4 illustrates the FCFV and PCFV regions for a non-cyclic and mosaicked geometry.

A complication introduced by mosaic patterns is the so-called *aliasing*: as all the points at the the boundary of the FCFV project the same pattern, they are reconstructed as the same point despite being in different positions. Due to aliasing, mosaics cannot go beyond a 2×2 repetition of the mosaic pattern, but should rather leave out a row and a column [60].
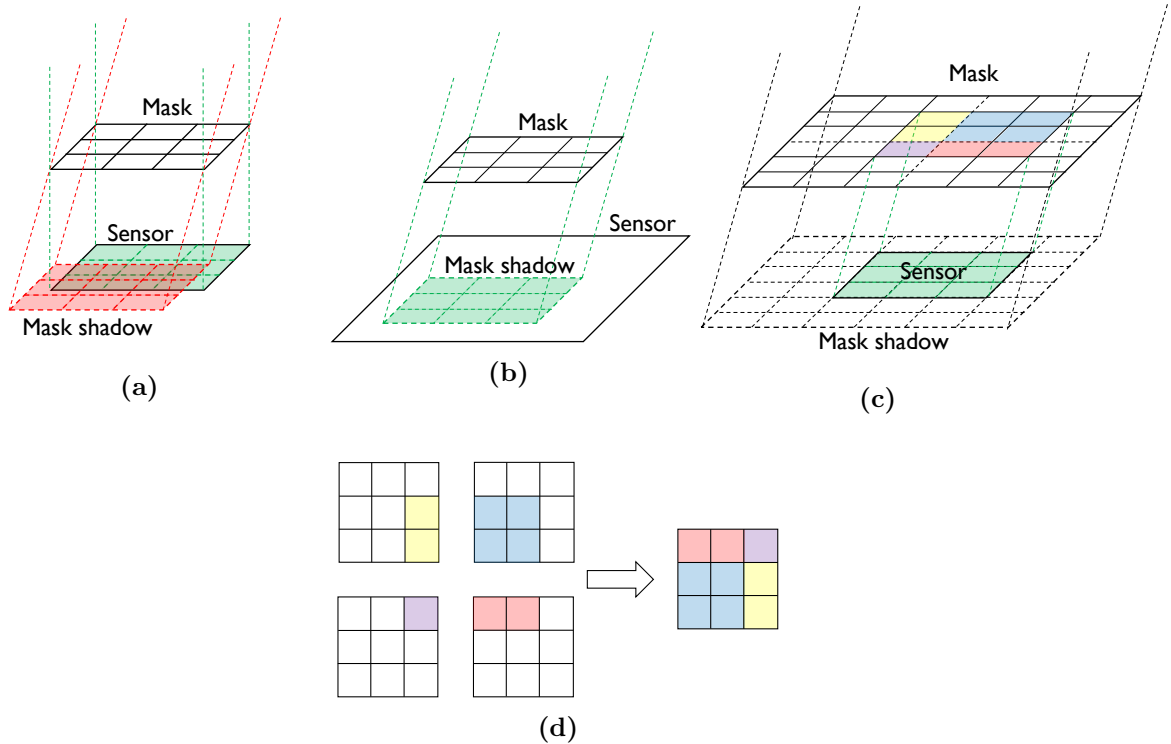
Fig. 3.3: Comparison of three different Coded Aperture camera arrangements, with a point source at infinity. (a) Mask and detector have the same size: only the sources on the optical axis project the full mask shadow on the sensor. (b) The sensor is larger than the mask, extending the FCFV region. (c) Mask composed of a 2×2 mosaic of the mask in (a) and (b), while the sensor has the same dimensions as in (a). Only part of the mask is projected in the sensor. (d) The combination of projected parts of the mosaic in (c) is the full shadow of one of the base mask patterns.

3.1.2.4 Field of View and resolution

The two main parameters for Coded Aperture cameras are the FoV and the geometric resolution, i.e. the resolution intrinsic to its geometric arrangement, assuming the detector to be ideal. As for simple pinholes, these two quantities are strictly related to each other and to the parameters of the detector.

For a single period mask camera, a source at a finite distance, the so-called near field configuration, will be projected according to the magnification coefficient

$$m = 1 + \frac{b}{a} = 1 + m_p, \tag{3.1.17}$$

where the notation in Fig. 3.1 is used. If the side of the mask is d_m and $d_d > d_m$ is the side of the detector, the projection will have a size md_m, which leaves a space $(d_d - d_m)/2$
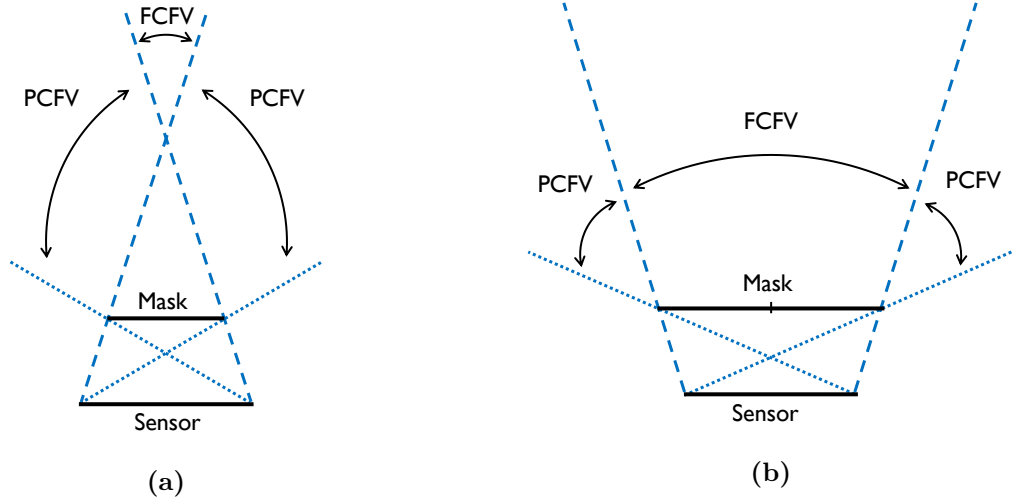
Fig. 3.4: Scheme of the FCFV and PCFV for a camera with a single mask (a) and for one with a 2×2 mosaic mask (b). The detector is assumed to be larger than a mask tile.

on both sides of the detector to shift the mask. This corresponds to a field of view

$$\text{FoV} = \frac{d_d - md_m}{m - 1} = \frac{d_d}{m - 1} \cdot \frac{md_m}{m - 1}. \tag{3.1.18}$$

In the case of a periodic 2×2 mosaic, only one of the four copies of the basic pattern covers the detector completely, leading to a field of view

$$\text{FoV} = d_d \cdot \frac{a}{b} = \frac{d_d}{m - 1}, \tag{3.1.19}$$

which can be readily seen to be larger than the FoV of a non-periodic arrangement for a given d_d. Mosaics are therefore preferable over single patterns for a given dimension.

In Section 3.1.1 the resolution of an imager was defined as the minimum distance between two point sources so that their image is still perceived as two separate points. For a Coded Aperture system this definition translates to the distance that two sources must have for their projections to be a projection of a mask hole apart. This spacing λ_g is found to be:

$$\lambda_g = \frac{mp_m}{b} \cdot a = \frac{m}{m - 1} \cdot p_m, \tag{3.1.20}$$

where p_m is the size of a mask hole. A relation between FoV and resolution equivalent to eqn. (3.1.7) can thus be derived for periodic mosaic configurations:

$$\frac{FoV}{\lambda_g} = \frac{d_d}{mp_m} = \frac{d_m}{p_m} \equiv n, \tag{3.1.21}$$

as the projection of the mask takes the whole detector, so that for all shifts $d_d = md_m$. The ratio $d_m/p_m = n$ is the number of *mask elements* (holes and opaque cells) on the side of the mask, if connection elements are neglected, so that the relation between FoV and resolution, FoV $= \lambda_g n$ is independent of magnification. A good geometrical resolution requires masks with the highest possible number of elements. Conversely, for a given resolution, a large FoV is only possible for large patterns. A third implication is that in a given mask, FoV can be traded for resolution and vice versa by acting on the magnification, which depends on the a and b distances.

Finally, the effect of the detector dimension on the geometric resolution is found to be determined by

$$\lambda_g = p_m \cdot \left(1 + \frac{\text{FoV}}{d_d}\right), \qquad (3.1.22)$$

which implies that a large detector allows better resolution for a given FoV [60].

3.1.2.5   Depth of field

For lenses, the distance range at which objects can be focused sharply, or Depth of Field (DoF), is defined by the focal length. Coded Aperture optical systems, on the other hand, do not focus light and in theory should produce collimated images at infinity. This would enable the focusing of tracks at any distance, greatly simplifying the reconstruction. In reality, the sharpness of Coded Aperture images is constrained by the sampling artefacts emerging when the shadow of a mask element is projected over a non-integer number of pixels, which act as a limiting factor for the collimation. This allows to define a concept of focusing in analogy to lenses. The aforementioned number of pixels α is given by

$$\alpha = \frac{mp_m}{p_d} = \frac{\left(1 + \frac{b}{a}\right)p_m}{p_d}, \qquad (3.1.23)$$

so that the camera configurations for which focusing is possible are those close to $\alpha = 1$, with successive αs identifying increasing in-focus magnifications. The size of the DoF is thus defined by the derivative

$$\frac{d\alpha}{da} = -\frac{p_m b}{p_d a^2}, \qquad (3.1.24)$$

so that, as typically $p_m \simeq p_d$, cameras that focus ($\alpha = 1$) at large distances have very small variations of α with a, i.e. a nearly infinite DoF, while configurations with a small focusing distance will have a really small DoF [55].

From these results it follows that the optimal camera configurations for event reconstruction are those with large focusing distances a. This characteristic will be crucial for determining the design of the optical system for GRAIN [60].

3.1.2.6 Mask patterns

In the previous section the validity of the Coded Aperture approach to imaging over single pinhole cameras was illustrated, deriving the figures of merit of such systems and outlining the analytical decoding procedure which is typically used in imaging applications. In particular, the advantages in FoV and resolution granted by masks with large dimensions and using periodic mosaic patterns were outlined. With a view to the potential use of analytical 3D reconstruction such masks should also have specific mathematical properties that make decoding possible.

The mask designs that are currently being considered for the GRAIN optical readout system are based on the Modified Uniformly Redundant Array (MURA) family of coded aperture patterns, introduced in [57] as a modification of the previous URA masks [59]. Square MURA masks can be generated in any length p of pixels, called *rank*, that is prime. The binary array of the aperture $A = \{A_{ij}\}_{i,j=0}^{p-1}$ is constructed with the prescription

$$
A_{ij} = \begin{cases} 0 & \text{if } i = 0, \\ 1 & \text{if } i = 0, j \neq 0, \\ 1 & \text{if } C_i C_j = +1, \\ 0 & \text{otherwise} \end{cases}
\tag{3.1.25}
$$

where

$$
C_i = \begin{cases} +1 & \text{if } i \text{ is a quadratic residue modulo } p, \\ -1 & \text{otherwise} \end{cases}
\tag{3.1.26}
$$

As mentioned before, in this notation holes have $A_{ij} = +1$ while for opaque pixels $A_{ij} = 0$. Fig. 3.5 shows the MURA patterns for p up to 17.

The decoding kernel G for MURA apertures A_{ij} can be constructed as follows:

$$
G_{ij} = \begin{cases} +1 & \text{if } i + j = 0, \\ +1 & \text{if } A_{ij} = 1, \ (i + j \neq 0) \\ -1 & \text{if } A_{ij} = 0, \ (i + j \neq 0) \end{cases}
\tag{3.1.27}
$$

The relation in eqn. (3.1.14) between a MURA and its decoding matrix is illustrated in Fig. 3.6 for a 17×17 aperture: the $A \otimes G$ correlation product yields a point-like image-matrix, which is the discrete equivalent of a δ.

A property which makes MURA patterns optimal for analytical reconstruction techniques is that the *Periodic Autocorrelation Function* (PACF) of the aperture has constant
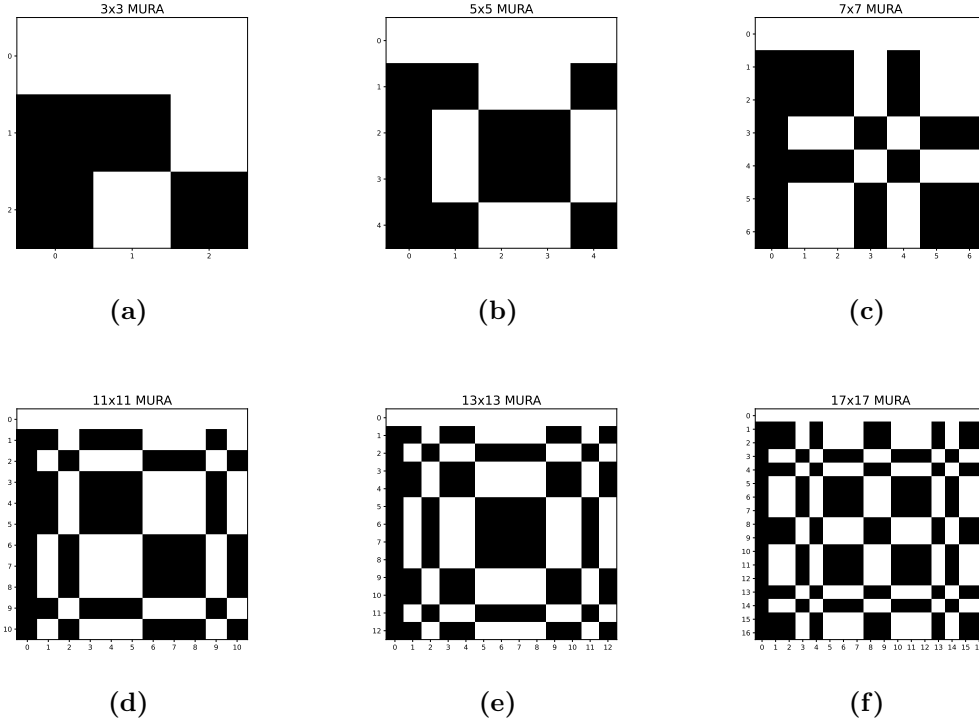
Fig. 3.5: Squared MURA aperture patterns for prime p up to 17. Black pixels indicate the holes ($A_{ij} = +1$) while the white ones indicate the opaque elements ($A_{ij} = 0$).

sidelobes, i.e.

$$
\begin{aligned}
\phi(l, k) &= \sum_{i=0}^{p-1} \sum_{j=0}^{p-1} A(i, j) A(i + l \bmod p, j + k \bmod p) \\
&= \begin{cases} K & (l, k) = (0, 0) \\ \lambda & \text{otherwise} \end{cases} \quad,
\end{aligned}
\tag{3.1.28}
$$

where the peak K and the sidelobe parameter λ are numbers to be determined. Such a property gives the optimal compromise between the reduction of *coding noise* (artefacts) and the amplification of coherent effects [56]. Fig. 3.7 shows the constant sidelobe PACF of a 17×17 MURA matrix, together with the corresponding histogram of occurrences.

Another important property of MURAs is the throughput of the aperture, i.e. the fraction of open elements with respect to the total number, is always around 50%. For a squared mask with sides of p pixels, the number of open elements is indeed found to be:

$$
N_{open} = \frac{p^2 - 1}{2} = \frac{N_{total} - 1}{2}
\tag{3.1.29}
$$
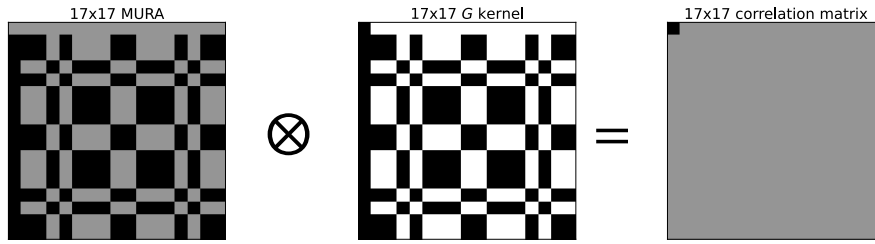
Fig. 3.6: Illustration of the $A \otimes G = \delta$ correlation product property. The grey-scale pixel colours white, grey and black correspond to $-1, 0, +1$ respectively.

(a)	(b)
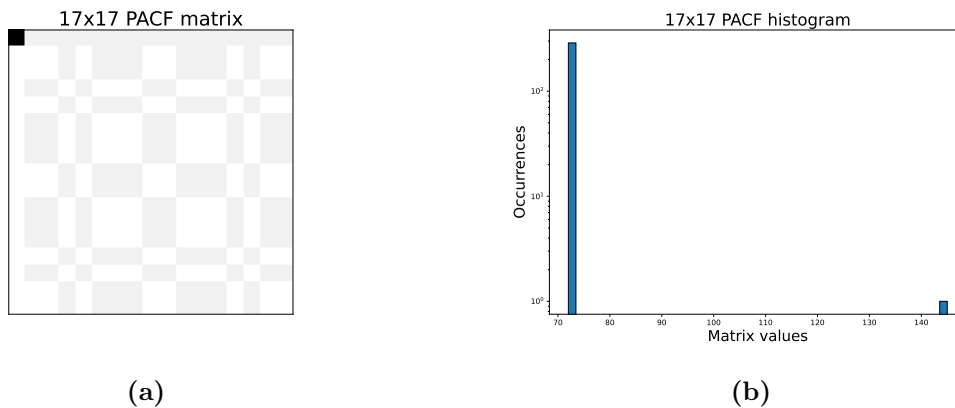
Fig. 3.7: Periodic Autocorrelation function of a 17×17 MURA matrix. In (a) the greyscale matrix plot is shown: only a pixel has the peak value, while the sidelobe being two-valued is an artefact due the discretization of the pattern. The corresponding histogram of occurrences for the PACF values is shown in (b), where a logarithmic scale in y has been chosen to improve the readability.

As discussed in Section 3.1.2.3, periodic mosaic patterns are the optimal solution for increasing the FCFV for a given detector size. Two different mosaic types are being considered, at the time of writing, for application in the GRAIN detector, having side dimensions $2p-1$ and $2p$ respectively, where p is as usual the rank of the base MURA. For a given p and a certain size of the pixels, the two designs will have slightly different dimensions, which will impact the FoV and geometric resolution.

The $2p-1$ odd-dimension mosaic patterns are straightforwardly obtained by tiling four p-rank MURAs in a $2p \times 2p$ pattern and then cutting the 0th row and 0th column. As the tiling of MURAs is periodic, the resulting pattern can be permutated in any direction. Such a pattern does not preserve the autocorrelation properties of the base MURAs: the PACF, computed for the mosaic according to eqn. (3.1.28), does not have

71

constant sidelobes.The mosaic pattern for a rank 17 base MURA is shown in Fig. 3.8 together with ithe PACF and its related histogram.

(a)

(b)

(c)
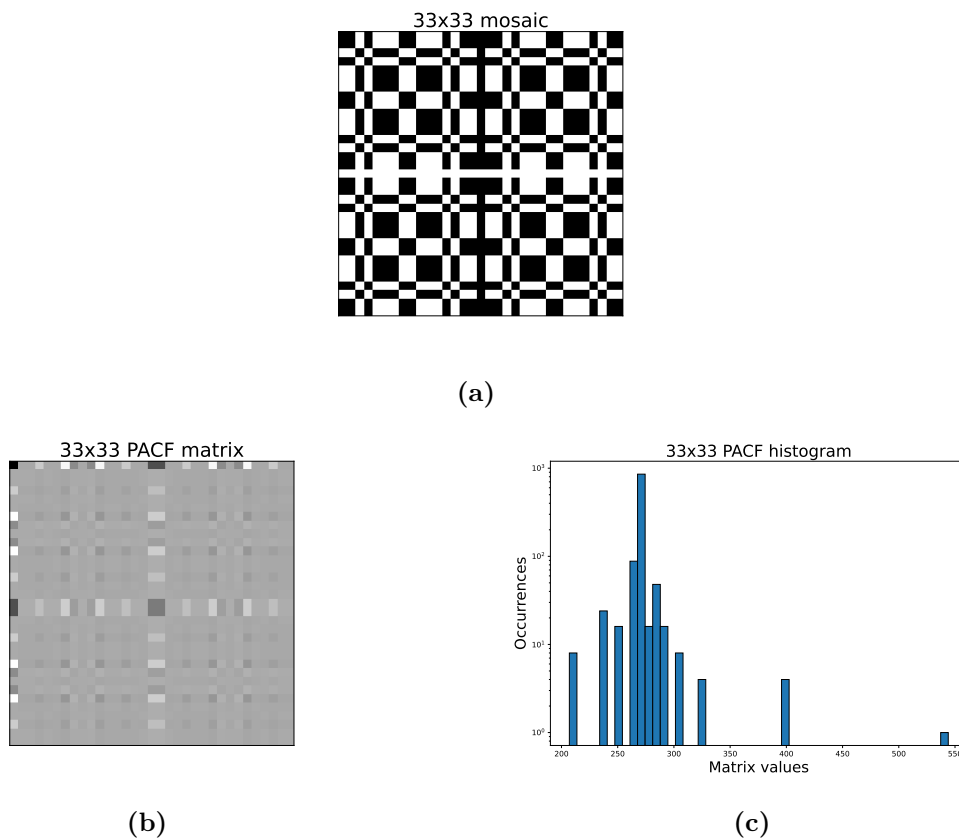
Fig. 3.8: (a) Odd-dimension mosaic pattern for a 17×17 base MURA. The greyscale matrix plot of the PACF is shown in (b): the values of the autocorrelation have a visible dispersion, as the corresponding histogram of occurrences in (c) shows. A logarithmic scale for y in (c) has been chosen to improve the readability.

The second type of mosaics, with $2p$ even dimensions has been shown in [56] to maintain the autocorrelation properties of the base MURAs. The patterns are obtained by cyclic permutations of rows and columns of a tiling of four MURAs, or by equivalent operations. Being periodic, this pattern too can be permutated in any direction. The mosaic pattern for a rank 17 base MURA is shown in Fig. 3.9 together with ithe PACF and its related histogram.
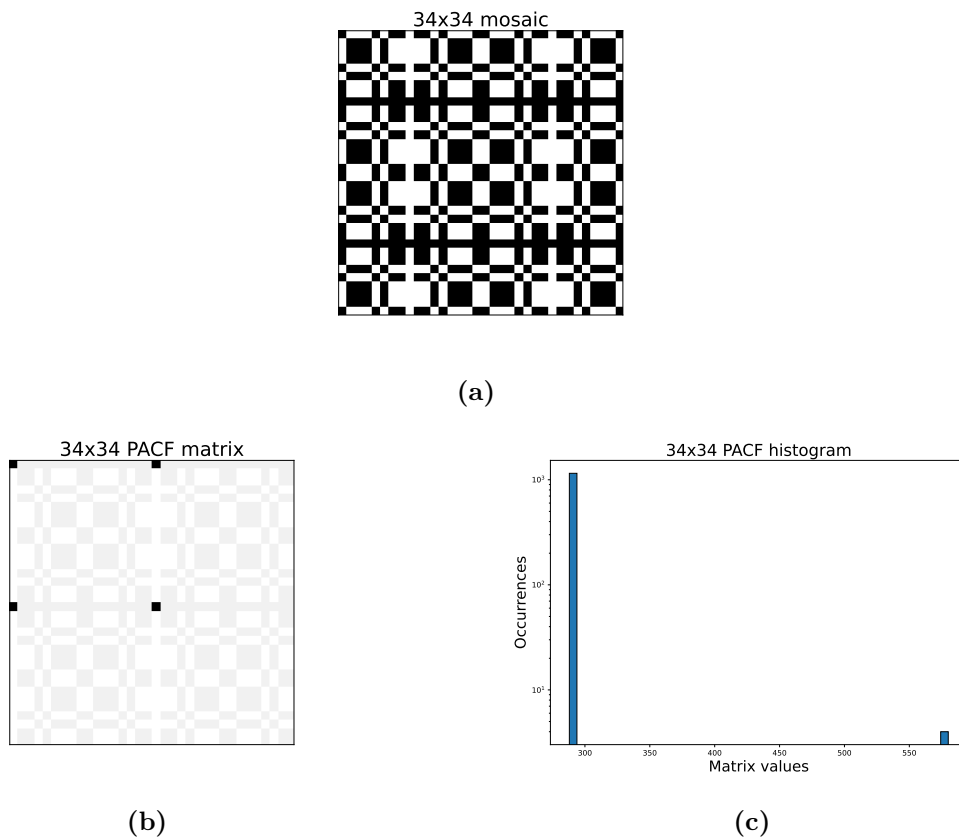
Fig. 3.9: (a) Even-dimension mosaic pattern for a 17×17 base MURA. The greyscale matrix plot of the PACF is shown in (b): the autocorrelation has constant sidelobes as the corresponding histogram of occurrences in (c) shows. The sidelobe being two-valued is an artefact due the discretization of the pattern. The four peak values of the PACF are due to the periodicity of the mosaic. A logarithmic scale for y in (c) has been chosen to improve the readability.

3.2 3D reconstruction techniques

The choice of MURA mosaics for the Coded Aperture cameras of the GRAIN optical system has been made on the grounds of their optimal characteristics for the analytic decoding of the detected images: the relatively high throughput, a constant sidelobe autocorrelation and a known expression for the decoding kernel G of matrices of any rank p in the family. The decoding of the 2D images of each mask in the detector would be, with this rationale, the first step of a analytic 3D reconstruction algorithm, which would combine the decoded images from each camera to obtain a three-dimensional view of the event.

As anticipated in Section 3.1.2.2, the main obstacle for this technique is the low Photon Detection Efficiency (PDE), just 20-25%, to the VUV scintillation emission of the

current SiPMs capable of working in LAr. Such a low PDE makes it difficult to perform the reconstruction as the projection of a complete mask pattern by each point-source constituting the event cannot be taken for granted. The 3D analytical reconstruction technique is still being developed at the time of writing of this dissertation.

The alternative solution to the problem of 3D reconstruction of images from Coded Apertures in GRAIN uses a combinatorial approach to perform a direct 3D reconstruction of the image: for each detected photon, a probability is projected in the reconstruction volume, segmented in voxels, through all possible mask holes. The true light sources of the event should correspond to the highest probability voxels.

The direct 3D reconstruction technique can work with masks of any design, not just MURAs, as it does not use the decoding properties of the aperture patterns. Additionally it is well-suited to operate with low light-yields, as the probability propagation is done for each photon individually. Its only main drawback is that it is computationally heavy, requiring GPU acceleration for the computation of the amplitude projection weights.

This technique too is still being actively developed at the time of writing and, despite having a less developed mathematical background, it is in a more mature stage code-wise than the analytical method. As such the events used in this thesis work will be obtained using the 3D direct reconstruction technique, and the main result of the dissertation will be the assessment of the quality of the reconstruction by comparing it with the Monte Carlo truth.

3.3 The GRAIN design

Before moving to the main results of this dissertation it is necessary to detail the relevant dimensions and parameters of the GRAIN LAr active target and of its Coded Aperture imaging system that have been used for the simulations in the remainder of the thesis work. It is important to note that the details of the GRAIN design are far from fixed, as the detector is still in the early phases of its development, and so are those of the imaging system, both in its mask-based and in its lens-based version.

The inner volume of the cryostat, the relevant region for this thesis work, has a width (along the x axis) of 130 cm, with elliptical sides (along the y-z plane) of 147.6 cm in height and 47.5 in length, respectively along the y and z axes. The neutrino beam direction in the simulations is along the positive z axis, consistently with Fig. **??**. A scheme of the GRAIN inner volume is shown in Fig. 3.10.

The imaging system is composed of 76 Coded Aperture cameras, 8 on each elliptical side, 25 on each of the curved faces and 10 on the top and bottom of the inner volume along the x-axis, five on each side. Such a number of cameras is the highest that is possible to fit given their dimensions. The mask patterns are 33×33 odd-dimension mosaics of the rank-17 base MURA. The sides of the mask pixels are 2.33 mm long, with a 0.2 mm edge between each pixel, for a total mask length of 94 mm. Masks are cut out
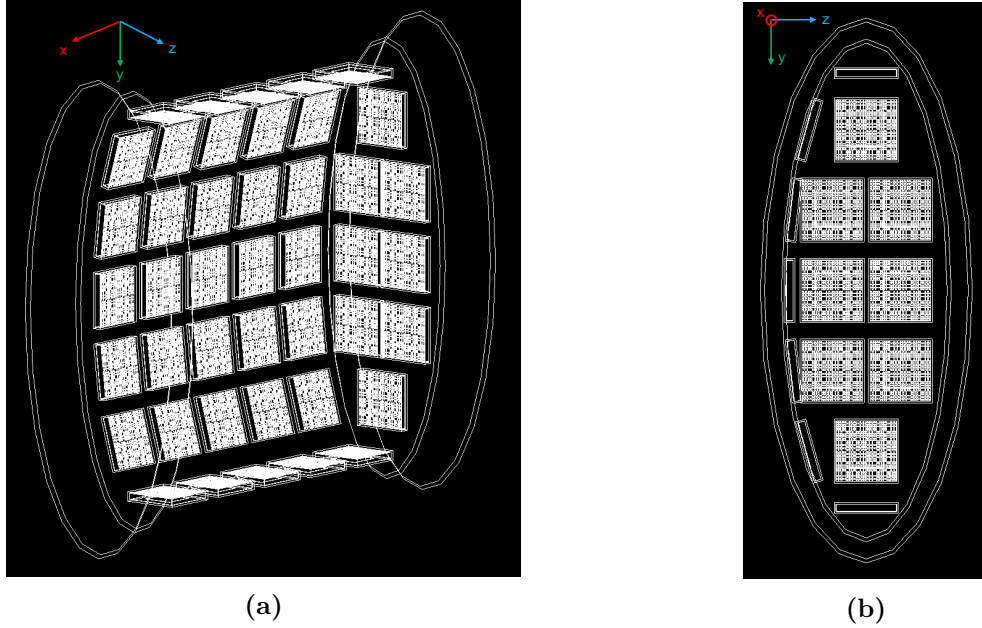
Fig. 3.10: Frontal (a) and side (b) views of the GRAIN geometry that has been considered in this dissertation. The disposition of the cameras maximises their possible number. In (a) the front-facing side is cut to allow a better view of the inner volume. The neutrino beam direction is along the positive z-axis. The front facing side has been cut for better viewing.

of a 0.1 mm thick steel sheet.

The geometric configuration of the cameras is designed so that the cameras can provide complementary depths of field, with $\alpha \simeq 1$ at 50 cm from each mask plane. This requires a distance b between mask and detector plane of 20 mm.

The detector is a 32×32 pixel SiPM array with a pixel size of 3 mm and pixels separated by a 0.2 mm spacing, for a total detector side length $d_d = 51.2$ mm. The SiPM detector model is still being developed, so the parameters and response assumed for the simulations are reasonable estimates. The thickness of the detector assembly is 1 mm. The sides of the camera are enclosed by a 1 mm thick layer of a yet to be chosen opaque material. A view of a GRAIN camera is shown in Fig. 3.11.

The total LAr-filled volume is $\sim 9.1 \times 10^5$ cm^3, which the reconstruction algorithm divides in 1 cm^3 voxels. As the 3D direct reconstruction technique is prone to producing artefacts close to the camera, a fiducial region at a distance of 5 cm from the chamber sides is chosen, with the outer voxels being set to a 0 probability amplitude. This gives a fiducial volume of $\sim 4.9 \times 10^5$ cm^3.

Tab. 3.1 summarizes the main parameters of the GRAIN design used in the remainder of this dissertation.
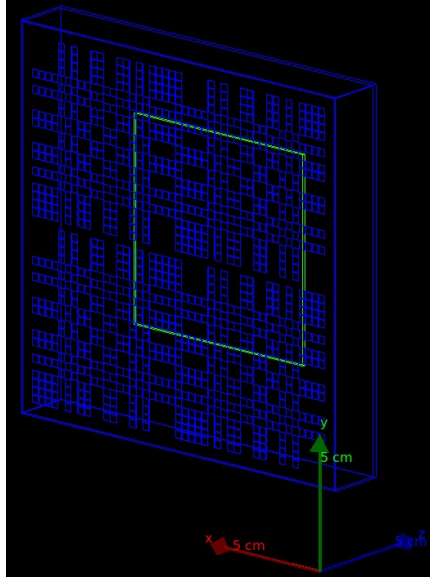
Fig. 3.11: Schematic view of a GRAIN camera, with the mask on the foreground and the SiPM array detector highlighted in the background in green.

GRAIN design parameters			
Cryostat dimensions		**Detector parameters**	
Width	130 cm	Pixels per side	32
Height	147.6 cm	Pixel edge	0.2 mm
Length	47.5 cm	Pixel size	3 mm
Total volume	0.91 m^3	Detector thick.	1 mm
Fiducial vol.	0.49 m^3	Detector side (d_d)	51.2 mm
Mask parameters		**Camera assembly parameters**	
Number of masks	76	b	20 mm
Elements per side	33	Camera body thick.	1 mm
Element size (p_m)	2.33 mm		
Element spacing	0.2 mm		
Mask size (d_m)	94 mm		
Mask thickness	0.1 mm		

Table 3.1: Summary of the relevant dimensions and parameters in the design of GRAIN that has been used for the analyses of this dissertation.

Chapter 4

Neutrino event reconstruction

The basic output of the 3D direct reconstruction technique, introduced in Section 3.2, is the prediction of the spatial distribution of the energy deposited by particles in the inner volume, which is then converted in scintillation light. In particular, for each voxel a score (or *probability amplitude*) is defined. This score represents the Bayesian probability of the voxel to be a source of the detected photons. Integrating subsequently over each detector and finally summing the amplitudes of all the cameras, one obtains the final amplitude-field for the event.

The basis of the algorithm is that a real light-source voxel would be reconstructed to have a high probability amplitude by cameras in different positions, resulting in a high value of the amplitude-field. This assumption must be verified by comparison with the spatial distribution of the true energy deposits from the simulation.

Once the correspondence between the 3D reconstruction and the Monte Carlo truth has been established, it will be possible to reconstruct the event, identifying vertices and particle tracks through Track Finding techniques. Doing so will require to discriminate the event signal from the significant combinatorial background produced by the 3D reconstruction algorithm.

This chapter will first analyse the amplitude distributions of the simulated neutrino events in GRAIN, determining their common features and issues. The need for performing amplitude cuts on the distributions will be argued consequently from the approximate point of view of image quality by using the Structural Similarity index to compare the reconstructions to the Monte Carlo distributions.

The analyses in the following have been performed using the Python programming language and its available libraries, which will be indicated when relevant.

4.1 The simulation chain

Before moving to the main subject of discussion, it is useful to outline the elements of the simulation chain that has been used to generate the events:

1. The neutrino events are generated by the *GENIE* neutrino Monte Carlo event generator [61] and subsequently passed through the *edep-sim* energy deposition simulation, which generates the corresponding distribution of the energy deposition in the GRAIN volume, not including the optical system cameras. The *edep-sim* simulation is a wrapper around Geant4 dedicated to the simulation of particle propagation and geometry [62].

2. In Geant4 [63], the optical readout cameras are added to the geometry. The scintillation emission is generated from the *edep-sim* output and its propagation is simulated in the final GRAIN geometry up to the hits on the SiPM cells.

3. The response of the SiPMs to the detected photons can be simulated thanks to a dedicated Detector Response program. This includes a modelling of the SiPM and electronics properties and of the DAQ system.

4. The 3D reconstruction algorithm is then applied to the output of the detector response. In the context of the SAND simulation chain, the reconstruction response is integrated with the simulation of the KLOE calorimeter.

The dataset that will be used in the following contains ν_μ events with all the typologies that will be possible for the future DUNE beam: nc events, Quasi Elastic cc events, Resonance production events and Deep Inelastic scatterings. The proportions of the different types are consistent with the prospects for DUNE.

4.2 Amplitude distributions of the simulated events

The final output of the 3D reconstruction algorithm was the probability amplitude for each of the $130 \times 146 \times 48$ voxels which compose the reconstruction volume. As mentioned in Section 3.3, a fiducial volume is defined at 5 cm from each side of the chamber to eliminate the reconstruction artefacts close to the cameras and to accomodate the overall parallelepipedal volume to the elliptical shape of the inner volume. The fiducial volume is thus of 4.9×10^5 cm^3.

   As the values of the probability amplitudes coming from the reconstruction algorithm are in arbitrary units, they were, when not specified otherwise, normalized between 0 and 1. This was done to transform the data in a range that is easier to manipulate and visualize. The resulting probability amplitude distribution for a generic event is shown
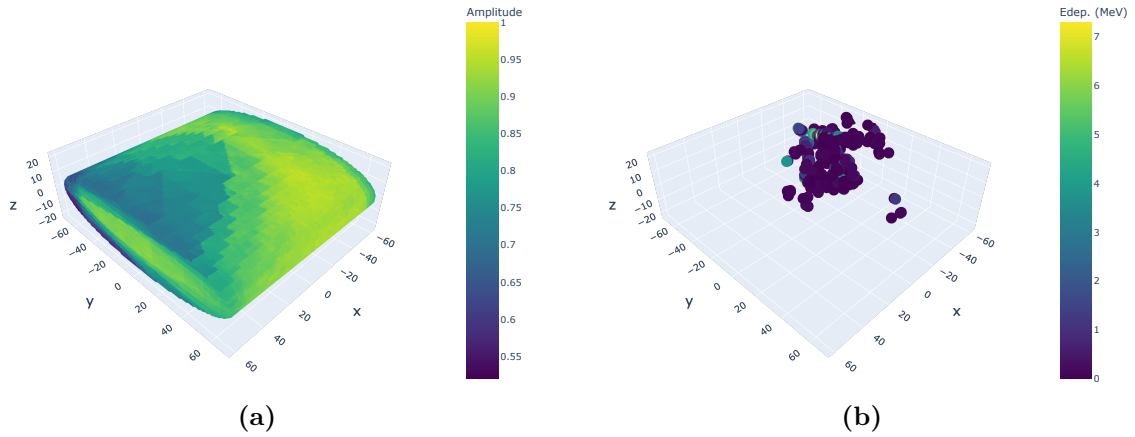
Fig. 4.1: (a) Probability amplitude distribution of an event with with voxels having $A > 0$. The origin of the axes is at the center of the image, consistently with the GRAIN simulation. (b) True spatial distribution of the energy deposits (in MeV) for the same event.
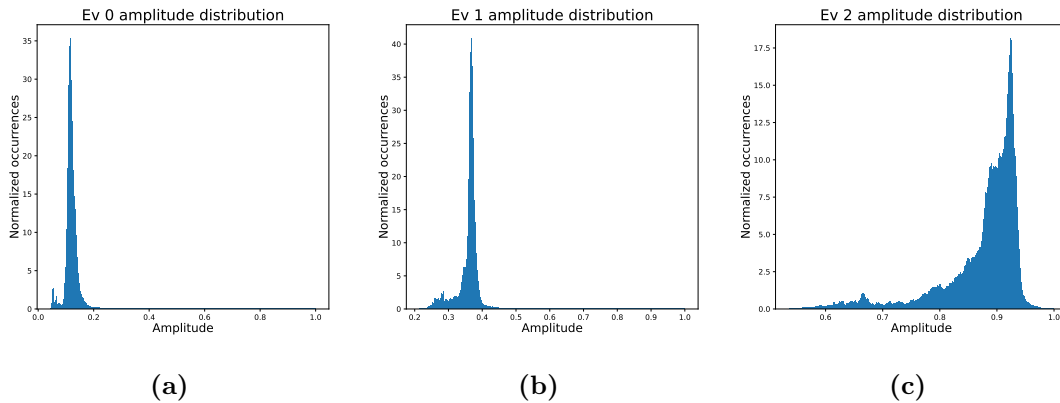
Fig. 4.2: Normalized spectrum of the amplitudes for three events. The significant variation in the peak position and the sharpness of the drop-off can be noticed.

in Fig. 4.7a for amplitudes $A(x, y, z) > 0$. The true spatial distribution of the energy deposits is show in Fig. 4.7b instead.

It is clear, from Fig. 4.7a, that the output of the 3D reconstruction algorithm features a significant background, as most of the voxels have a nonzero amplitude. It will be necessary, therefore, to devise a criterion for the discrimination of the reconstructed event from the combinatorial background. The need for such a criterion will be expanded upon in Section 4.3, in which a metric to validate it will be provided as well.

It has proved useful, for analysing the reconstructed events, to plot the distribution of occurrences of the probability amplitudes (or amplitude-spectrum): as the following will detail, such plots have been used to determine several important features of the event

reconstruction. Fig. 4.2 shows the amplitude-spectrum for a set of generic events.

The most significant hurdle to overcome for event reconstruction to be possible is due to the distribution of the combinatorial background: this corresponds to the large part of the amplitude spectrum, with the few signal voxels being close to the upper-end and without a corresponding distinguishing feature in the distribution. This situation is, in a sense, opposite to the typical one of a high signal peak with a lower background, and it is due to the reconstruction algorithm, which yields a fairly high probability amplitude for most of the voxels.

An additional complication that may occur is the presence of so-called *blind cameras*, cameras in which energy deposition, and thus light emission, has occurred in the space between the Coded Aperture mask and the detector. In such cases, the light emission, occurring inside the camera, does not project the usual mask pattern on the detector and it is wrongly reconstructed by the algorithm. This results in substantial artefacts with very high probability amplitudes distributed over a wide range of values.

The frequency of events having one or more blind cameras depends on the arrangement of the cameras along the sides of the detector: as the GRAIN design that is being considered in this work features the maximum number of cameras, most events will have at least a blind one. Blind cameras are, at the time of writing, identified from on the Monte Carlo truth of the energy deposit positions. Events where light emission occurs close to the cameras can also feature less significant reconstruction artefacts.

Having been identified, blind cameras can be excluded when summing to obtain the total amplitude distribution. Fig. 4.3 shows the amplitude spectra of two generic events with and without the contributions from the blind cameras: the reconstruction artefacts produced by blind cameras can significantly alter the distribution of the amplitude distributions.

To quantify the effect of blind cameras, two relevant features of the event spectra, with and without the blind cameras being cut, for a set of 369 events have been computed. These characteristics are the amplitude of the distribution maximum (the mode $Mo(A)$) and the Full Width at Half Maximum (FWHM) of the distribution peak. The distributions of the features for the dataset are shown in Fig. 4.4 with the blind camera excluded and included cases juxtaposed. It can be noticed how the inclusion of the blind cameras tends to shift the modes towards low amplitudes and increase the FWHM of the events.

The previous remarks on the characteristics of the reconstruction background allow to understand the effects of blind cameras on the modes of the amplitude spectra in Fig.4.4a. Blind cameras introduce artefacts with high reconstructed probabilities compared to the those resulting from correct reconstructions. This shifts the peak and thus the mode to lower fractions in the normalized amplitude range with respect to those of the valid spectra. Additionally, the very large width of the blind camera distributions increases the FWHM of the regular peak when the incorrect probabilities are added to the distribution, leading to the increase in Fig. 4.4b.
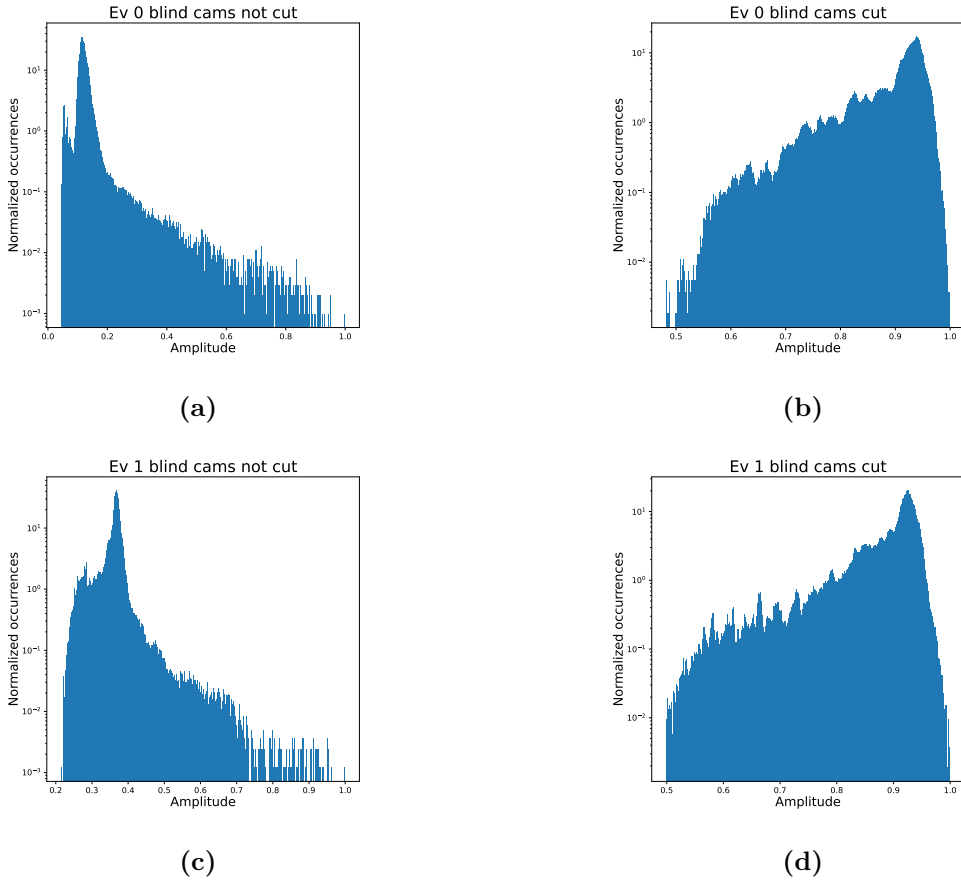
Fig. 4.3: Each row shows the amplitude spectrum of an event with the inclusion of blind cameras (left column) and without it (right column). A logarithmic scale on the occurrences axis has been chosen. The exclusion of the blind cameras modifies substantially the distribution.

The good consistency of the modes and FWHMs among the events in the dataset justifies their use as feature points in the analyses which follow. Indeed, since the single-camera distributions and subsequent total spectrum result from a combination of geometric and combinatorial factors, they cannot be easily modelled with standard distributions, and as a result, the mode and FWHM are the most robust features available to describe the position and width of the amplitude peak.
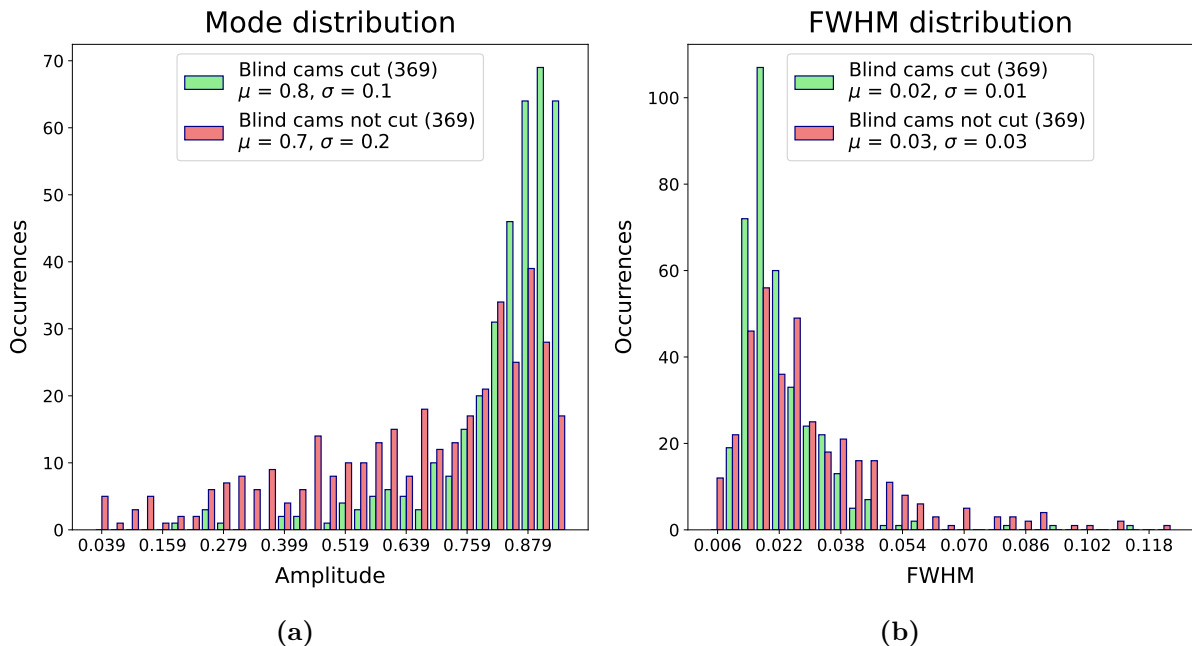
Fig. 4.4: The distribution of the amplitude spectrum modes (a) and of the FWHM (b) for a dataset of 369 events with (without) the inclusion of blind cameras is shown in red (green).

4.3 Structural Similarity index comparison

Having discussed the features of the spatial and amplitude distributions of the event reconstructions, it is necessary to determine whether they represent a reasonably accurate estimate of the spatial distribution of the energy deposits of the true events and to quantify the degree to which they are so.

The 3D reconstruction technique outputs a spatial distribution of probabilities starting from a certain amount of detected photons, so that a reconstructed event can be compared to the Monte Carlo truth by way of their image-wise similarity. This quality metric does not require track reconstruction and fitting, which are not applicable to this phase of event reconstruction

As a measure of the similarity of the reconstruction to the Monte Carlo truth, the *Structural Similarity Index* (SSIM) [64] of the two distributions can be used: this metric is adapted from the field of Image processing, where it is used to quantify the discrepancy between processed images and their originals in a way that takes into account the structural information. The application of the SSIM in the context of the event reconstruction in GRAIN has been suggested by the need for a measure of the similarity independent of any assumption on the physics of the event. The measure should also take into consideration both the amplitude values of single voxels and their positions relative to the others.

This section shall outline the principles and characteristics of the SSI metric before discussing its application to the reconstruction in GRAIN, discussing the results and limits of this method of comparison.

4.3.1   Introduction to the Structural Similarity index

The Structural Similarity index (SSIM) is one of the many *objective* image quality metrics that have been introduced over the years and that play a variety of roles in image processing applications by providing quantitative measures that can predict the perceived image quality. Natural image signals are highly structured, with pixels exhibiting strong dependencies, especially when they are spatially close, with said dependencies carrying important information about the structure of the objects in the scene [64]. The structural information in an image is independent from its luminance, i.e. the mean intensity. As such, the SSIM index aims at separating the two features through a similarity measurement divided in three comparisons: luminance, contrast and structure.

Assuming $\mathbf{x}$ and $\mathbf{y}$ to be the original and distorted image signals respectively, the first step in the index computation is the comparison of the luminance of each signal, estimated as their mean intensity. A luminance comparison function $l(\mathbf{x}, \mathbf{y})$ can be defined, as a function of μ_x and μ_y. For the second comparison, the standard deviation is used as an estimate of the signal contrast, defining the comparison function $c(\mathbf{x},\mathbf{y})$ of σ_x and σ_y. Finally, the signals are normalized by their own standard deviations, so that the structure comparison $s(\mathbf{x}, \mathbf{y})$ is conducted on the normalized signals.

The three aforementioned components are combined to yield an overall similarity measure

$$S(\mathbf{x}, \mathbf{y}) = f(l(\mathbf{x}, \mathbf{y})), c(\mathbf{x}, \mathbf{y})), s(\mathbf{x}, \mathbf{y}))), \tag{4.3.1}$$

where, importantly, the three components are relatively independent. For the definition of the similarity measure to be complete, the three functions and their combination f must now be defined under the following conditions:

1. Symmetry: $S(\mathbf{x}, \mathbf{y}) = S(\mathbf{y}, \mathbf{x})$;

2. Boundedness: $S \leqslant 1$;

3. Unique maximum: $S(\mathbf{x}, \mathbf{y}) = 1$ if and only if $\mathbf{x} = \mathbf{y}$.

A general expression of the index which satisfies the three conditions above is:

$$\text{SSIM}(\mathbf{x}, \mathbf{y}) = [l(\mathbf{x}, \mathbf{y})]^{\alpha} \cdot [c(\mathbf{x}, \mathbf{y})]^{\beta} \cdot [s(\mathbf{x}, \mathbf{y})]^{\gamma}, \tag{4.3.2}$$

where $\alpha, \beta, \gamma > 0$ are parameters that define the relative importance of the three components. Since image statistical features are typically highly non-stationary and image distortions, whether they depend on the local image statistics or not, may also be space-variant, it is useful to apply the SSIM index locally within a square window of a certain

width that is moved pixel-by-pixel over the entire image. At each step the local statistics and similarity index are computed, so that the overall quality measure of the image is given by the average over the M local windows:

$$\text{MSSIM}(\mathbf{X}, \mathbf{Y}) \equiv \frac{1}{M} \sum_{j=1}^{M} \text{SSIM}(\mathbf{x}_j, \mathbf{y}_j), \tag{4.3.3}$$

where $\mathbf{X}$ and $\mathbf{Y}$ are the reference and processed images respectively, while $\mathbf{x}_j$ and $\mathbf{y}_j$ are the contents of the j-th local window. Depending on the application, different weights can be applied to each local window [64].

It is instructive to show with 2D images how the SSIM index changes for transformations that may replicate the effects of the 3D direct reconstruction in GRAIN. In Fig. 4.5, four different transformations are applied to a reference *track-like* image and the resulting similarity indices are computed, assuming a 7×7 pixels local window:

1. A shift transformation in Fig. 4.5b, meant to replicate the effects of a coordinate bias of the reconstruction, which, as will be discussed in Section 5.1, is indeed present. The relatively high SSIM index of 0.92 is due to the preservation of the *track* structure and the high *inertia* of the background, which remains the same in both images.

2. A gaussian smoothing filter applied in Fig. 4.5c aiming to reproduce the finite resolution of the imaging system. This transformation too results in a relatively high similarity index.

3. The addition of a normally-distributed background noise to the image in Fig. 4.5d and to its smoothed version in Fig. 4.5e, corresponding to the high combinatorial background of the reconstructions. The SSIM index falls to low values as the background, which makes up the majority of the pixels, has different values compared to the reference image.

The SSIM computation is performed with the pre-defined function in the *Scikit-Image* Python library [65], which, most importantly, offers the generalization to n-dimensional images which will be used in the following.

Fig. 4.5 illustrates the main hurdle in using of the SSIM index in physics detectors: the absence of a distinction between background and signal, which, while unnecessary for regular imaging applications, is crucial for event reconstruction. Since the relevant signal pixels are a small fraction of the total, the SSIM index mostly depends on the similarity of the background.

4.3.2 Application in GRAIN

From the previous discussion on the effects of a change of background on the SSIM index, and referring to Fig. 4.1 it becomes clear how the SSIM index cannot be applied

(a)

(b)

(c)

(d)

(e)
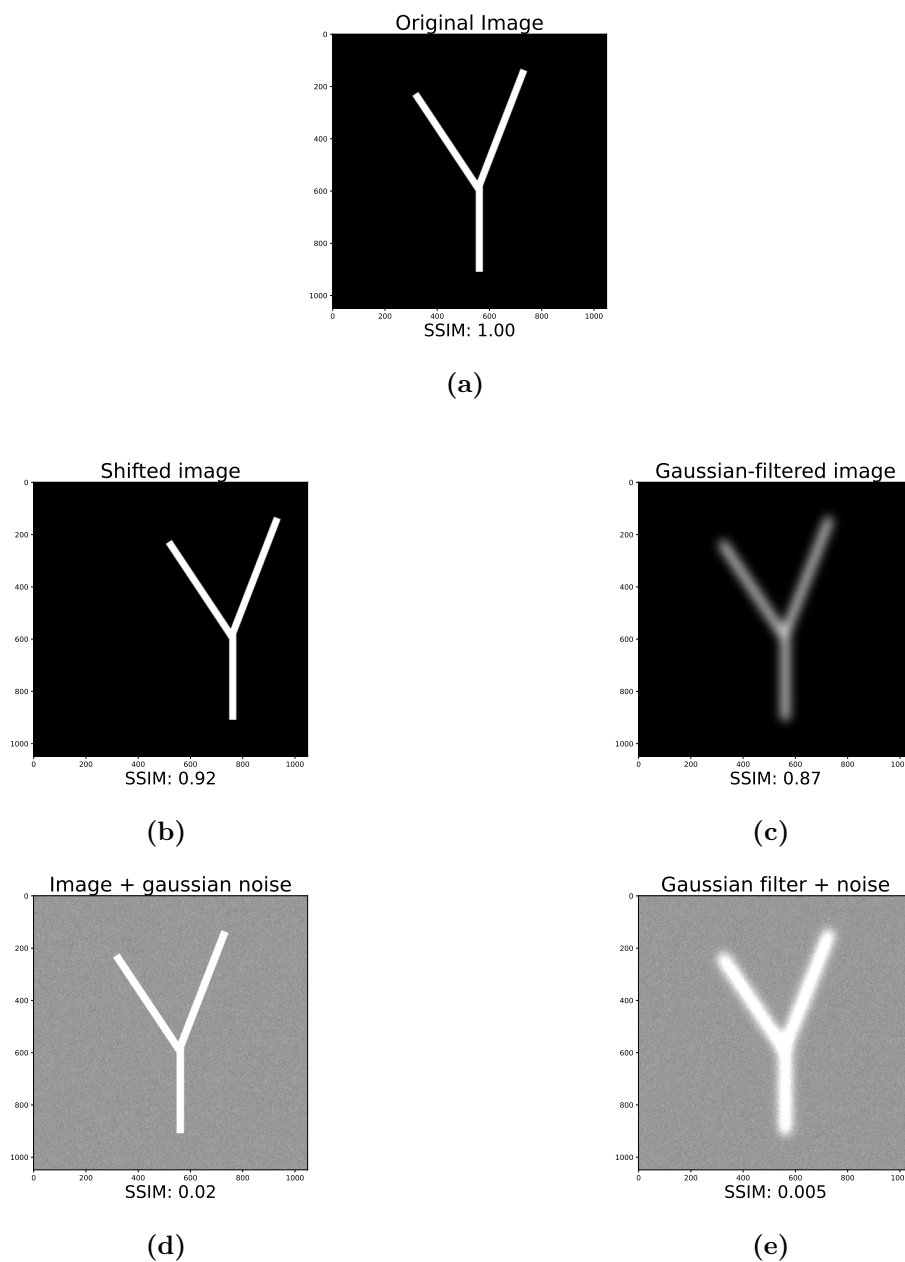
Fig. 4.5: (a) shows the track-like reference image. The shifted image in (b) results in a SSIM index of 0.92. The smoothed image in (c) gives a similarity index of 0.87. In (d) and (e), the addition of a high value (mean = 0.7) normally-distributed background reduces significantly the SSIM index.

directly to the output of the 3D reconstruction technique: its background voxels have amplitudes $A > 0$ with a peak at high amplitudes close to the signal values, while the

true energy deposition distribution has a nonzero value only at the voxels where light has been emitted. Since the SSIM does not implement a distinction between the signal and background of the image, the index for the aforementioned comparisons between reconstruction and Monte Carlo truths would be dominated by the non-similar backgrounds, as such voxels take up most of the volume. The resulting comparisons would be equivalent to those in Fig. 4.5d and 4.5e, having a very low similarity index.

For the SSIM to give meaningful results it is therefore necessary to perform amplitude cuts on the reconstructed events, defining a threshold amplitude above which the voxels can be assumed to be light sources. Such a procedure intuitively increases the similarity between the images and the SSIM index should improve accordingly. Defining such a criterion is not trivial, as the amplitude distributions do not present specific features that distinguish the signal voxels from the background.

In the absence of an analytical model for the amplitude distributions the two robust features that can be utilised to analyse the tail-end of the spectrum are the mode and FWHM of the peak: in Section 4.2 it was shown how, upon exclusion of the blind cameras, the values of these two features are consistent between the events, justifying their use as scales for the tail of the amplitude peak.

In order to quantify the optimal amplitude cut, or interval thereof, in terms of the structural similarity, the tail-end of the distribution can be scanned by multiples of the FWHM, at which the SSIM index between the reconstructions and the Monte Carlo truths can be evaluated. A preliminary check of the validity of the SSIM comparisons must be performed by computing, for each reconstruction, the similarity index with all the true energy distributions: this should have the highest value for the corresponding Monte Carlo truth. If the index can reliably match the corresponding distributions for a value of the cut, this might provide a valid threshold between the signal and background voxels.

For the sake of performing this preliminary assessment of the validity of the reconstruction, it has proved useful to reduce the spatial resolution of the reconstruction and Monte Carlo truth distributions by summing the amplitudes of adjacent voxels. This *rebinning* procedure increases the ratio of signal to background voxels since the signal is concentrated in a limited volume, enabling to reduce the impact of the background on the SSIM index. A number of potential combinations of reduced dimensions have been considered, finally choosing a $21 \times 24 \times 12$ voxels volume, as it led to the best comparison results. Fig. 4.6 shows the resulting spatial distribution heatmaps of the reconstruction and Monte Carlo truth: it can be noticed in Fig. 4.7a how the *rebinning* algorithm may discard some of the boundary voxels, since the original dimensions are not exact multiples of the final ones. The effect of the resulting asymmetries was deemed to be negligible for the computation of the SSIM index.

After the rebinning of both spatial distributions, the amplitude cuts were applied to the reconstruction. Fifteen cut thresholds were considered, starting from the mode of the event amplitude distribution and reaching $\mathrm{Mo}(A) + 1.4 \cdot \mathrm{FWHM}$ with 0.1 wide

| (a) | (b) |
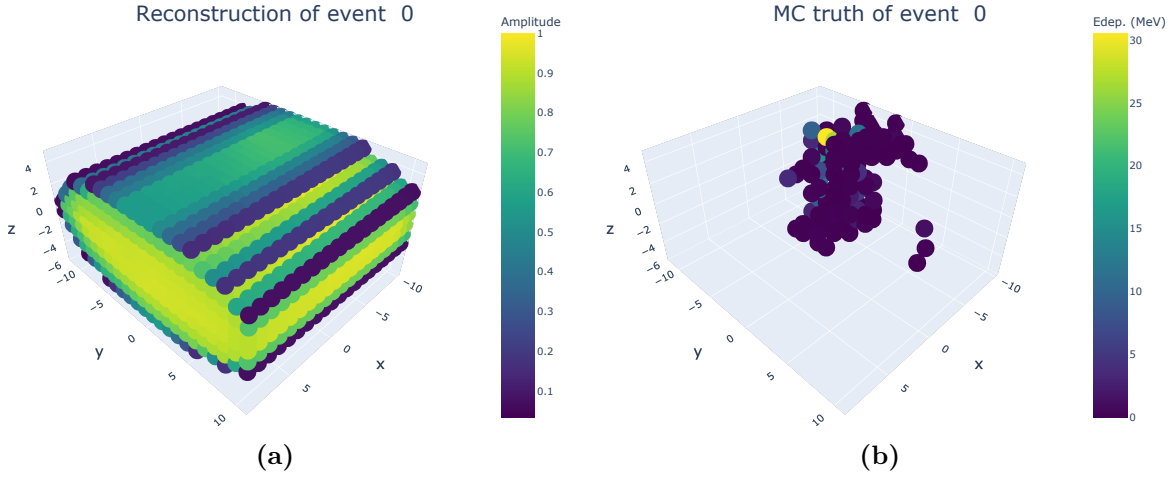
Fig. 4.6: Spatial amplitude distribution of a reconstruction in (a), and of the true Monte Carlo energy deposits in (b), after the *rebinning* procedure. In (a) an asymmetry of the distribution due to the *rebinning* is noticeable at the positive-y boundary.

intervals. The SSIM indices of all available pairs of reconstructed and true distributions in a subset of 97 events were computed using the *Scikit-Image* function and plotted as a 2D image: if the structural similarity measure were to be valid, the highest values of the index would be on the diagonal, corresponding to the correct matching of reconstruction and true distributions.

The similarity indices were found to vary significantly between reconstructed events, making the diagonal pattern difficult to discern. The closeness of the SSIM indices for all comparisons of a given reconstruction can be explained referring to the previous section: as the majority of voxels, once the cut has been applied, have a shared value of $A = 0$ for both the reconstruction and all Monte Carlo distributions, the similarity indices will have a minimum nonzero value that depends on the reconstructed event. An equivalent behaviour for the Monte Carlo distributions was also observed, featuring, although, less pronounced variations.

To obviate to the issue above, the mean SSIM index for each reconstruction was subtracted to the corresponding row and was subsequently used to normalize the resulting residues: this has allowed to cancel the similarity index baselines and highlight the higher indices along the diagonal. In Fig. 4.7 the residual indices for the lowest ($Mo(A)$) and highest ($Mo(A)+1.4 \cdot FWHM$) amplitude thresholds are plotted: for both cuts, a diagonal structure with higher indices with respect to the surrounding can be noticed, due to the higher SSIM index that is correctly assigned to matching pairs of reconstruction and true distribution. The diagonal is more sharply visible in the highest cut plot, which, after the normalization, appears more uniform row-wise. This enables, conversely, to notice the difference in the similarity baselines for each Monte Carlo distribution.
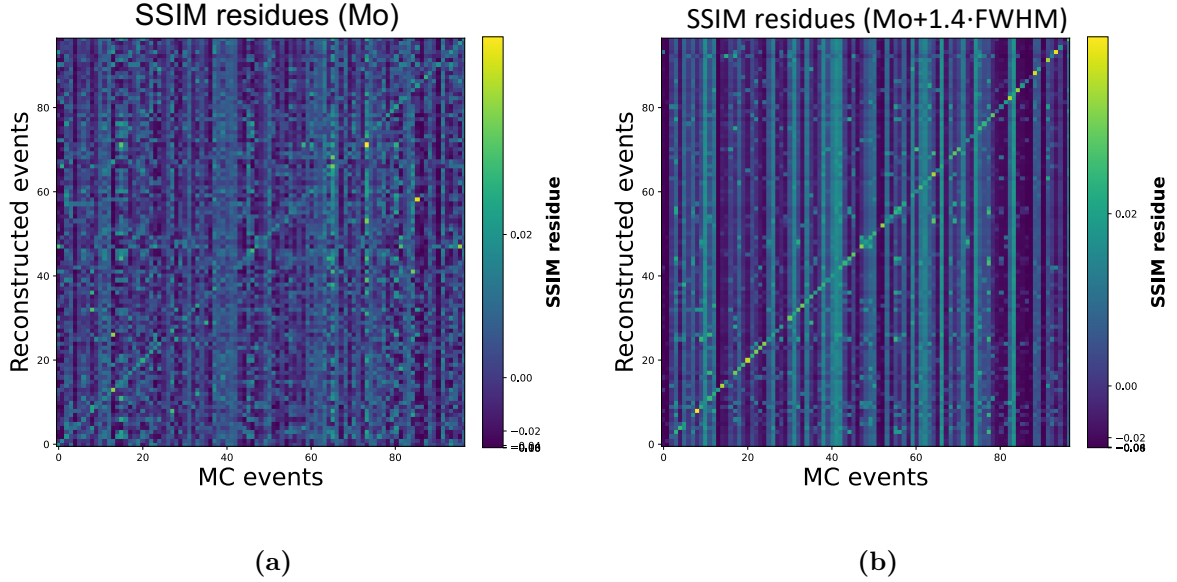
Fig. 4.7: Normalized SSIM index residues for 97×97 pairs of events in the dataset assuming an amplitude cut at $\mathrm{Mo}(A)$ in (a) and at $\mathrm{Mo}(A) + 1.4 \cdot \mathrm{FWHM}$. An exponential colorscale has been chosen to highlight the differences between the higher indices. At the higher cut the index distributions for each reconstructions are more uniform, with the diagonal indices standing out more sharply.

In order to quantify the separation of the similarity indices of matching pairs over those of non-corresponding combinations, the ratio between the mean of the indices along the diagonal and the mean of the non diagonal indices was computed for all the considered amplitude cuts. In Fig. 4.8a the plot of such ratios is shown: a clear maximum in the ratio is reached for a threshold value of $\mathrm{Mo}(A) + 0.8 \cdot \mathrm{FWHM}$, although the variation is not particularly pronounced over the cut range. It can be noted, furthermore, how the ratios have values ~ 1, consistently with the fact that all pairs have a nonzero baseline SSIM index, with the correct matches having only slightly higher values.

As a final measure of the validity of the amplitude cuts, the fractions of correct matches between reconstructions and true Monte Carlo distributions were computed for the chosen thresholds and are plotted in Fig. 4.8b: the percentages initially grow with the amplitude cuts, reaching $\sim 65\%$ at $\mathrm{Mo}(A) + \mathrm{FWHM}$. The subsequent slight decrease may be explained as due to a sufficiently high amount of voxels having been cut for the structural similarity to worsen. Such a behaviour may also be linked to the lowering of the diagonal to off-diagonal means ratios for cuts past $\mathrm{Mo}(A) + 0.8 \cdot \mathrm{FWHM}$ shown in Fig. 4.8a. The increase of both the similarity measures above with the amplitude cuts shows, from the point of view of image similarity, the need for applying such thresholds, as the elimination of the background leaves out the voxels corresponding to a true emission
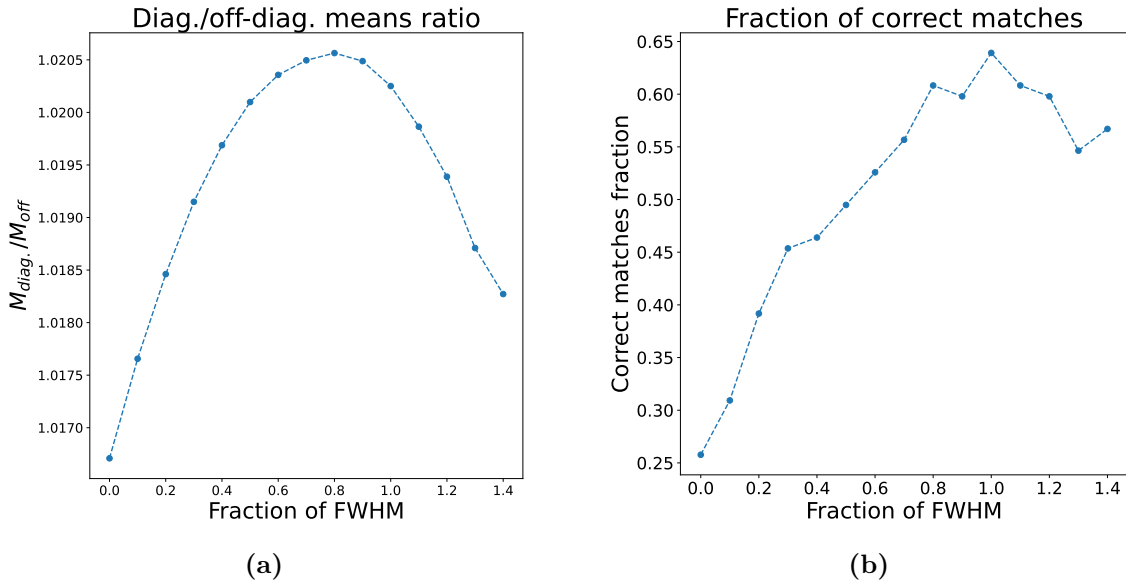
Fig. 4.8: (a) Ratios of the diagonal over the off diagonal means M for the considered amplitude cuts. (b) Fractions of correctly matched reconstructions for the chosen amplitude thresholds. The percentages grow, initially, with the amplitude cuts, reaching $\sim 65\%$ at $\mathrm{Mo}(A) + \mathrm{FWHM}$. The scale for the x-axes is given by the fractions f of FWHM of a given $\mathrm{Mo}(A) + f \cdot \mathrm{FWHM}$ cut.

The limited accuracy in the matching of corresponding reconstructions and Monte Carlo truths can be ascribed to the presence, in the dataset, of events with similar true distributions, as the interaction topologies in the simulation are limited and the *rebinning* reduces the distinguishing features of the distributions. This is indeed shown in Fig. 4.9, where the Monte Carlo distributions are compared against each other: the off-diagonal indices have relatively high values, with a ratio of the diagonal to off-diagonal means $M_{diag}/M_{off} = 1.04$, just slightly higher than the maximum one in Fig. 4.8a.

4.4 Preliminary observations

The first analyses described in this chapter were aimed at gaining and understanding of the 3D direct reconstructions, determining their features and the issues that may be present:

- The presence of a dominant combinatorial background close to the *signal*-voxel amplitudes produced by the algorithm was assessed, justifying qualitatively the need for applying amplitude cuts when performing track reconstruction.

- The effects of *blind-cameras* on the reconstructions were determined: the emission
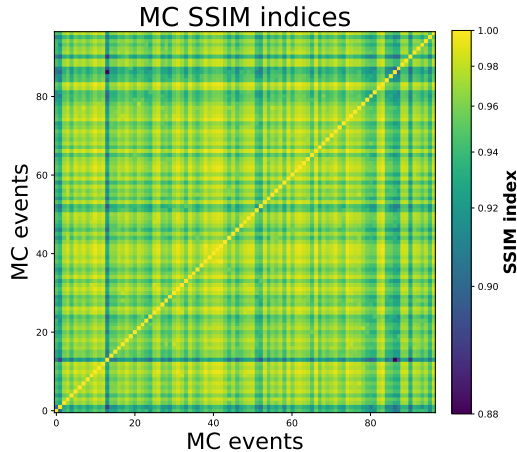
Fig. 4.9: SSIM comparisons of the Monte Carlo distributions against each other: the ratio $M_{diag}/M_{off} = 1.04$ corresponds to a mean background index of 0.96, significantly close to the maximum index of 1.

of scintillation light inside the cameras led to the reconstruction of voxels with unnaturally high probability amplitudes distributed over a much wider range of values with respect to the standard behaviour.

- The features of the probability amplitude distributions were analysed, determining that the amplitude mode $Mo(A)$ and FWHM are consistent between all reconstructions, once blind cameras have been excluded, and can therefore be used to set a scale with which to define the amplitude cuts. It proved impossible to exactly model the amplitude spectrum as a known distribution, justifying the choice of $Mo(A)$ and FWHM as features.

The Structural Similarity Index was used, in the second phase, to evaluate the image-wise similarity between the reconstructions and the Monte Carlo truth distributions. The application of amplitude cuts was justified, in this case, by the need for similar backgrounds for the distributions to be compared. This is in accordance with the higher perceived similarity of the reconstruction to the true energy deposition once the combinatorial background has been cut.

The computation of the SSIM index of all pairs of events for a range of amplitude cut values showed that despite the presence of structures in the similarity plots due to the features of both reconstructed and Monte Carlo distributions, the indices of true matching pairs were generally higher than those of the false matches. The mean amplitude ratio between the two subsets furthermore grew with the cut, reaching a maximum at

Mo(A) + 0.8·FWHM before decreasing again. The percentage of correctly matched reconstructions was correspondingly found to increase with the cuts, reaching a maximum of $\sim 65\%$ for a Mo(A)+FWHM threshold before decreasing slightly.

Overall, the comparison of the spatial distributions has not proved decisive, as the relatively low M_{diag}/M_{off} and correct matches fractions have shown. Thus, despite the algorithm still being in an early of a phase for track fitting, it was decided to extract some basic event features from the reconstructions. Such features could be compared to the true distribution to provide a quality measure of the reconstruction. The results of this analysis is discussed in the next chapter.

Chapter 5

Feature extraction of neutrino events

The analysis in the previous chapter focused on the characteristics of the GRAIN imaging technique that did not depend on the physical observables of the events: the common features of the reconstruction distributions and the issue of the combinatorial background and blind cameras could be investigated without any assumption or assessment on the event type and physics. In the same way, the Structural Similarity index allowed a quantification of the correspondence between reconstructions and true energy deposition distributions that did not depend on physical observables such as particle momenta, vertex positions and track lengths. These preliminary procedures have, nonetheless, confirmed what was assumed to be a key necessity for the eventual extraction of observables from the event reconstructions: the application of amplitude cuts.

As a final step in this thesis work, the basic features of the events will be estimated from the 3D reconstructions. The validity of the estimators will first be argued considering the possible event topologies and the known limitations with the reconstruction technique. The extracted features will then be compared to the true physical observables for a range of amplitude cuts in order to evaluate the discriminating aspects for the quality of the reconstruction technique. Specifically, it will be determined whether the amplitude cuts have a positive effect on the estimate of features from the reconstruction, which is the extent of such effect and, finally, if an amplitude threshold value or an interval of them can be found that guarantees a high accuracy of the estimates of the event observables from the reconstruction features. The features that will be extracted from the reconstructions are aimed at estimating the vertex position, the length and direction of tracks ad the cumulative energy deposition in the detector volume.

5.1 Vertex position

The measurement of the position of the event vertices is crucial for the GRAIN physics program. This hinges on the possibility of discriminating interactions occurring inside its fiducial volume to study the νAr interaction cross-section. It is therefore necessary to determine an estimator of such a structure which has sufficiently high accuracy and efficiency.

An first choice for the estimator of the event vertex position is the *centroid* of the reconstructed distribution, given by the mean of the voxel positions $\vec{x}_i$ weighted by their amplitude $A(\vec{x}_i)$:

$$\text{Cen}(\vec{x}) = \frac{\sum_{i=0}^{N_{vox}} A(\vec{x}_i) \cdot \vec{x}_i}{\sum_{i=0}^{N_{vox}} A(\vec{x}_i)} \tag{5.1.1}$$

Indeed, for a significant fraction of the events, which will be assessed in the following subsection, the highest energy deposition will occur at the vertex, so that the reconstructed probabilities can be expected to have the highest values at the corresponding position. In light of the high amplitude of the combinatorial background, the accuracy of the centroid estimate of the vertex should increase with the amplitude threshold which is set for the distribution: in order to confirm this, the quality of the estimate will need to be evaluated for a range of cuts.

5.1.1 Validity of the centroid estimator

Before evaluating the quality of the estimate of the vertex position from the centroid of the amplitude distribution, it is necessary to determine the degree to which such a quantity is actually meaningful. In fact, the true quantity that the centroid of the amplitude distribution estimates is the centroid of the Monte Carlo energy deposition (E_{dep}) distribution, since the 3D reconstruction algorithm depends on the light emission. It is necessary, therefore, to compare the centroid of the E_{dep} distribution to the true position of the event vertex, verifying whether the two positions match and determine the origin of potential outliers.

The distances between the Monte Carlo E_{dep} centroids and the corresponding true event vertices have been computed for the events in the dataset having true vertices within the fiducial volume: as shown in Fig. 5.1, the distribution is peaked at the minimum distance of 0.38 cm and drops off sharply at distances above ~ 25 cm. A check of the Monte Carlo information on the events showed how events with distances below ~ 10 cm mostly featured emission concentrated at the vertex or short tracks, with larger deviations corresponding to progressively longer charged particle tracks or to the diffuse emission due to the interactions of γs. For the latter event types, significant distances of the centroid from the vertex are to be expected, since:

- the centroid of the E_{dep} for tracks will be roughly at the middle point between the extremities, one of which will be close to the vertex;

- the pair production from γs gives rise to events with a sparse E_{dep} distribution, with most voxels not being connected to any clear vertex.
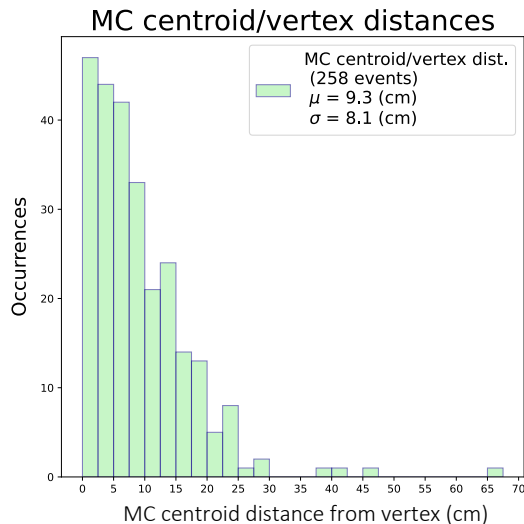
Fig. 5.1: Distances of the centroids of the Monte Carlo E_{dep} distributions from the true vertex position. Only events having vertices inside the fiducial volume are included. The bin width is of 2.5 cm.

The distribution of the distances between the E_{dep} centroid and the true vertex reaching its peak at the minimum of the interval (with 66% percent of the events having distance $\lesssim 10$ cm). The higher deviations are instead ascribable to charged particle tracks and sparse emission. This assessment justifies the use of the Monte Carlo E_{dep} centroid as an estimate for the vertex, as it is consistent with the latter once event topology is taken into consideration.

5.1.2 Comparison between reconstructed and true position

Having verified the validity of the Monte Carlo E_{dep} centroid as an estimator of the vertex position, the former can be compared to the centroid of the reconstructed amplitude distributions to test the capabilities of the 3D reconstruction algorithm. As the emission of scintillation light corresponds to energy deposition of charged particles, the positions of the two centroids can be expected to be consistent. The application of progressively higher amplitude cuts should furthermore lead to a decrease of the mean value of the deviations, as a larger fraction of the combinatorial background is eliminated.

94

The histogram of the distances between reconstruction and Monte Carlo centroids for amplitude cuts between $\mathrm{Mo}(A)$ and $\mathrm{Mo}(A) + 4 \cdot \mathrm{FWHM}$ is shown in Fig. 5.2: for the largest fraction of the events, the deviation from the centroid position decreases with the amplitude threshold, while the smaller subset with slightly increasing distances was determined to be composed of remaining badly reconstructed events, the centroid of which, as more voxels are cut, might be computed as further away from the true one, depending on the structure of the artefacts.
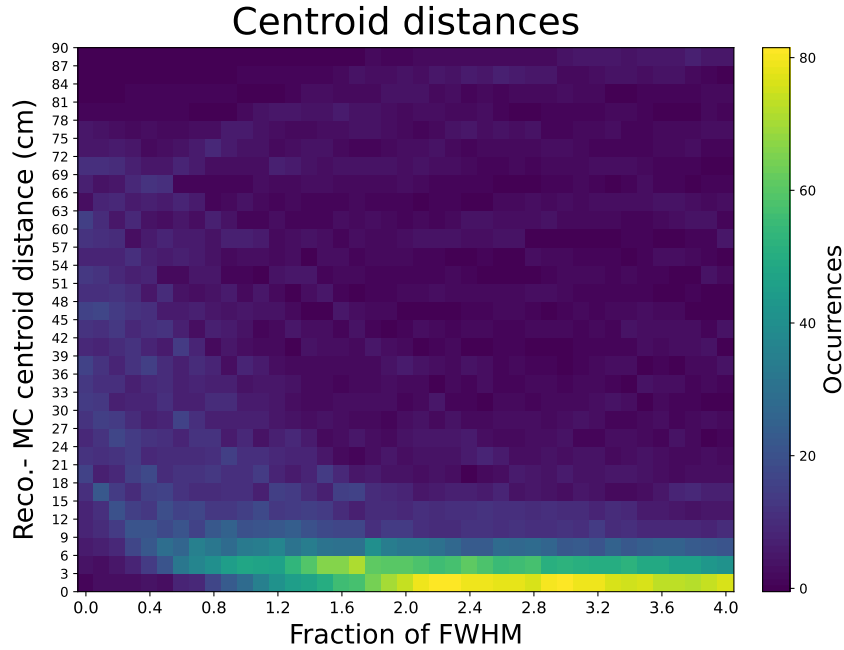
Fig. 5.2: Distribution of the distances between the reconstruction and Monte Carlo E_{dep} centroids for cut values between $\mathrm{Mo}(A)$ and $\mathrm{Mo}(A) + 4 \cdot \mathrm{FWHM}$. The maximum number of events in the minimum distance bin is for the $\mathrm{Mo}(A) + 2.3 \cdot \mathrm{FWHM}$ cut. The sparse events with high deviations were assessed to contain artefacts. At cuts above $\mathrm{Mo}(A) + 1.7 \cdot \mathrm{FWHM}$ progressively more events are excluded as the cuts eliminate all voxels.

The mean of the distances decreases sharply, reaching a minimum of 16 cm for a cut threshold of $\mathrm{Mo}(A) + 2.4 \cdot \mathrm{FWHM}$ before returning to a slight rise as Fig. 5.4a shows. The histogram of the distances at the $\mathrm{Mo}(A) + 2.4 \cdot \mathrm{FWHM}$ cut, corresponding to the minimum mean, is shown in Fig. 5.4b: for the largest part of the events (72%) the distances remain below ~ 15 cm, with the outliers with larger deviations being badly reconstructed events that still feature significant reconstruction artefacts. Fig. 5.3 shows an example of the distribution of a badly reconstructed event and of a low deviation one at the $\mathrm{Mo}(A) + 2.4 \cdot \mathrm{FWHM}$ cut.

In order to understand the behaviour of the reconstruction centroid estimate it also proved useful to plot, for each cut, the number of events in two subsets defined by their
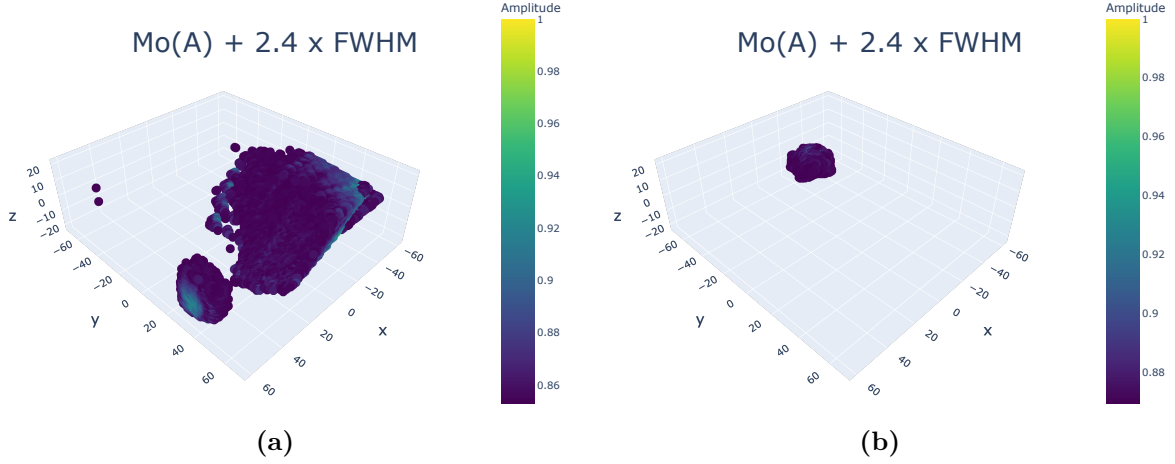
Fig. 5.3: (a) Amplitude cut of $Mo(A) + 2.4 \cdot FWHM$ for a badly reconstructed event, showing significant artefacts. (b) Amplitude cut of $Mo(A) + 2.4 \cdot FWHM$ for a low deviation event.
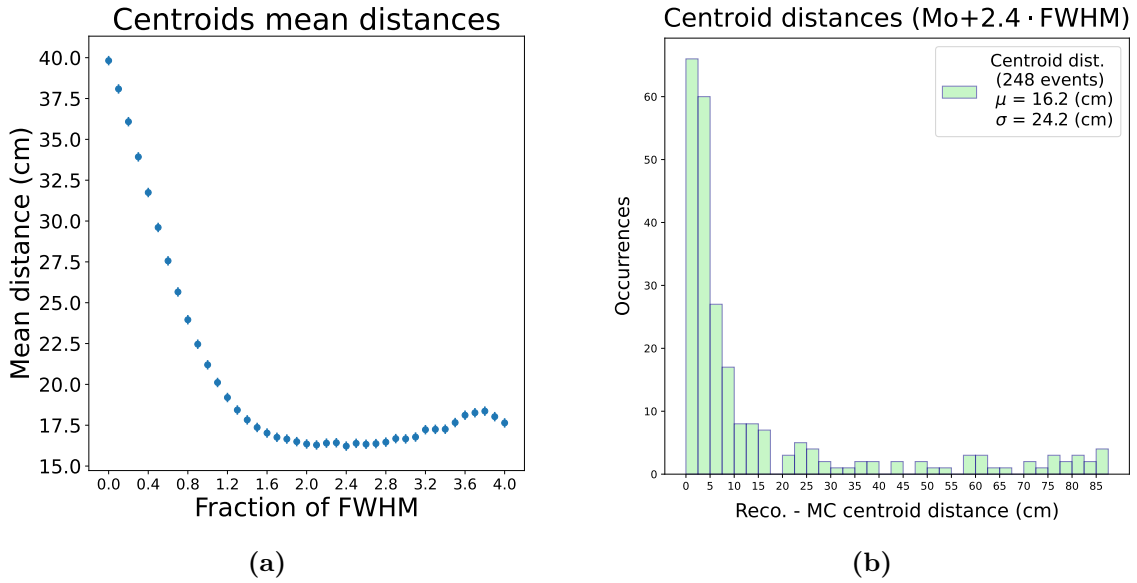
Fig. 5.4: (a) Mean of the centroid distances for the range of cuts that has been considered. The slight rise in the mean values at higher cuts is due to the reduction of events with distances $\lesssim 30$ cm, as not all survive the selection cut. The uncertainty associated to the mean distance has been estimated as $1/\sqrt{12} \simeq 0.3$ cm. (b) Histogram of the centroid distances for the cut at $Mo(A) + 2.4 \cdot FWHM$, with the minimum mean distance. Events with deviations above 15 cm are found to contain artefacts.

deviations:

1. Events with deviations $d_{cen} < 15$ cm, which when checked, were determined to be almost free of artefacts at the given cut.

2. Events with $d_{cen} \geq 15$ cm, which, upon inspection were found to contain residual background and artefacts of varying size and amplitude for the given cut.

The effects of the progressive amplitude cuts, as shown in Fig. 5.6a, were the initial rise of the events with $d_{cen} < 15$ cm, which overcomes the other subset at a cut of $\sim \mathrm{Mo}(A) + 0.9 \cdot \mathrm{FWHM}$. To decouple the effects of the cuts from the total event number, the fractions of the remaining events at a given amplitude cut are plotted in Fig. 5.5b. The percentage of events having $d_{cen} < 15$ cm stabilizes after the $\sim \mathrm{Mo}(A) + 2 \cdot \mathrm{FWHM}$ cut, reaching a maximum of 76% at $\mathrm{Mo}(A) + 2.7 \cdot \mathrm{FWHM}$. The plot in Fig. 5.5b defines, furthermore, a minimum viable amplitude cut of $\sim \mathrm{Mo}(A) + 0.9 \cdot \mathrm{FWHM}$, at which point the fraction of $d_{cen} < 15$ cm events overcomes that of the other subset.

(a)   (b)
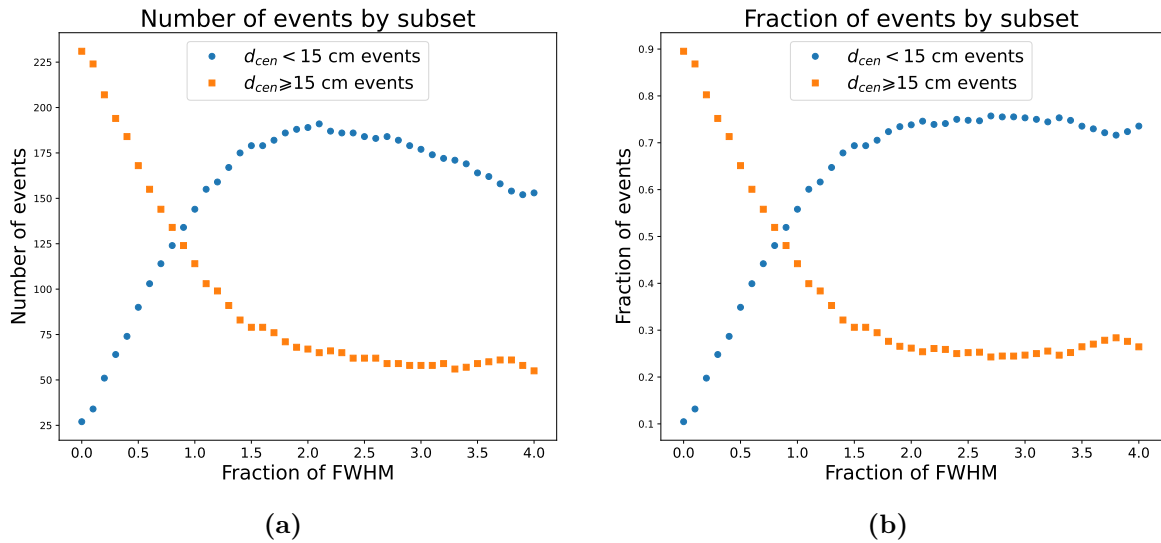
Fig. 5.5: Total number (a) and fraction (b) of events with reconstructed centroid position distance $d_{cen} < 15$ cm (blue) or $d_{cen} \geq 15$ cm (orange) from the true centroid position as a function of the cut.

In order to define the optimal range of amplitude cuts, the accuracy of the estimates had to be determined for the subset of correctly reconstructed events. The mean centroid distances for the $d_{cen} < 15$ are plotted in Fig. 5.6: after $\sim \mathrm{Mo}(A) + 2 \cdot \mathrm{FWHM}$, the means reach a stable value of ~ 4.5 cm. The optimal interval of amplitude cuts, from the point of view of the centroids deviations, is determined to be between $\mathrm{Mo}(A) + 2 \cdot \mathrm{FWHM}$ and $2.4 \cdot \mathrm{FWHM}$ as it corresponds to the maximum fractions of events with minimum

97

deviations, and therefore to the lowest mean distance, while maintaining a sufficiently high reconstruction efficiency ($\gtrsim 95\%$) as shown in Fig. 5.6b. Furthermore, the mean distances of the correctly reconstructed events reach a stable minimum value of ~ 4.5 cm.

Overall, the use of the reconstruction centroid as an estimator of Monte Carlo centroid is deemed to be substantiated, as the majority of events is found within 15 cm of the true position for a consistent range of amplitude cuts and the origin of the outliers has been determined.
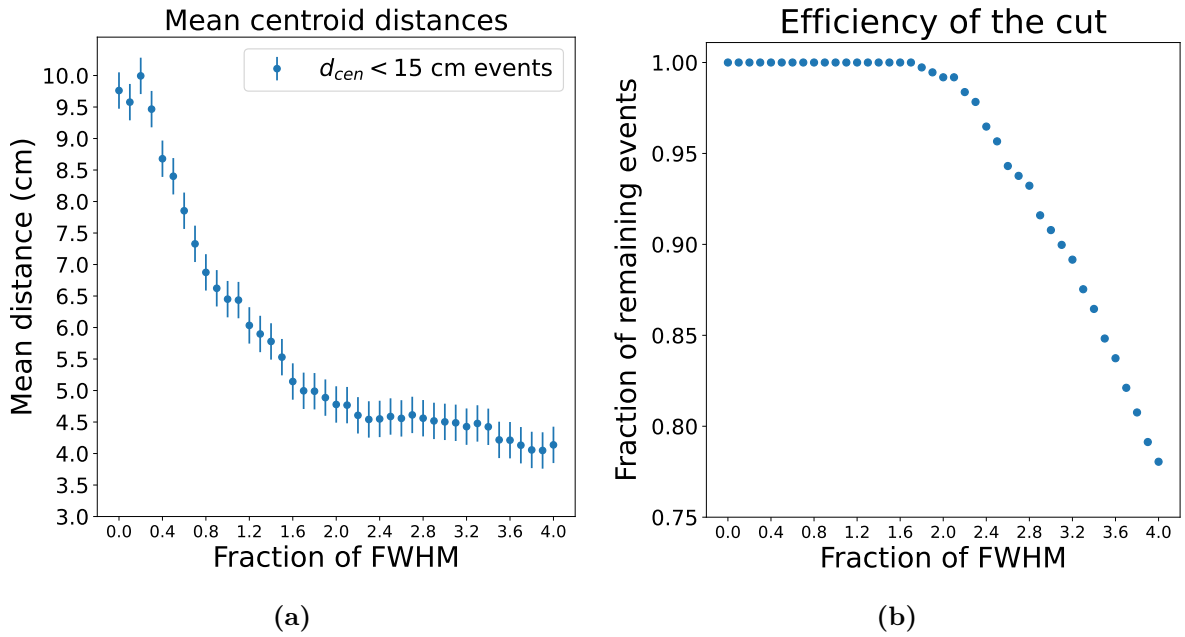
Fig. 5.6: (a) Mean centroid distances for the $d_{cen} < 15$ cm event subset: after $\sim \mathrm{Mo}(A) + 2 \cdot$ FWHM, the means reach a stable value of ~ 4.5 cm. The uncertainty associated to the mean distance has been estimated as $1/\sqrt{12} \simeq 0.3$ cm. (b) Efficiency of the amplitude cuts for the centroid analysis, computed as the fraction of remaining events compared to the initial number of 258.

5.1.3 Comparison between the reconstructed centroid and the true vertex position

Having shown its consistency with the Monte Carlo E_{dep} centroid, the centroid of the 3D reconstruction can be tested against the true vertex position of the event. A worse performance can be expected, since, as discussed above, the reconstruction will depend directly on the E_{dep} spatial distribution, which was shown in Section 5.1.1 to feature non-negligible deviations from the vertex position.

The 2D histogram of the distances d_{vert} between the reconstruction centroid and the true vertex for the amplitude cuts between $\mathrm{Mo}(A)$ and $\mathrm{Mo}(A) + 4 \cdot \mathrm{FWHM}$ is shown in Fig. 5.7: as with the E_{dep} centroid, the deviation decreases with the amplitude cut for the majority of events, with the smaller subset having increasing large distances being determined to consist of badly reconstructed events. For these, the most intense voxels are indeed unrelated to the true vertex position.
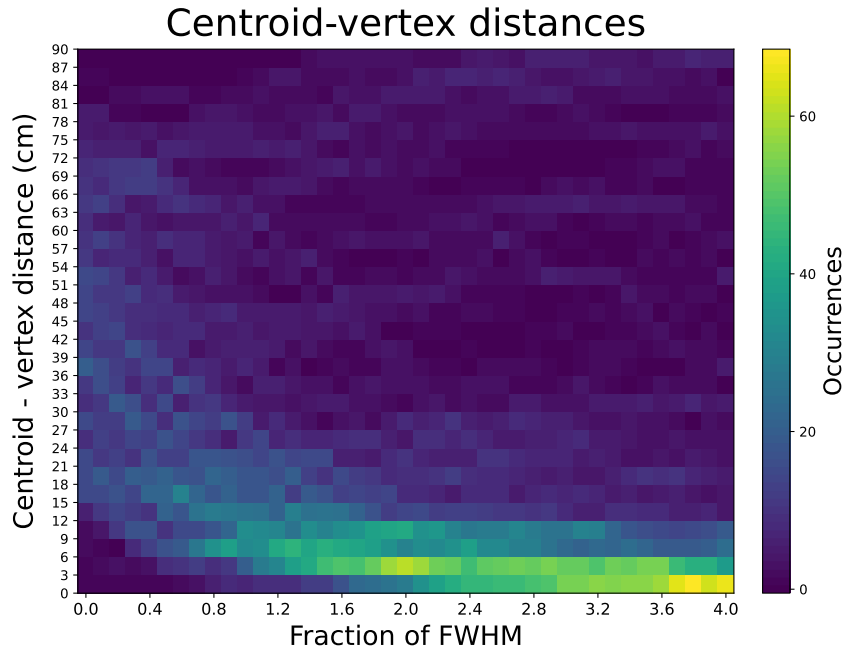
Fig. 5.7: Distribution of the distances between the reconstruction centroids and Monte Carlo vertices for cut values between $\mathrm{Mo}(A)$ and $\mathrm{Mo}(A) + 4 \cdot \mathrm{FWHM}$. The maximum number of events in the minimum distance bin is for the $\mathrm{Mo}(A) + 3.6 \cdot \mathrm{FWHM}$ cut. The sparse events with high deviations were assessed to contain artefacts. At cuts above $\mathrm{Mo}(A) + 1.7 \cdot \mathrm{FWHM}$ progressively more events are excluded as the cuts eliminate all voxels.

The mean of the distances was computed for all amplitude cuts and is shown in Fig. 5.8a. The minimum value of ~ 19 cm is is reached for a threshold of $\mathrm{Mo}(A) + 2.6 \cdot \mathrm{FWHM}$.

The number of events and the relative fractions of the two distance subsets used in the comparison of the centroids were computed to understand the behaviour of the reconstruction estimate. The number of events at $d_{vert} < 15$ cm and $d_{vert} \geqslant 15$ cm is shown in Fig. 5.9a: the smallest-deviation subset overtakes the other at a cut of $\sim \mathrm{Mo}(A) + 1.2 \cdot \mathrm{FWHM}$, higher than the corresponding cut for the centroid comparison ($\sim \mathrm{Mo}(A) + 0.9 \cdot \mathrm{FWHM}$), and reaches a maximum for the cut at $\mathrm{Mo}(A) + 2 \cdot \mathrm{FWHM}$ before decreasing, as the number of available events is reduced. The relative fraction
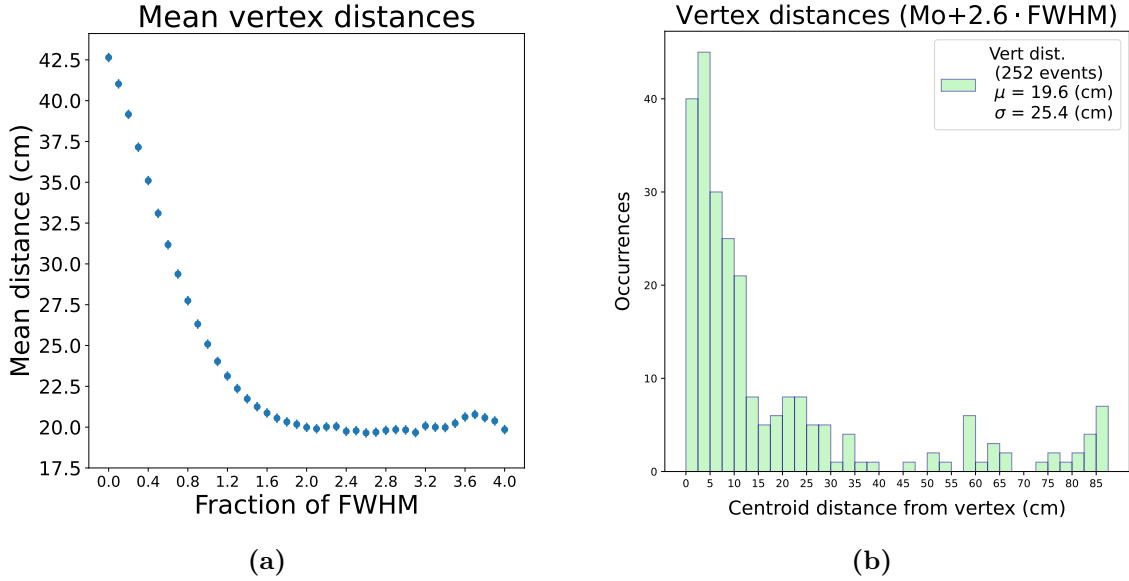
Fig. 5.8: (a) Mean of the vertex distances for the range of cuts that has been considered. The slight rise in the mean values at higher cuts is due to the reduction of events with distances $\lesssim 30$ cm, as not all survive the selection cut. The uncertainty associated to the mean distance has been estimated as $1/\sqrt{12} \simeq 0.3$ cm. (b) Histogram of the centroid distances for the cut at $\mathrm{Mo}(A) + 2.6 \cdot \mathrm{FWHM}$, with the minimum mean distance. Events with deviations above 15 cm are found to contain artefacts.

of events having $d_{cen} < 15$ cm, shown in Fig. 5.9b reaches a maximum of 70% at $\mathrm{Mo}(A) + 4 \cdot \mathrm{FWHM}$.

The lower performance of the reconstruction centroid as an estimator of the true vertex compared to the E_{dep} centroid was anticipated. This is because the latter, to which the imaging algorithm is directly correlated, shows clear deviations from the position of the vertices due to the event topology and energy deposition processes. It can be nonetheless noted that the distances of the reconstructed centroids follow a behaviour consistent to the one discussed in Section 5.1.3: a minimum for the mean is reached at a cut of $\sim \mathrm{Mo}(A) + 2.6 \cdot \mathrm{FWHM}$ and the fraction of low-distance $d_{vert} < 15$ cm increases initially with the thresholds before stabilizing.

The higher values, compared to the E_{dep} distribution analysis, of the cuts featuring the minimum mean and the maximum fraction of $d_{vert} < 15$ cm events (respectively $\mathrm{Mo}(A) + 2.7 \cdot \mathrm{FWHM}$ and $4 \cdot \mathrm{FWHM}$) may be explained as due to the true vertices corresponding to the highest E_{dep} density for most of the events: higher amplitude cuts are therefore needed to eliminate a larger fraction of the voxels, leaving out only the higher intensity core of the reconstruction, which corresponds to the vertex.

In order to assess the optimal interval of amplitude cuts from the point of view of the vertex distances, the accuracy of the estimates for the reconstructed dataset was

determined as their mean deviations. The mean vertex distances, as shown in Fig. 5.10a, decrease over the entire cut range, with a minimum of 4.5 cm at the $\mathrm{Mo} + 3.7 \cdot \mathrm{FWHM}$.

Despite the percentage of $d_{vert} < 15$ cm events still showing a slight growth at the upper end of the cut interval taken in consideration, with the maximum fraction of 70% reached for $4 \cdot \mathrm{FWHM}$, the reduction of the dataset size (as shown in the efficiency plot of Fig. 5.10b) justifies an optimal range of amplitude cuts from the vertex analysis that is consistent to the one determined from the E_{dep} centroid comparison, of $\mathrm{Mo}(A) + 2 \cdot \mathrm{FWHM}$ and $2.4 \cdot \mathrm{FWHM}$.

(a)   **(b)**
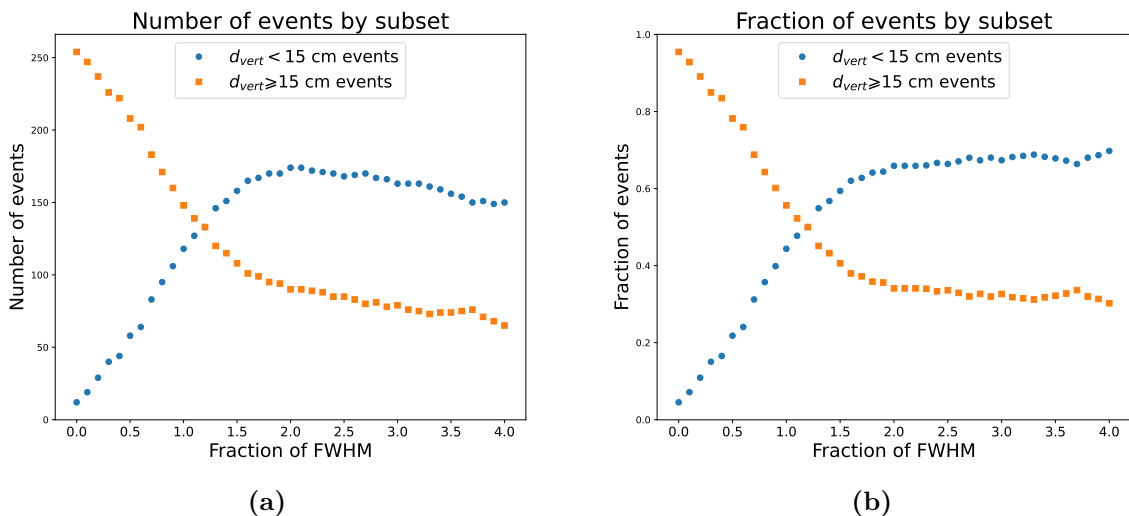
Fig. 5.9: Total number (a) and fraction (b) of events with reconstructed centroid position distance $d_{cen} < 15$ cm (blue) or $d_{cen} \geqslant 15$ cm (orange) from the true vertex position as a function of the cut.

5.1.4   Results on the centroid analysis

While the previous analyses have been able to prove the effectiveness of amplitude cuts for the purpose of improving the estimates of the E_{dep} centroid and of the true vertex, the minimum mean deviations over the complete dataset were determined to be above 15 cm and with high standard deviations in both cases. Since the mean distances correspond to significant portions of the fiducial volume[1], the reconstruction capabilities of the algorithm would be insufficient to reach the physics requirements if badly reconstructed events were to be taken into consideration. The exclusion of this subset of reconstructions has instead improved significantly the mean deviations, reaching for both the E_{dep} centroid and vertex comparisons a minimum of ~ 5 cm in the $\mathrm{Mo}(A) + 2.4 \cdot \mathrm{FWHM}$-$2.8 \cdot \mathrm{FWHM}$ optimal cut range that has been defined. Such a distance is comparable

---

[1]As a reference the fiducial semi-axis along z is of 19 cm.
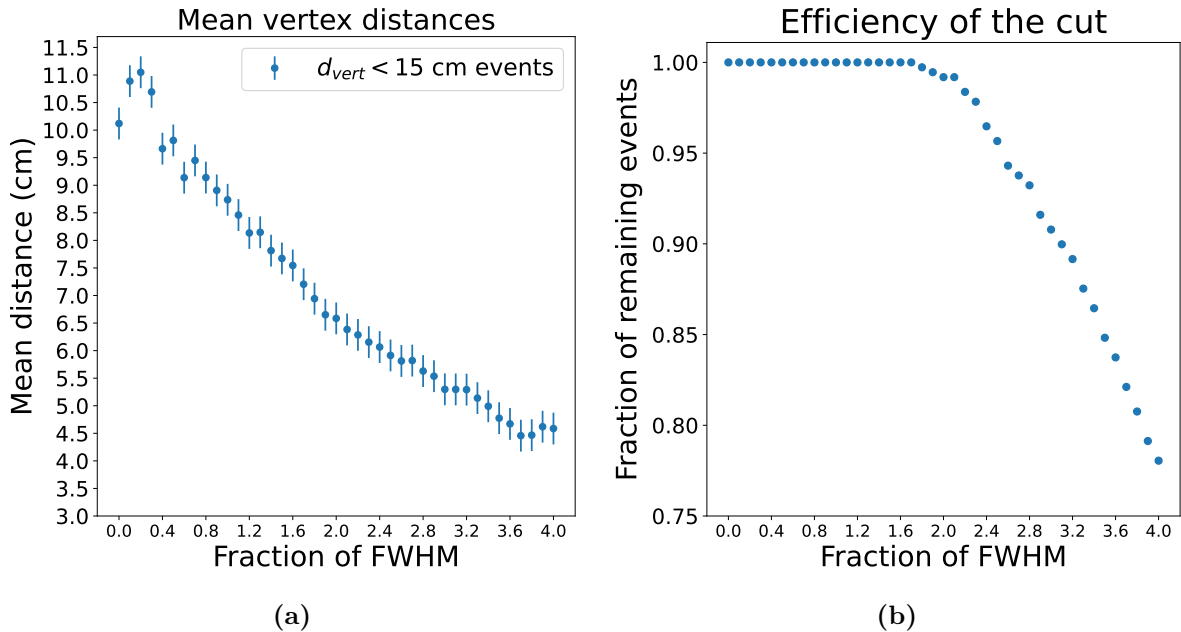
Fig. 5.10: (a) Mean vertex distances for the $d_{cen} < 15$ cm event subset. The uncertainty associated to the mean distance has been estimated as $1/\sqrt{12} \simeq 0.3$ cm. (b) Efficiency of the amplitude cuts for the vertex analysis, computed as the fraction of remaining events compared to the initial number of 266.

to the edge of the fiducial volume, allowing to place the events inside the GRAIN volume only at one standard deviation. The capabilities of the reconstruction technique are therefore assessed to be not yet fully mature, as further improvements of the algorithm are needed, aiming both at reducing the reconstruction artefacts and improving the accuracy.

5.2   Principal Component Analysis

The comparison between the reconstruction centroids and the true vertex positions performed in the previous section gave satisfactory results once badly reconstructed events were excluded. As remarked in Section 5.1.1, however, the E_{dep} centroid, to which the one of the reconstruction is related, does not correspond necessarily to the true vertex position. This is, most importantly, the case for long charged particle tracks.

In order to provide a better estimate for the vertex of tracks the alternative that was considered is the *Principal Components Analysis* (PCA) of the reconstructions. After the computation of the three principal axes of the reconstructed distribution, performed with the pre-defined function of the *Scikit-learn* Python library [66], the voxels were projected onto the major axis. The extreme projections of the distribution thus defined

the estimated endpoints of a candidate *track*. Once the background had been cut, the deviations of the endpoints from the true vertex could be expected to be lower than those of the centroid for track-like reconstructions or of the same order of the latter in the case of the symmetrical distributions that correspond to point-like emission.

As the PCA determined two endpoints, it was necessary to define a criterion with which to choose the best vertex estimator between the two. Since in the simulations the neutrino beam direction is towards the positive z coordinates, the reconstruction endpoints with the minimum z coordinate were selected for all events. The 2D histogram of the distances d_{vert} between the minimum z endpoint z_{min} and the true vertex for the amplitude cuts between $Mo(A)$ and $Mo(A) + 4 \cdot FWHM$ is shown in Fig. 5.11: the vertex distances still feature the decreasing behaviour with progressive amplitude cuts of the centroid estimate.

As a further test of the validity of the of the PCA estimate, the projection of the vertex on the segment connecting the endpoints, z_{min} and z_{max}, was computed: if the vertices were actually estimated by the minimum endpoint z_{min}, their projections on the segment, which lies on the major axis should be uniformly distributed. As shown in the 2D histogram in Fig 5.12, though, there is a significant asymmetry between the positive projections on the $(\vec{z}_{max} - \vec{z}_{min})$ segment and the negative ones. This is consistent with a vertex position inside the distribution, making the PCA endpoint estimate irrelevant compared to the centroid measure.

5.3 Linearity of energy reconstruction

An additional evaluation of the reconstruction quality of events in GRAIN can be given by the correlation between its estimated deposited energy and the true Monte Carlo value. As, to a first degree, the number of emitted scintillation photons is proportional to the energy deposited in the LAr volume, the same should hold for the number of photons that are detected. It follows that, for the reconstruction to be valid, the quantities that are proportional to the number of detected photons should display a linear dependence on the Monte Carlo energy deposition as well.

The sum of the reconstructed probability amplitudes for all voxels has been plotted in Fig. 5.13 against the cumulative energy deposition of the Monte Carlo truth (in a range of < 300 MeV), for the complete of 369 events. The linear fit to the scatter-plot shows how the dependence of the cumulative reconstruction amplitude on the true energy deposition can be indeed modelled as linear at least for $E_{dep} \lesssim 300$ MeV. Therefore it is possible to conclude that the 3D reconstruction technique maintains the information on the number of detected photons and the linear proportionality of their number to the true cumulative energy deposition in the volume.
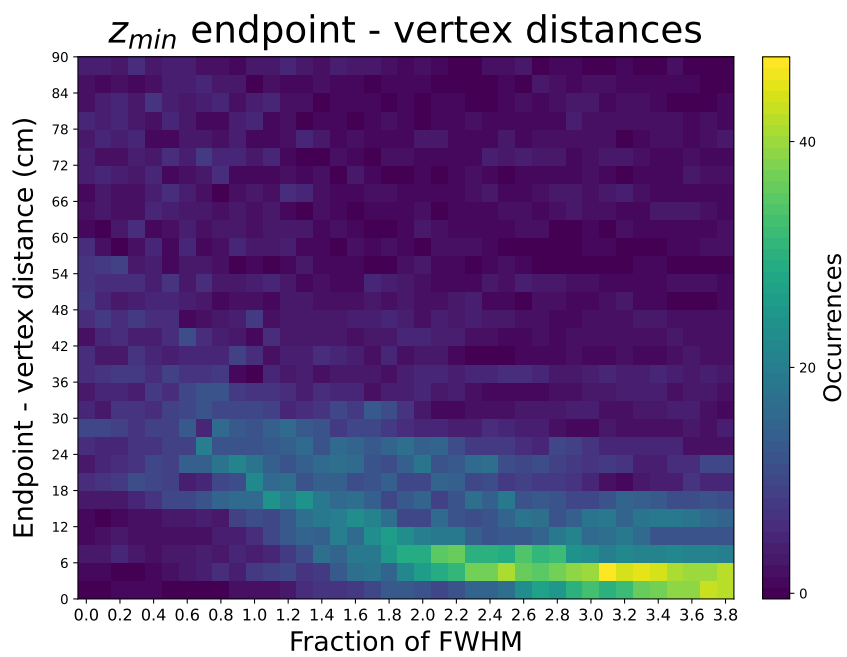
Fig. 5.11: Distribution of the distances between the z_{min} PCA endpoint and Monte Carlo vertices for cut values between $Mo(A)$ and $Mo(A) + 3.8 \cdot FWHM$. The larger dispersion of the deviation compared to the centroid estimates can be noticed.
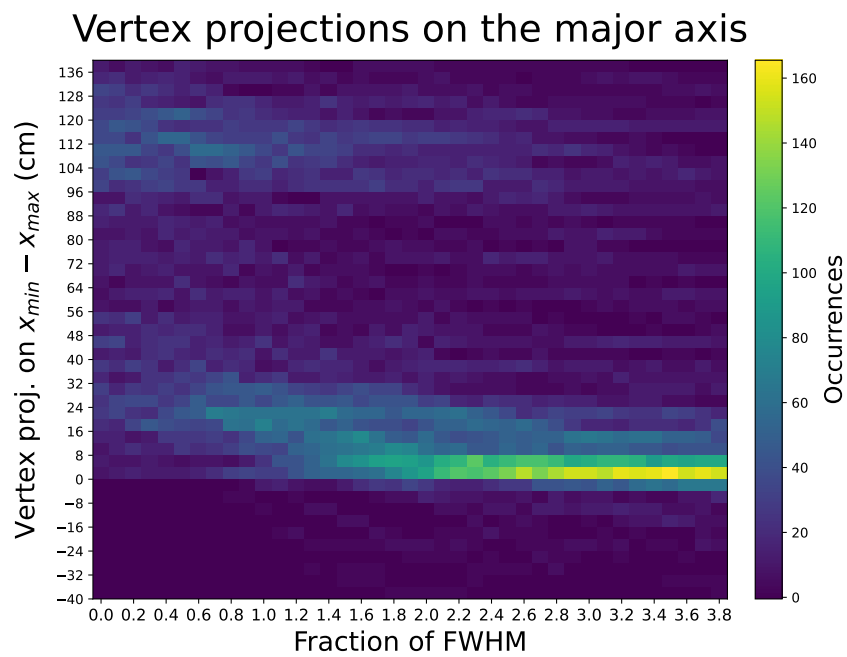
Fig. 5.12: Distribution of the projection of the vertex on the $(\vec{z}_{max} - \vec{z}_{min})$ segment along the major axis. The distribution is asymmetrical, and indicates that the vertex is inside the distribution rather than close to the endpoints.
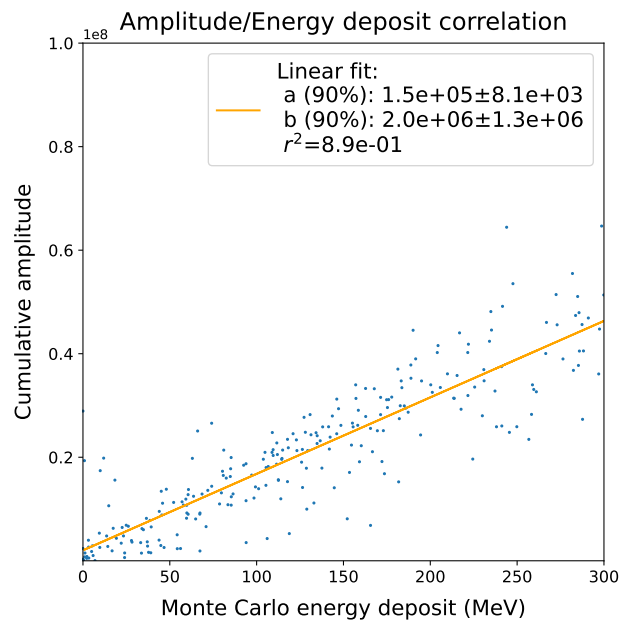
Fig. 5.13: Linear correlation plot between the cumulative reconstruction amplitudes and the true energy deposition.

Conclusions and outlook

As part of the SAND detector of the DUNE ND complex, GRAIN will serve an important role in the characterization of the neutrino beam and in the improvement LAr interaction models. For GRAIN to leverage its granularity and fast response and contribute to the SAND physics case, a well-performing optical reconstruction technique is needed.

In this thesis a first quantitative assessment of neutrino event 3D reconstruction performance for the Coded Aperture mask system in GRAIN was performed. The properties of the output of the reconstruction algorithm were first studied, determining that they contain a significant combinatorial background and artefacts, which were finally reduced by an accurate tuning of thresholds applied to the events. The similarity between the reconstructed and the true Monte Carlo energy distribution was subsequently quantified through the Structural Similarity Index. Threshold cuts were also optimized to improve the similarity.

The basic features of the events were then extracted and compared to the Monte Carlo truth. The validity of the reconstructed energy deposit centroid as an estimator of the neutrino vertex position was tested and found to be satisfactory. An optimal interval of thresholds was established, taking into consideration both accuracy and efficiency: the deviation from the expected Monte Carlo centroid for correctly reconstructed events is of ~ 4.5 cm, with an overall efficiency $\gtrsim 95\%$. Such a deviation is small compared to the resolution of typical LAr scintillation light detection systems. This makes the technique a very promising solution for the event reconstruction in GRAIN.

The endpoints of the reconstruction distributions were determined through a Principal Component Analysis and tested as estimators of the true vertex position, finding a worse performance compared to the centroid estimator. Finally, the correlation between the cumulative reconstructed probability amplitude and the true total energy deposition was determined to be linear up to 300 MeV, consistently with the expectations.

This work has provided a first quantitative assessment of the quality of the neutrino event reconstruction by optical imaging and a benchmark with which to evaluate the performances of future versions of the algorithm, thereby helping to guide its development. In particular, the analysis of the reconstruction and Monte Carlo centroids, together with the comparison of the PCA endpoints, have shown that the estimates of the vertex positions depend significantly on the true topology of the events. For this reason, the next

step will be the development of a robust criterion for the event topology discrimination and an accurate track reconstruction technique. An approach based on *Local Principal Curves* is being currently pursued, starting from one applied to the analysis of LArTPC data. The aim is to adapt the algorithm to the specific case of the 3D reconstruction in GRAIN.

References

[1] Carlo Giunti and Chung W. Kim. *Fundamentals of Neutrino Physics and Astrophysics*. 2007. ISBN: 978-0-19-850871-7.

[2] Samoil Bilenky. *Introduction to the physics of massive and mixed neutrinos*. Vol. 817. 2010. DOI: 10.1007/978-3-642-14043-3.

[3] P. A. Zyla et al. "Review of Particle Physics". In: *PTEP* 2020.8 (2020), p. 083C01. DOI: 10.1093/ptep/ptaa104.

[4] Mark Thomson. *Modern particle physics*. New York: Cambridge University Press, 2013. ISBN: 978-1-107-03426-6.

[5] C. Hagedorn et al. "CP Violation in the Lepton Sector and Implications for Leptogenesis". In: *Int. J. Mod. Phys. A* 33.05n06 (2018), p. 1842006. DOI: 10.1142/S0217751X1842006X. arXiv: 1711.02866 [hep-ph].

[6] B. T. Cleveland et al. "Measurement of the solar electron neutrino flux with the Homestake chlorine detector". In: *Astrophys. J.* 496 (1998), pp. 505–526. DOI: 10.1086/305343.

[7] M. Altmann et al. "Complete results for five years of GNO solar neutrino observations". In: *Phys. Lett. B* 616 (2005), pp. 174–190. DOI: 10.1016/j.physletb.2005.04.068. arXiv: hep-ex/0504037.

[8] J. N. Abdurashitov et al. "Solar neutrino flux measurements by the Soviet-American Gallium Experiment (SAGE) for half the 22 year solar cycle". In: *J. Exp. Theor. Phys.* 95 (2002), pp. 181–193. DOI: 10.1134/1.1506424. arXiv: astro-ph/0204245.

[9] Y. Fukuda et al. "Solar neutrino data covering solar cycle 22". In: *Phys. Rev. Lett.* 77 (1996), pp. 1683–1686. DOI: 10.1103/PhysRevLett.77.1683.

[10] J. Hosaka et al. "Solar neutrino measurements in super-Kamiokande-I". In: *Phys. Rev. D* 73 (2006), p. 112001. DOI: 10.1103/PhysRevD.73.112001. arXiv: hep-ex/0508053.

[11] B. Aharmim et al. "Electron energy spectra, fluxes, and day-night asymmetries of B-8 solar neutrinos from measurements with NaCl dissolved in the heavy-water detector at the Sudbury Neutrino Observatory". In: *Phys. Rev. C* 72 (2005), p. 055502. DOI: 10.1103/PhysRevC.72.055502. arXiv: `nucl-ex/0502021`.

[12] B. Aharmim et al. "Measurement of the ν_e and Total ^{8}B Solar Neutrino Fluxes with the Sudbury Neutrino Observatory Phase-III Data Set". In: *Phys. Rev. C* 87.1 (2013), p. 015502. DOI: 10.1103/PhysRevC.87.015502. arXiv: 1107.2901 `[nucl-ex]`.

[13] S. Gariazzo et al. "Neutrino masses and their ordering: Global Data, Priors and Models". In: *JCAP* 03 (2018), p. 011. DOI: 10.1088/1475-7516/2018/03/011. arXiv: 1801.04946 `[hep-ph]`.

[14] Michele Maltoni and Alexei Yu. Smirnov. "Solar neutrinos and neutrino physics". In: *Eur. Phys. J. A* 52.4 (2016), p. 87. DOI: 10.1140/epja/i2016-16087-0. arXiv: 1507.05287 `[hep-ph]`.

[15] Y. Fukuda et al. "Evidence for oscillation of atmospheric neutrinos". In: *Phys. Rev. Lett.* 81 (1998), pp. 1562–1567. DOI: 10.1103/PhysRevLett.81.1562. arXiv: `hep-ex/9807003`.

[16] Mayly C. Sanchez et al. "Measurement of the L/E distributions of atmospheric neutrinos in Soudan 2 and their interpretation as neutrino oscillations". In: *Phys. Rev. D* 68 (2003), p. 113004. DOI: 10.1103/PhysRevD.68.113004. arXiv: `hep-ex/0307069`.

[17] M Ambrosio et al. "Atmospheric neutrino oscillations from upward through going muon multiple scattering in MACRO". In: *Phys. Lett. B* 566 (2003), pp. 35–44. DOI: 10.1016/S0370-2693(03)00806-2. arXiv: `hep-ex/0304037`.

[18] E. Aliu et al. "Evidence for muon neutrino oscillation in an accelerator-based experiment". In: *Phys. Rev. Lett.* 94 (2005), p. 081802. DOI: 10.1103/PhysRevLett.94.081802. arXiv: `hep-ex/0411038`.

[19] Y. Ashie et al. "A Measurement of atmospheric neutrino oscillation parameters by SUPER-KAMIOKANDE I". In: *Phys. Rev. D* 71 (2005), p. 112005. DOI: 10.1103/PhysRevD.71.112005. arXiv: `hep-ex/0501064`.

[20] F. P. An et al. "Improved Measurement of Electron Antineutrino Disappearance at Daya Bay". In: *Chin. Phys. C* 37 (2013), p. 011001. DOI: 10.1088/1674-1137/37/1/011001. arXiv: 1210.6327 `[hep-ex]`.

[21] J. K. Ahn et al. "Observation of Reactor Electron Antineutrino Disappearance in the RENO Experiment". In: *Phys. Rev. Lett.* 108 (2012), p. 191802. DOI: 10.1103/PhysRevLett.108.191802. arXiv: 1204.0626 `[hep-ex]`.

[22] Y. Abe et al. "Indication of Reactor $\bar{\nu}_e$ Disappearance in the Double Chooz Experiment". In: *Phys. Rev. Lett.* 108 (2012), p. 131801. DOI: `10.1103/PhysRevLett.108.131801`. arXiv: `1112.6353 [hep-ex]`.

[23] Ivan Esteban et al. "Global analysis of three-flavour neutrino oscillations: synergies and tensions in the determination of θ_{23}, δ_{CP}, and the mass ordering". In: *JHEP* 01 (2019), p. 106. DOI: `10.1007/JHEP01(2019)106`. arXiv: `1811.05487 [hep-ph]`.

[24] Lino Miramonti. "Neutrino Physics and Astrophysics with the JUNO Detector". In: *Universe* 4.11 (2018), p. 126. DOI: `10.3390/universe4110126`.

[25] K. Hiraide et al. "Resolving θ_{23} degeneracy by accelerator and reactor neutrino oscillation experiments". In: *Phys. Rev. D* 73 (2006), p. 093008. DOI: `10.1103/PhysRevD.73.093008`. arXiv: `hep-ph/0601258`.

[26] *T2K Neutrino Oscillation Results with Data up to 2017 Summer*. KEK seminar and press release Aug 2017 (Aug. 4, 2017). 282. 2017. URL: `http://www.t2k.org/docs/talk/282`.

[27] Y. Farzan and M. Tortola. "Neutrino oscillations and Non-Standard Interactions". In: *Front. in Phys.* 6 (2018), p. 10. DOI: `10.3389/fphy.2018.00010`. arXiv: `1710.09360 [hep-ph]`.

[28] Fengpeng An et al. "Neutrino Physics with JUNO". In: *J. Phys. G* 43.3 (2016), p. 030401. DOI: `10.1088/0954-3899/43/3/030401`. arXiv: `1507.05613`.

[29] Soo-Bong Kim. "New results from RENO and prospects with RENO-50". In: *Nucl. Part. Phys. Proc.* 265-266 (2015). Ed. by Paolo Bernardini, Gianluigi Fogli, and Eligio Lisi, pp. 93–98. DOI: `10.1016/j.nuclphysbps.2015.06.024`. arXiv: `1412.2199 [hep-ex]`.

[30] D. S. Ayres et al. "NOvA: Proposal to Build a 30 Kiloton Off-Axis Detector to Study $\nu_\mu \to \nu_e$ Oscillations in the NuMI Beamline". In: (Mar. 2004). arXiv: `hep-ex/0503053`.

[31] Babak Abi et al. "Deep Underground Neutrino Experiment (DUNE), Far Detector Technical Design Report, Volume II: DUNE Physics". In: (Feb. 2020). arXiv: `2002.03005 [hep-ex]`.

[32] Shakeel Ahmed et al. "Physics Potential of the ICAL detector at the India-based Neutrino Observatory (INO)". In: *Pramana* 88.5 (2017), p. 79. DOI: `10.1007/s12043-017-1373-4`. arXiv: `1505.07380 [physics.ins-det]`.

[33] M. G. Aartsen et al. "Letter of Intent: The Precision IceCube Next Generation Upgrade (PINGU)". In: (Jan. 2014). arXiv: `1401.2046 [physics.ins-det]`.

[34] Veronique Van Elewyck. "ORCA: measuring the neutrino mass hierarchy with atmospheric neutrinos in the Mediterranean". In: *Journal of Physics: Conference Series* 598 (Apr. 2015), p. 012033. DOI: `10.1088/1742-6596/598/1/012033`.

[35] Masashi Yokoyama. "The Hyper-Kamiokande Experiment". In: *Prospects in Neutrino Physics*. Apr. 2017. arXiv: 1705.00306 [hep-ex].

[36] Marcos Dracos. "Short and Medium Baseline Reactor Neutrino Experiments". In: *28th International Symposium on Lepton Photon Interactions at High Energies*. Guangzhou, China, Aug. 2017, pp. 84–98. DOI: 10.1142/9789811207402_0006. URL: https://hal.archives-ouvertes.fr/hal-02536155.

[37] X. Qian and P. Vogel. "Neutrino Mass Hierarchy". In: *Prog. Part. Nucl. Phys.* 83 (2015), pp. 1–30. DOI: 10.1016/j.ppnp.2015.05.002. arXiv: 1505.01891 [hep-ex].

[38] Ikaros I. Bigi and A. I. Sanda. *CP violation*. Vol. 9. Cambridge University Press, Sept. 2009. ISBN: 978-0-511-57728-4, 978-0-521-84794-0, 978-1-107-42430-2. DOI: 10.1017/CBO9780511581014.

[39] Tomasz Wachala. "Recent Results on the CP Violation Search in the Accelerator Neutrino Oscillations". In: *Acta Phys. Polon. B* 48 (2017), p. 1969. DOI: 10.5506/APhysPolB.48.1969.

[40] William Marciano and Zohreh Parsa. "Intense neutrino beams and leptonic CP violation". In: *Nucl. Phys. B Proc. Suppl.* 221 (2011). Ed. by Geoffrey Mills et al., pp. 166–172. DOI: 10.1016/j.nuclphysbps.2011.03.114. arXiv: hep-ph/0610258.

[41] *Updated results from the T2K experiment with $3.13 \times 10^2 1$ protons on target* (Jan. 10, 2019). 335. 2019. URL: https://t2k.org/docs/talk/335.

[42] M. Aker et al. "Improved Upper Limit on the Neutrino Mass from a Direct Kinematic Method by KATRIN". In: *Phys. Rev. Lett.* 123.22 (2019), p. 221802. DOI: 10.1103/PhysRevLett.123.221802. arXiv: 1909.06048 [hep-ex].

[43] L. Gastaldo et al. "The Electron Capture ^{163}Ho Experiment ECHo: an overview". In: *J. Low Temp. Phys.* 176.5-6 (2014). Ed. by Erik Skirokoff, pp. 876–884. DOI: 10.1007/s10909-014-1187-4. arXiv: 1309.5214 [physics.ins-det].

[44] B. Alpert et al. "HOLMES - The Electron Capture Decay of ^{163}Ho to Measure the Electron Neutrino Mass with sub-eV sensitivity". In: *Eur. Phys. J. C* 75.3 (2015), p. 112. DOI: 10.1140/epjc/s10052-015-3329-5. arXiv: 1412.5060 [physics.ins-det].

[45] M. P. Croce et al. "Development of holmium-163 electron-capture spectroscopy with transition-edge sensors". In: *J. Low Temp. Phys.* 184.3-4 (2016). Ed. by Philippe Camus, Alexandre Juillard, and Alessandro Monfardini, pp. 958–968. DOI: 10.1007/s10909-015-1451-2. arXiv: 1510.03874 [physics.ins-det].

[46] A. Gando et al. "Search for Majorana Neutrinos near the Inverted Mass Hierarchy Region with KamLAND-Zen". In: *Phys. Rev. Lett.* 117.8 (2016). [Addendum: Phys.Rev.Lett. 117, 109903 (2016)], p. 082503. DOI: `10.1103/PhysRevLett.117.082503`. arXiv: `1605.02889 [hep-ex]`.

[47] James Strait et al. "Long-Baseline Neutrino Facility (LBNF) and Deep Underground Neutrino Experiment (DUNE): Conceptual Design Report, Volume 3: Long-Baseline Neutrino Facility for DUNE June 24, 2015". In: (Jan. 2016). arXiv: `1601.05823 [physics.ins-det]`.

[48] Babak Abi et al. "Deep Underground Neutrino Experiment (DUNE), Far Detector Technical Design Report, Volume IV: Far Detector Single-phase Technology". In: *JINST* 15.08 (2020), T08010. DOI: `10.1088/1748-0221/15/08/T08010`. arXiv: `2002.03010 [physics.ins-det]`.

[49] Sabrina Sacerdoti. "A LArTPC with Vertical Drift for the DUNE Far Detector". In: *PoS* NuFact2021 (2022), p. 173. DOI: `10.22323/1.402.0173`.

[50] Adam Abed Abud et al. "Deep Underground Neutrino Experiment (DUNE) Near Detector Conceptual Design Report". In: *Instruments* 5.4 (2021), p. 31. DOI: `10.3390/instruments5040031`. arXiv: `2103.13910 [physics.ins-det]`.

[51] *ArgonCube Website*. URL: `https://argoncube.org/index.html`.

[52] Gianfranco Ingratta. "Development of a novel LAr detector for the SAND apparatus in DUNE". MA thesis. Università di Bologna, 2021.

[53] Tadayoshi Doke, Kimiaki Masuda, and Eido Shibamura. "Estimation of absolute photon yields in liquid argon and xenon for relativistic (1 MeV) electrons". In: *Nucl. Instrum. Meth. A* 291 (1990), pp. 617–620. DOI: `10.1016/0168-9002(90)90011-T`.

[54] M. Babicz et al. "A measurement of the group velocity of scintillation light in liquid argon". In: *JINST* 15.09 (2020), P09009. DOI: `10.1088/1748-0221/15/09/P09009`. arXiv: `2002.09346 [physics.ins-det]`.

[55] Valerio Pia. "Study of a novel VUV-imaging system in liquid argon for neutrino oscillation experiments". MA thesis. Università di Bologna, 2019.

[56] M. Andreotti et al. "Coded masks for imaging of neutrino events". In: *Eur. Phys. J. C* 81.11 (2021), p. 1011. DOI: `10.1140/epjc/s10052-021-09798-y`. arXiv: `2105.10820 [physics.ins-det]`.

[57] Stephen Gottesman and E Fenimore. "New family of binary arrays for coded aperture imaging". In: *Applied optics* 28 (Oct. 1989), pp. 4344–52. DOI: `10.1364/AO.28.004344`.

[58] Michał J. Cieślak, Kelum A.A. Gamage, and Robert Glover. "Coded-aperture imaging systems: Past, present and future development – A review". In: *Radiation Measurements* 92 (2016), pp. 59–71. ISSN: 1350-4487. DOI: `https://doi.org/10.1016/j.radmeas.2016.08.002`. URL: `https://www.sciencedirect.com/science/article/pii/S1350448716301524`.

[59] E. E. Fenimore and T. M. Cannon. "Coded aperture imaging with uniformly redundant arrays". In: *Appl. Opt.* 17.3 (Feb. 1978), pp. 337–347. DOI: `10.1364/AO.17.000337`. URL: `http://opg.optica.org/ao/abstract.cfm?URI=ao-17-3-337`.

[60] R. Accorsi. "Design of a near-field coded aperture cameras for high-resolution medical and industrial gamma-ray imaging". In: (Aug. 2005).

[61] C. Andreopoulos et al. "The GENIE Neutrino Monte Carlo Generator". In: *Nucl. Instrum. Meth.* A614 (2010), pp. 87–104. DOI: `10.1016/j.nima.2009.12.009`. arXiv: `0905.2517 [hep-ph]`.

[62] Clark McGrew. *edep-sim : An Energy Deposition Simulation.* URL: `https://github.com/ClarkMcGrew/edep-sim`.

[63] S. Agostinelli et al. "Geant4—a simulation toolkit". In: *Nuclear Instruments and Methods in Physics Research Section A: Accelerators, Spectrometers, Detectors and Associated Equipment* 506.3 (2003), pp. 250–303. ISSN: 0168-9002. DOI: `https://doi.org/10.1016/S0168-9002(03)01368-8`. URL: `https://www.sciencedirect.com/science/article/pii/S0168900203013688`.

[64] Zhou Wang et al. "Image quality assessment: from error visibility to structural similarity". In: *IEEE Transactions on Image Processing* 13.4 (2004), pp. 600–612. DOI: `10.1109/TIP.2003.819861`.

[65] Stéfan van der Walt et al. "scikit-image: image processing in Python". In: *PeerJ* 2 (June 2014), e453. ISSN: 2167-8359. DOI: `10.7717/peerj.453`. URL: `https://doi.org/10.7717/peerj.453`.

[66] F. Pedregosa et al. "Scikit-learn: Machine Learning in Python". In: *Journal of Machine Learning Research* 12 (2011), pp. 2825–2830.